Modeling and Thrust Optimization of a Bio-Inspired Pulsatile Jet Thruster

by

Michael W. Krieg

B.S., University of Colorado Boulder, 2006

A thesis submitted to the

Faculty of the Graduate School of the

University of Colorado in partial fulfillment

of the requirements for the degree of

Doctor of Philosophy

Department of Aerospace Engineering Sciences

2012

This thesis entitled:
Modeling and Thrust Optimization of a Bio-Inspired Pulsatile Jet Thruster
written by Michael W. Krieg
has been approved for the Department of Aerospace Engineering Sciences

Committee Chair Kamran Mohseni

Prof. Sedat Biringen

Prof. Jean Hertzberg

Prof. Dale Lawrence

Prof. Hanspeter Schaub

Date

The final copy of this thesis has been examined by the signatories, and we find that both the content and the form meet acceptable presentation standards of scholarly work in the above mentioned discipline.

Krieg, Michael W. (Ph.D., Aerospace Engineering Sciences)

Modeling and Thrust Optimization of a Bio-Inspired Pulsatile Jet Thruster

Thesis directed by Prof. Committee Chair Kamran Mohseni

A new type of thruster technology offers promising low speed maneuvering capabilities for underwater vehicles. Similar to the natural locomotion of squid and jellyfish the thruster successively forces fluid jets in and out of a small internal cavity. We investigate several properties of squid and jellyfish locomotion to drive the thruster design including actuation of nozzle geometry and vortex ring thrust augmentation. The thrusters are compact with no extruding components to negatively impact the vehicle's drag. These devices have thrust rise-times orders of magnitude faster than those reported for typical propeller thrusters, making them an attractive option for high accuracy underwater vehicle maneuvering.

The dynamics of starting jet circulation, impulse, and kinetic energy are derived in terms of kinematics at the entrance boundary of a semi-infinite domain, specifically identifying the effect of a non-parallel incoming flow. A model for pressure at the nozzle is derived without the typical reliance on a predetermined potential function, making it a powerful tool for modeling any jet flow. Jets are created from multiple nozzle configurations to validate these models, and velocity and vorticity fields are determined using DPIV techniques. A converging starting jet resulted in circulation $90-100\%$, impulse $70-75\%$, and energy $105-135\%$ larger than a parallel starting jet with identical volume flux and piston velocity, depending on the stroke ratio. The new model is a much better predictor of the jet properties than the standard 1D slug model.

A simplified thrust model, was derived to describe the high frequency thruster characteristics. This model accurately predicts the average thrust, measured directly, for stroke ratios up to a critical value where the leading vortex ring separates from the remainder of the shear flow. A new model predicting the vortex ring pinch-off process is developed based on characteristic centerline velocities. The vortex ring pinch-off is coincides with this velocity criterion, for all cases tested.

Piston velocity program and nozzle radius are optimized with respect to average thrust, and a quantity similar to propulsive efficiency. The average thrust is maximized by a critical nozzle radius. An approximate linear time-invariant (LTI) model of the thruster vehicle system was derived which categorizes maneuvers into different characteristic regimes. Initial thruster testing showed that open and closed loop frequency response were sufficiently approximated by the LTI model, and that the thruster is ideally suited for small scale high accuracy maneuvers.

Dedication

I'd like to dedicate this work to the infinite patience of those around me.

Acknowledgements

Thanks to Torin and Tyler for fabrication, my advisor for all his wisdom, and the ONR for financial support of this research project.

Contents

Chapter

Tables

Table

Figures

Figure

Chapter 1

Introduction

1.1 Motivation

Traditionally unmanned underwater vehicles fall into one of two categories. One class of vehicles (torpedo like) are built to travel long distances with minimal energy, and are usually characterized by a long slender body, a rear propeller for propulsion and a set of fins to provide maneuvering forces. This type of vehicle is poorly suited for missions requiring a high degree of positioning accuracy because the control surfaces provide little to no maneuvering force at low forward velocity. The other class of vehicle (ROV like) is designed to operate in these situations which require high positioning accuracy, and incorporate several thrusters at various locations to provide maneuvering forces in all directions. However, this class of vehicle typically has a very high drag coefficient due to the abundance of external thrusters, and cannot travel to remote locations without additional support.

The abundance of remote marine research sites requiring high positioning accuracy for inspection, as well as the desire to create fully autonomous vehicle sensor networks, has inspired significant research in a hybrid class of vehicles with the efficient cruising characteristics of the torpedo class and the high positioning accuracy abilities of the ROV class. Some take a mechanical approach moving the maneuvering propellers into tunnels which run through the hull of the vehicle [52, 89] or into the fins themselves [19]. Others observe that nature's swimmers have a healthy balance of long distance endurance and high accuracy low speed maneuvering. Vehicles have been designed to use fins both as control surfaces at high speeds as well as mimic the low speed flapping

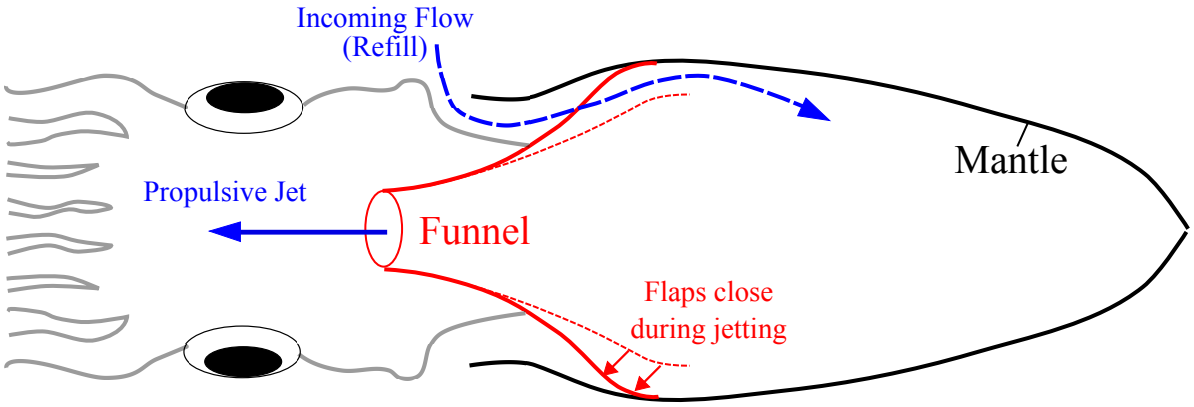

Figure 1.1: Diagram showing body layout of a squid focusing on the anatomy responsible for jetting.

of turtles and marine mammals [44, 43]; and some use tail fins as a primary means of propulsion [5]. Our inspiration comes from the cyclical jet propulsion seen in jellyfish, scallops, octopus, squid and other cephalopods.

1.2 Squid and Jellyfish Locomotion

Squid jet propulsion produces the fastest swimming velocities seen in aquatic invertebrates [4, 61]. While jetting is generally considered a less efficient form of locomotion than undulatory swimming [61, 93], squid morphology has evolved to fully exploit it. In fact propulsive efficiency was seen to rise as high as 78% in adult *L. brevis* swimming at high velocities, and averaged 87% ($\pm$6.5%) for paralarvae [7], challenging the notion that a low volume high velocity jet inherently negates a high propulsive efficiency. Soaring and climbing vertically through ocean currents, negotiating prey capture, or hovering near the surface are a few of the squid's many swimming capabilities [61].

In general, jetting locomotion begins when the squid inhales seawater through a pair of vents or aperture behind the head, filling the mantle cavity. The mantle then contracts forcing seawater out through the funnel which rolls into a high momentum vortex ring and imparts the necessary propulsive force [4]. Figure 1.1 shows the basic squid layout and anatomy used for jetting. The versatility of the system permits both low speed steady swimming or cruising, and fast impulsive escape jetting. Two distinct gaits are seen in steadily swimming squid as determined by the

nature of the expelled jet [6], those being above or below the jet formation number (The formation number is defined in great detail in section 5.1.2; it is essentially a measure of the quality of the jet). During cruising, squid swim at nominal speed with a higher efficiency; whereas, escape jetting involves a hyperinflation of the mantle followed by a fast powerful contraction to impart significant acceleration at the cost of fluid dynamic losses; similar to the loss in efficiency seen in high velocity jet locomotion of jellyfish [83]. Bartol et al. [6] report cruising mode efficiency at 69% (±14%) averaged over several species and swimming speeds, and 59% (±14%) for escape jetting.

The locomotion of jellyfish tends to be very similar to that of squid with some key differences; primarily that the refilling phase of jellyfish swimming uses the same bell opening as the jetting phase. However, despite the fact that squid do not use the funnel during refilling, the inlet vents are still on the anterior side of the mantle cavity (See Figure 1.1), meaning that locomotion for both organisms is quite different from traditional pumping mechanisms. Similar to the different gaits seen in squid locomotion, different species of jellyfish generally fall into two categories of swimmers based on the quality of vortex ring they produce. Jellyfish like moon jellyfish have a very large bell opening, and the jetting motion is more similar to a paddling type motion. Box jellyfish and other faster swimming jellyfish have smaller bell openings with nozzle-like flaps at the velar cavity opening, and have a much more distinct jetting motion.

Jellyfish morphology during swimming has been digitally captured from experiment, and the body motions imported into numerical simulations to predict body forces on the swimming jellyfish, determining drastically different swimming efficiencies. Froude propulsive efficiency of jellyfish was calculated through this process by Sahin and Mohseni [81, 82, 83] to be 37% for *Aeqorea victoria* and 17% for *Sarsia tubulosa*. It should be noted that both species of jellyfish most likely do not use vortex generation for the sole purpose of locomotion. *Aeqorea victoria* uses vortex generation for feeding as demonstrated through Lagrangian coherent structures (LCS) analysis [47, 46, 97], and *Sarsia tubulosa* use jetting as an escape mechanism, where survival supersedes the desire for efficient propulsion. Empirical data gathered by Dabiri et al. through DPIV measurements of several species shows similar efficiency characteristics for the different swimming patterns [15].

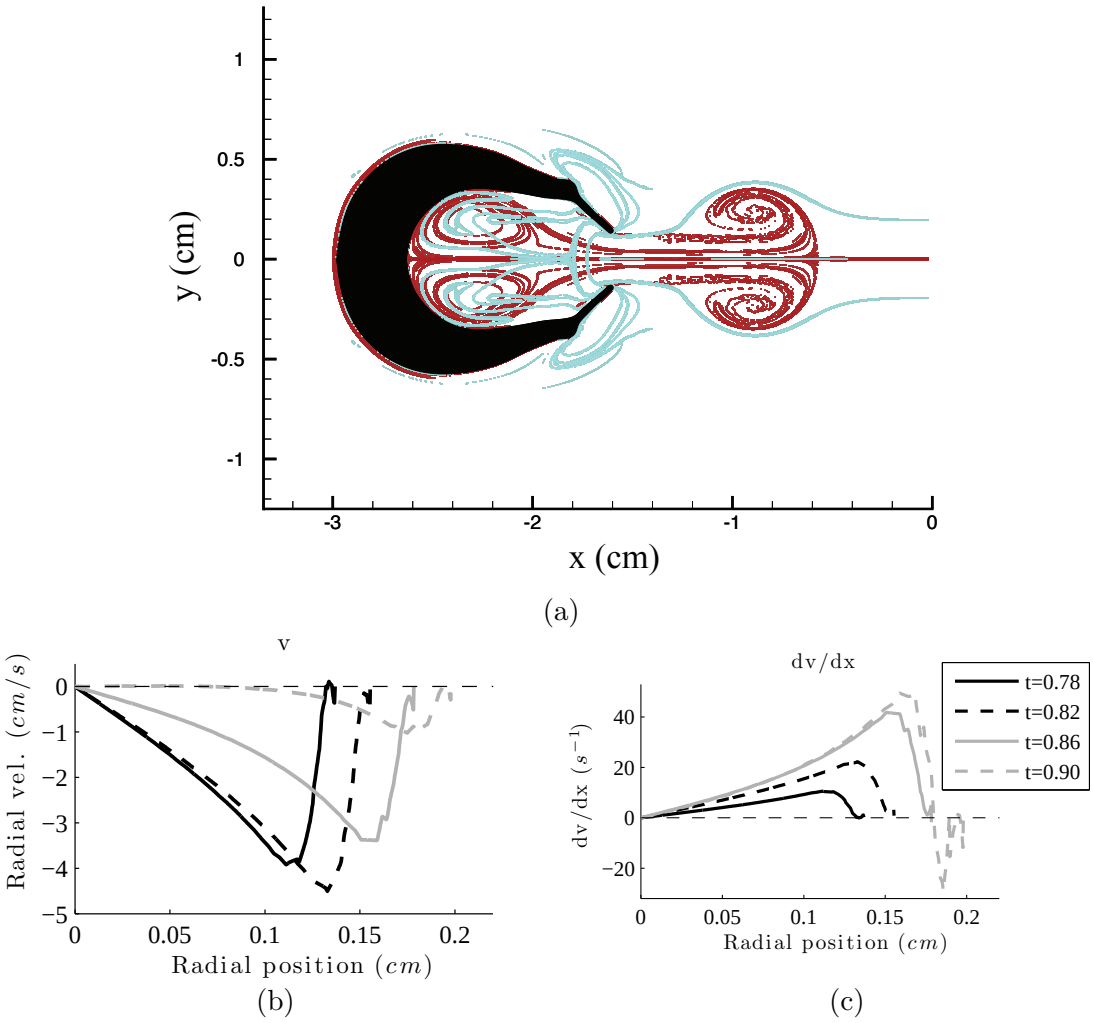

Figure 1.2: A swimming jellyfish, *Sarsia tubulosa*, is shown along with stable (blue) and unstable (red) Lagrangian Coherent Structures (LCS) around the body for a given instant during the jetting phase (a). Local radial velocity velocity at the velar opening is plotted for several instances in (b), as well as the gradient of the radial velocity, $\partial v/\partial x$ (c). Data reproduced from [83, 47]

Figure 1.2(a) shows stable and unstable LCS around a swimming jellyfish taken from simulations in [83] and [47]. During the phase of jetting which is shown in this figure, the velar opening is a converging conical nozzle. Which creates a converging radial velocity in the jet being expelled which is shown in Figure 1.2(b). The squid funnel changes shape during pulsation and at times resembles a converging conical nozzle, and a converging radial velocity can be seen very close to the exit of the funnel in figure 8 of [4].

Non-parallel starting jets serve an important function in the jetting of marine animals like jellyfish and squid, but it is not clear exactly which swimming behaviors benefit propulsion vs. feeding and respiration.

1.3 Problem Statement

Several aspects of squid and jellyfish locomotion are quite different from continuous propulsive jetting mechanisms used in recreational watercraft. These animals are limited to a given finite jet volume, and a wide variety of species have similar propulsive jet characteristics. These characteristics include some amount of converging radial velocity at the jet source, as well as similar vortex ring patterns.

This investigation analyzes these behaviors to determine the exact effect on propulsion. More specifically, a control volume analysis is derived to model the evolution of circulation, impulse, and kinetic energy of non-parallel starting jets in terms of kinematics at the entrance boundary; and the kinematics are parameterized for several nozzle configurations. A new, more accurate, velocity criterion corresponding to vortex ring pinch-off is presented and validated, and the starting jet control volume analysis is incorporated to model the vortex ring formation process again in terms of the entrance boundary kinematics. Finally this analysis is used to create a methodology for optimizing propulsive jetting with respect to desirable locomotion performance indices. The prototype thruster is also analyzed with respect to inclusion in typical vehicle control environments.

1.4 Starting Jet Dynamics

The study of short duration starting jets is almost synonymous with the study of vortex ring formation dynamics. In this type of flow a jet of fluid is expelled into a semi-infinite resting reservoir of similarly dense fluid, where the unstable shear layer/tube begins to spiral, and the jet rolls into a single vortex ring or a vortex ring with a trailing wake depending on the exact jetting parameters, [23]. The formation and evolution of vortex rings have been extensively studied by the fluid dynamics community; for a more in depth review of vortex rings see [84]. However, the formation analysis has been limited to a fairly restricted set of boundary flow conditions.

In practice starting jets which enter the domain with nearly parallel axial streamlines can be created by ejecting the jet through a nozzle which consists of a long cylindrical tube. Here, as a point of clarification, we define 'nozzle' to be any solid structure which separates the emerging jet flow from the surrounding fluid reservoir. Commonly, flows ejected through a tube nozzle are driven by a moving piston internal to the cylinder. Starting flows with converging streamlines can be created by ejecting the jet through a converging conical nozzle. Converging conical nozzles are a family of nozzles extending from a nearly cylindrical tube to nozzles with increasing slope until the nozzle cone becomes a flat plate with a central circular orifice, which we will call an orifice nozzle. In these flows the fluid behind the nozzle must converge to pass through the central opening and these converging streamlines persist downstream of the nozzle exit plane. Similarly, starting flows with diverging streamlines can be created by diverging conical nozzles with the maximum divergence created by an unbounded source just outside the domain. It should be noted here that during the early stages of vortex formation the vortex ring is very close to the entrance boundary, and will induce a radial velocity on the flow crossing the entrance plane. However, throughout this paper we will refer to jet flows which are expelled through tube nozzles as parallel jets, and jet flows expelled through converging or diverging nozzles as non-parallel in reference to the nature of the source flow, despite the influence of the vortex ring at early formation times.

Experimental studies on parallel starting jets have characterized jet velocity profiles and

vortex ring geometries [18]. Gharib et al. [23] used DPIV to get the full velocity field of parallel flows and used that data to determine vortex ring circulation and vortex ring separation dynamics. Using numerical simulations this analysis was extended to flows with a much larger range of jet velocity profiles [78] and shear layer growth/acceleration [57]. The circulation of the primary vortex ring is usually modeled by a 1D slug model [25, 84, 23], or through the self similar roll-up of the vortex tube extending from the nozzle [67, 79, 69, 68, 58]. The circulation and impulse of the jet were modeled by the 1D slug model with an added contribution due to 'overpressure' by ([40, 39]). However, vortex rings formed from non-parallel starting jets have only been recently studied through numerical simulation by Rosenfeld et al. [77], even though non-parallel starting jets exist in several vortex flows from squid and jellyfish propulsion, to cardiac flows, to synthetic jet actuation. Rosenfeld et al. [77] investigated the effect the added 2D velocity component had on the circulation of the forming jet. This paper presents additional empirical data to support these findings, and extends the analysis to impulse and energy, and presents an alternative model to predict these quantities in the jet, for a general case of an incoming flow with known velocity profiles at the boundary.

Therefore, the tools of this manuscript can be used to analyze jellyfish and squid jetting, which in turn will help to clarify the genetic optimization of these animals swimming behaviors, since impulse and kinetic energy of the jet are directly related to propulsion, whereas creating a jet with increased circulation may be tied to other functions like feeding or respiration.

An accurate model for determining the kinetic energy of a fluid jet as well as the pressure along the jet entrance boundary is an invaluable tool for analyzing any fluid propulsor. Propulsive efficiency of a vehicle driving mechanism is inversely proportional to the energy required to generate motion. For propulsors in a fluid environment this is directly related to the kinetic energy of the jet created while propelling the vehicle forward. The pressure at the entrance boundary of a parallel starting jet was approximated by Krueger in [39]. This was done by equating the starting jet flow to the flow around a translating flat plate with the same propagation velocity as the leading vortex ring, and determining pressure from the resulting potential function, where the plate is oriented

normal to the axis of symmetry and moves parallel to it. The modeling of this study allows jet energy and nozzle pressure to be determined using only the velocity profiles at the jet entrance boundary. Though we focus mainly on finite jets in this paper, the analysis can be extended to continuous jets as well.

One of the biggest advantages to using pulsatile jet thrusters for underwater vehicle locomotion is that they can be installed within the hull of the vehicle with no protruding control surfaces, reducing the impact on the overall drag of the vehicle [35]. However, to create a parallel starting jet this thruster would require either an external tube nozzle, which would eliminate the beneficial drag characteristics, or an internal tube nozzle which would use up valuable payload space. Therefore it is ideal to create a thruster which expels jets through a circular orifice in the side of the vehicle, but this will generate a jet with a converging radial velocity. Therefore an accurate 2D energy model is crucial to determining the effect that this thruster arrangement has on propulsive efficiency.

The rate of circulation and momentum transfered to the external flow could play a key role in defining synthetic jet formation criteria. Characteristic jet flow parameters like Strouhal number are determined entirely from axial jet velocity; however, as is shown in this paper, the radial velocity of the jet flow at the nozzle exit plane has a significant effect on the rate of circulation, impulse, and energy added to the external flow. Ignoring the radial velocity during normalization produces an underspecified scaling law which results in large scatter in experimental data. Holman et al. [31] approximated the vorticity flux from axial jet velocity which was related to Strouhal number to give a criterion for synthetic jet formation. The entrance geometry of the synthetic jet nozzle was observed to strongly affect this criterion, and a heuristic expression was used to modify the vorticity flux based on nozzle entrance curvature. Similarly, the entrance length was characterized for zero-net mass-flux devices with a variety of channel entrance conditions in [71], showing that a sharp edge at the channel entrance has a strong effect on vorticity flux and entrance length. While not pursued here, we expect that if the characteristic vorticity flux and Strouhal number are redefined to include contributions from radial velocity, the jet formation constant and entrance length, as well as other characteristic synthetic jet parameters, would converge upon a

more universal value independent of specific device geometry. Additionally, predicting jet kinetic energy and nozzle pressure could serve as a powerful tool for analyzing and designing synthetic jet actuators, one particular application would be improving energetic cost functions for optimization of systems which use synthetic jets for active flow control in airfoil drag reduction applications.

A more complete model for the circulation, impulse, and energy of a jet formed from incoming flow with non-zero radial velocity is given based on the flux of kinematic quantities across the entrance plane, which in all cases reduces to the evaluation of surface integrals at the boundary. The pressure profile at the entrance boundary which is required to evaluate energy is also derived in terms of the entrance plane kinematics. The velocity profiles at the inflow are then parameterized for a set of nozzle configurations allowing the invariants of motion to be calculated from a limited number of parameters. It should be noted that the hydrodynamic impulse is modeled, because the rate of change of the hydrodynamic impulse is equal to the net external force required to create the flow. This is not in all cases equal to the total fluid momentum. The derivation of total jet circulation, impulse, and kinetic energy is given in Chapter 2, and the general form model for the axial and radial velocity profiles for several actual nozzle flows is given in Chapter 4 allowing the total circulation, impulse, and energy to be predicted. This model is validated in Chapter 6, showing good agreement with actual jet values.

1.5 Vortex Ring Dynamics

Squid and jellyfish locomotion has been linked to vortex ring formation dynamics in the propulsive jet [7, 6, 81, 82, 83, 15], and a phenomena known as vortex ring 'pinch-off', is closely associated with the efficiency of the propulsive jet. Vortex ring pinch-off is one of the most well studied and denotative aspects of vortex ring formation. This is a process where a forming vortex ring achieves a critical state and separates from the remainder of the shear flow feeding the vortex ring growth. This phenomena gained notoriety through the classic paper by Gharib et al. [23]. In this study vortex rings were generated experimentally using a piston-cylinder device and analyzed using DPIV techniques. A circulation history of both the vortex ring and the total expelled jet was

extracted from the DPIV vorticity field. It was observed that as the jet formation time increases, the primary vortex ring grows until it becomes saturated and can no longer accept circulation in its current arrangement, and 'pinches off' from the trailing shear flow. The formation time is defined as the time since flow initiation normalized by the piston velocity, u_p, and cylinder diameter, D, $t^\star = \int_0^t u_p \, d\tau / D$. Gharib et. al. defined the *formation number* as the formation time when the total jet circulation first reached the final circulation of the primary vortex ring; and additionally showed that jets generated with a variety of piston velocity programs, $u_p(t)$, have a nearly universal formation number (3.6 - 4.2).

The experimental studies of Gharib et al. were limited to starting flows with a fairly specific jet velocity profile, despite the wide range of piston velocity programs. Numerical simulations performed by Rosenfeld et al. [78] were not restricted by the mechanical limitations of a physical vortex generator, and examined formation dynamics of jets with a wide variety of axial velocity profiles, ranging from the top hat profile to the fully developed Poiseuille flow. It was observed that jets formed with a more parabolic velocity profile separate at a lower formation number, dropping as low as 0.9 for a fully developed pipe flow. However, all cases were limited to parallel starting jets, meaning that at the entrance boundary there is no radial velocity and the streamlines are parallel (similar to flows created with piston-cylinder vortex generators). The rate of circulation added to the system was observed to be drastically different for non-parallel jet flows [77, 37], and vortex rings created from converging jet flows have formation numbers drastically lower than parallel jets [77].

The study by Mohseni et al. [57] showed that the formation number can also be shifted by adjusting the shear layer diameter during pulsation or by accelerating the shear layer. Vortex rings generated with a background co-flow were studied by Krueger et al. [38] exhibiting a decrease in formation number which was proportional to the ratio of jet velocity to co-flow velocity. Dabiri and Gharib [17] present experimental data on the effect of changing nozzle diameter during pulsation on formation number, but do not account for the radial velocity in the nozzle arrangement.

It follows from the Kelvin-Benjamin variational principle that the energy of steadily trans-

lating vortex rings is maximized with respect to impulse preserving iso-vortical perturbations [10, 76, 75]. Gharib et al. [23] suggested that pinch-off is a direct manifestation of this principle whereby the energy required for the jet to attain steady motion increases with increasing impulse and circulation until it becomes equal to the energy of the forming jet and the vortex ring separates from the remainder of the shear flow. Mohseni and Gharib [57] analytically solved for the formation number utilizing this principle by equating the forming vortex ring to a member of the Norbury family of vortex rings [59, 60, 21, 22], and using the 1D slug approximation to model the circulation, impulse, and energy of the ejected jet.

Shusser and Gharib [85] suggest that an equality between jet velocity and vortex ring translational velocity should provide a good criterion for vortex ring pinch-off, and equated this condition to the Kelvin-Benjamin variational principle in [86]. This analysis represented the KB principle by the constraint that the required energy for steady propagation must be less than the jet energy or the vortex ring will pinch-off.

Within this manuscript the kinematic pinch-off criterion presented by Shusser and Gharib [86] is re-evaluated, and another more robust criterion is proposed. This study also provides additional experimental data to support the simulations of Rosenfeld et al. [77], and extends pinch-off analysis to non-parallel starting jets. The new kinematic velocity criterion is described in Chapter 5, and is validated in Chapter 6.

1.6 Operational Usage

Traditional propeller type thrusters are very efficient when operating at nominal rotation rates. However, accurate positioning often requires short impulses, which correspond to propeller rotations on the order of single rotations, resulting in unpredictable control forces [98]. This coupled with the unpredictability of typical marine environments causes traditional propeller type thrusters to be non-ideal for accurate maneuvering. The prototype thruster of this investigation is extremely much more accurate for small corrective impulses, since the thrust can be quantized down to the level of a single pulsation whose impulse is described in great detail in Chapters 2 and 4.

Though the thruster studied here is loosely inspired by the natural locomotion of squid and jellyfish, there are several aspects of the thruster which are well beyond the capabilities of any jetting animals. One obvious example is that the thruster of this investigation is not limited to low pulsation frequencies, which are more ideal for small scale corrective propulsion. The high frequency operation of this type of thruster will certainly come into use during normal vehicle maneuvers, and the response of the thruster under high frequency actuation is presented in Section 6.6. Traditional propeller type thrusters also have a rise time associated with reaching the desired thrust. This rise time is inversely proportional to the level of thrust and can take on the order of several seconds for the low thrust ranges [98, 20], additionally tunnel thrusters have been observed to continue producing a force even after being terminated [52]. The rise time of the prototype thruster is examined for high frequency operation showing similar rise times, but these rise times are orders of magnitude faster than those for propeller thrusters, and no lingering force is present when the flow is terminated. The high frequency testing also characterized the average thrust production, showing that average thrust suffers from losses when the jet is being expelled at high frequencies with a stroke ratio above the formation number. These losses are attributed to interactions with the jet trailing wake during thruster cavity refilling.

This observation inspired an optimization analysis, whereby the average thrust, as well as a measure of jet efficiency, are optimized with respect to the selection of piston velocity program and nozzle radius. The constraint that the stroke ratio of the expelled jet must be below the resulting formation number, is critical to finding any optimal driving program for the thruster, and actually reduces the optimization problem to the selection of the nozzle radius. This optimization analysis is given in Chapter 7.

Additionally, an approximated transfer function of the thruster output is derived which can be used in linear time-invariant control models. We also developed an approximated LTI model of underwater vehicle dynamics which separates maneuvers into different regimes based on the ratio of the the maneuver scale to the vehicle size. The approximated vehicle-thruster LTI model was used to study open and closed loop frequency response of the thruster in a mock control environment.

It is shown that the cutoff-frequency of the thruster and loop gains are well predicted by the approximated transfer function, and that the thruster is more ideally suited for small scale high frequency maneuvers. This analysis is given in Chapter 8.

1.7 Contributions

Listed here are this study's contributions to the field.

- Design and fabrication of a new type of vortex ring thruster.
- High frequency thrust characterization of vortex ring thruster.
- Model rate of change of hydrodynamic impulse in a starting jet system with non-zero radial velocity in the jet.
- Model nozzle pressure for any axisymmetric jet, purely in terms of kinematics at the nozzle plane (no reliance on approximated potential field).
- Introduce generic polynomial parameterization for any jet axial velocity profile, and derive circulation, impulse, and energy of that parameterization.
- Introduce simple linear parameterization for any jet radial velocity profile, and derive circulation, impulse, and energy of that parameterization.
- Develop more accurate velocity based criterion for vortex ring pinch off, in both parallel and non-parallel flows.
- Introduce optimization methodology, based on dynamic formation number constraint, for finite propulsive jets.
- Model approximate transfer function of thruster dynamics.
- Develop maneuver scaling technique for LTI frequency response analysis of non-linear vehicle environments.

- Implement vortex ring thrusters on vehicle testbeds to perform basic maneuvers.

- Model for the energy storage mechanics of collagen fibers in the squid mantle [36].

Chapter 2

Starting Jet Control Volume Analysis

The circulation, hydrodynamic impulse, and kinetic energy of a starting jet are modeled with a control volume analysis which relates the kinematics at the entrance boundary to the rate of change of those quantities. The fluid in the control volume is assumed to start at rest, so that integration of these rates over time gives the total circulation, impulse, and energy of the jet. This section will present the control volume analysis in terms of unspecified velocity profiles at the entrance boundary. These velocity profiles are specific to the method used to generate the flow and will be parameterized for several actuation methods in Chapter 4.

We consider a semi-infinite axisymmetric control volume, which extends from the axis of symmetry to infinity, R_∞, in the radial direction, and from the source of the starting flow, x_0, to infinity, x_∞, in the axial direction as is depicted in Figure 2.1. The position and velocity vectors in the cylindrical coordinate system are $\vec{x} = [r, \phi, x]^T$ and $\vec{u} = [v, w, u]^T$, respectively. The model presented in this section will presume that the control volume is truly infinite in the directions specified, when in actuality the fluid reservoir for experimentation is bounded by the walls of the testing tank. However, the distances to these boundaries are sufficiently large to consider the fluid reservoir unbounded, R_∞ is at least 50 times the nozzle radius, and x_∞ is at least 140 times the nozzle radius.

The flow is assumed to be incompressible with a constant density, ρ. The flow is also assumed to be symmetric about the x-axis with no swirl, so that $w = 0$ and $\partial/\partial\phi = 0$. In the axisymmetric

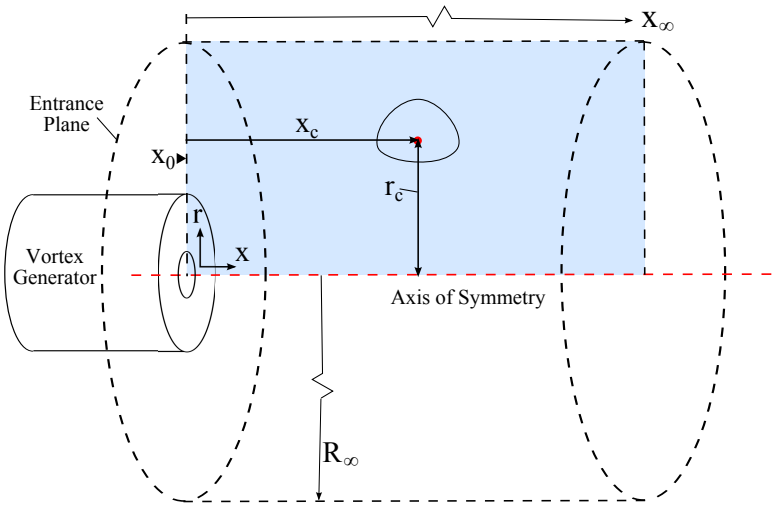

Figure 2.1: Definition of problem coordinate system and control volume boundaries, r_c and x_c are the radial and axial coordinates of the leading vortex ring center in this coordinate system.

coordinate system with the preceding assumptions the continuity equation can be written,

$$\frac{\partial u}{\partial x} + \frac{\partial v}{\partial r} + \frac{v}{r} = 0 \ . \tag{2.1}$$

The walls of the tank, and the center of mass of the fluid remain stationary meaning that there is no net force acting on the control volume, and forces are transmitted between the fluid and the tank walls through pressure forces. Therefore, there are no body forces in this specific control volume. It is also assumed that the effect of viscous dissipation is negligible and the governing dynamics of the flow field are modeled by the momentum equation,

$$\rho \frac{D\vec{u}}{Dt} = -\frac{1}{\rho} \nabla P \ . \tag{2.2}$$

Here P is the local pressure including the potentials of all conservative forces. Taking the curl of this equation, one obtains the vorticity transport equation, which is presented here in vector product form recognizing that the divergence of both vorticity and velocity are zero,

$$\frac{\partial \vec{\omega}}{\partial t} = \nabla \times (\vec{u} \times \vec{\omega}) \ . \tag{2.3}$$

For the remainder of the analysis the equations presented will not include the fluid density, ρ, meaning that the quantities are calculated per unit density; furthermore, in the system of units used for this experiment (g, cm, s) the density of water actually happens to be very close to 1. The density of water is 1 - 0.96 g cm^{-3} depending on temperature.

2.1 Circulation

The total circulation of the jet is just the integral of the vorticity over the axisymmetric plane, $[r, x]$. For inviscid fluids, circulation is an invariant, and the rate of change of circulation is equal to the flux of vorticity into the control volume. Since the vorticity is confined to the core of the primary vortex ring and trailing shear layer, the flux of vorticity across the boundaries $r = R_\infty$ and $x = x_\infty$ drops to zero, and the rate of change of the circulation is equal to the flux of vorticity across the nozzle exit plane [18],

$$\frac{d\Gamma}{dt} = \int_0^{R_\infty} u \left(\frac{du}{dr} - \frac{dv}{dx} \right) dr \ . \tag{2.4}$$

As was noted by [78, 77] the first term is independent of the specific axial velocity profile so that given the centerline velocity, u_0, the evolution of circulation becomes,

$$\frac{d\Gamma}{dt} = -\frac{1}{2}u_0^2 - \int_0^{R_\infty} u\frac{dv}{dx}\,dr\ . \tag{2.5}$$

For parallel starting jets the rate of change is mostly dependent on the axial velocity at the centerline, but the additional terms become significant for non-parallel starting jets.

2.2 Hydrodynamic Impulse and Momentum

Now we perform a similar derivation to arrive at the rate of change of impulse in terms of the same kinematic terms at the entrance boundary. The hydrodynamic impulse of the control volume is defined as,

$$\vec{I}_{\mathrm{h}} \equiv \frac{1}{2}\int_{CV} \vec{x}\times\vec{\omega}\,d\vec{x}\ . \tag{2.6}$$

It was shown by [42] (and in vector form by [80]) that in an unbounded fluid with vorticity confined to a finite region, the rate of change of the hydrodynamic impulse is equal to the total non-conservative body forces acting on the fluid. The following analysis gives the rate of change of the hydrodynamic impulse in a semi-infinite domain (more specifically the control volume of this section). The rate of change of hydrodynamic impulse in this bounded domain will be related to a surface integral at the entrance plane, but this integral is not exactly equal to the flux of the integrand of (2.6). Therefore, this rate of change of impulse is not necessarily equal to the force imposed on the source flow; however, the total hydrodynamic impulse of the jet at the end of pulsation is equal to the integral of that force, since at the end of pulsation the volume can be assumed to be unbounded.

Taking the total derivative of the hydrodynamic impulse, and using the vorticity transport equation (2.3) as the rate of change of vorticity, provides rate of change of hydrodynamic impulse

of an axisymmetric inviscid jet with no swirl,

$$\frac{d\vec{I}_{\mathrm{h}}}{dt} = \frac{1}{2}\begin{bmatrix} \iint -x\left(\dfrac{\partial(-u\omega)}{\partial x} - \dfrac{\partial(v\omega)}{\partial r}\right) 2\pi r\, dr dx \\ 0 \\ \iint r\left(\dfrac{\partial(-u\omega)}{\partial x} - \dfrac{\partial(v\omega)}{\partial r}\right) 2\pi r\, dr dx \end{bmatrix} . \tag{2.7}$$

The hydrodynamic impulse in the radial direction is of little concern (and indeed can be shown to be equal to zero), so we will focus on impulse in the axial direction. The volume integral can be simplified to a sum of surface integrals by taking a series of partial integrations and utilizing the incompressibility condition.

$$\frac{dI_{\mathrm{h}}}{dt} = \pi \int_0^{R_\infty} \left[-r^2 u\omega - rv^2 + ru^2\right]_{x_0}^{x_\infty} dr + \pi \int_{x_0}^{x_\infty} \left[-r^2 v\omega + 2rvu\right]_0^{R_\infty} dx . \tag{2.8}$$

Now the integral terms at the far field boundary can be eliminated using an order of magnitude Stream function analysis. The vorticity is confined to the core of the primary vortex ring and the trailing shear flow, so along the far surfaces the bounded vorticity appears as a point vortex at the origin, and the Stokes Stream function can be treated like that in an unbounded spherical domain since the vorticity is an equally infinite distance from the boundaries in the radial and axial directions, respectively. The first integrand term in both integrals of equation (2.8) involve the vorticity which is known to be zero at the farfield boundaries. Using the Stokes Stream function [12] and [80] showed that in an unbounded spherical domain the velocities, u and v, scale with r^{-2}. From this relation, the remaining integrand terms of (2.8) at farfield boundaries scale with r^{-3} meaning that the integrand drops to zero faster than the integration area grows at infinity. Therefore the surface integrals taken along the boundaries $x = x_\infty$ and $r = R_\infty$ can be neglected and the surface integral of (2.8) need only be calculated along the boundary $x = x_0$,

$$\frac{dI_{\mathrm{h}}}{dt} = \pi \int_0^{R_\infty} \left[ur^2\omega + rv^2 - u^2 r\right]_{x=x_0} dr . \tag{2.9}$$

Separating the vorticity term and performing a partial integration allows us to simplify,

$$\frac{dI_{\mathrm{h}}}{dt} = -\pi \int_0^{R_\infty} \left[2u^2 r + u\frac{dv}{dx}r^2 - v^2 r\right]_{x=x_0} dr . \tag{2.10}$$

The first flux term should look familiar, it is the axial momentum across the entrance boundary. Several studies ([25, 84, 23, 57]) approximate the jet circulation assuming that the jet leaves the vortex ring generator with a uniform axial velocity and no radial velocity (meaning that the jet is considered a uniform slug of fluid). Using the slug model approximation the rate of change of hydrodynamic impulse can be simplified to $dI_{\mathrm{h}} = \pi u_p^2 R^2 dt$. The integral of this term is used in [57, 40, 34] to predict the total impulse of the jet. For simplicity, throughout the remainder of the paper the hydrodynamic impulse in the axial direction will just be referred to as the impulse of the jet, I.

The total momentum of the control volume, $H = \int \vec{u}\, d\vec{x}$, is not in general equal to the hydrodynamic impulse. Classical analysis by [12] and [80], has shown that in a spherical control volume, extended to infinity, with vorticity localized to a confined central region the relationship is $H = \frac{2}{3} I_h$. To illustrate this point we integrate the momentum equation (2.2) over the entire control volume to get the rate of change of the total momentum, $\vec{H}$, and making a partial integration gives only surface integral terms,

$$\begin{aligned} \int \frac{\partial \vec{u}}{\partial t}\, d\vec{x} = \frac{d\vec{H}}{dt} &= -\int \vec{u} \cdot \nabla \vec{u}\, d\vec{x} - \int \nabla p\, d\vec{x} \\ &= -\int \vec{u}\, (\vec{u} \cdot \vec{n})\; dS - \int \vec{u}\, (\nabla \cdot \vec{u})\; d\vec{x} - \int p\vec{n}\, dS \\ &= -\int \vec{u}\, (\vec{u} \cdot \vec{n})\; dS - \int p\vec{n}\, dS\ . \end{aligned} \tag{2.11}$$

Here $\vec{n}$ is the unit normal which points out of the surface by convention. Under the same boundary conditions as were used to simplify equation (2.8), and taking advantage of axial symmetry to simplify the surface integral of the pressure, the rate of change of the total momentum in the axial direction is,

$$\frac{dH_x}{dt} = 2\pi \int_0^R u^2 r\, dr - 2\pi \int_0^{R_\infty} \left[p\left(x_\infty, r\right) - p\left(x_0, r\right)\right] r\, dr\ . \tag{2.12}$$

[40] define an added force measured during experimentation which they term the pressure impulse,

$$I_P(t) = \int_0^t \int_A \left[p(r,\tau) - p_\infty\right]\; dS\, d\tau, \tag{2.13}$$

where A is the nozzle area and p_∞ is the ambient pressure; $p_\infty = \lim_{x\to+\infty} p(x,0)$. This term can readily be equated to the pressure term of (2.12), since the pressure can be assumed to be uniform at the boundary $x = x_\infty$. To avoid confusion, we will refer to this terms as the pressure momentum, contrary to the term 'pressure impulse' used by Krueger et al. This is because 'pressure impulse' usually refers to the pressure needed to start impulsive motion where the acceleration dominates the convective terms ($\partial u/\partial t \gg \vec{u}\cdot\nabla\vec{u}$), and the pressure can be found from solid body mechanics, see [9]. This is distinctly different from an additional momentum due to over-pressure at the nozzle.

2.3 Kinetic Energy and Shaft Work

The rate of change of kinetic energy of the system, $E = \int \frac{1}{2}\vec{u}^2 dV$, is derived for an incompressible, inviscid control volume in multiple texts [42, 14]. This rate is presented here in vector form,

$$\frac{dE}{dt} = -\int \left(\frac{1}{2}\vec{u}^2 + P\right)\vec{u}\cdot\vec{n}\,dS\ , \tag{2.14}$$

where $\frac{1}{2}\vec{u}^2 + P$ is referred to as the 'total head' in some thermodynamic control volume analysis. Defining this surface integral in the axisymmetric coordinate system, taking into account the symmetry at the surface $r = R_\infty$, results in,

$$\frac{dE}{dt} = -\pi\int_0^{R_\infty} \left[\left(u^2+v^2+2P\right)ur\right]_{x_0}^{x_\infty} dr\ , \tag{2.15}$$

The surface integral can again be eliminated at the farfield boundary, using the same order of magnitude analysis as was used to eliminate the surface integrals in the impulse equation. By this analysis the integrand terms of (2.15), excluding the pressure term, scale with x^{-3} to the leading power of x, at the $x = x_\infty$ boundary. Since the pressure at this boundary is P_∞, a finite constant, the pressure integrand term scales with $x^{-1}r^{-1}$. Therefore, the integrand terms vanish faster than the surface of integration expands to infinity, and the surface integral of equation (2.15) only needs to be evaluated at the entrance boundary,

$$\frac{dE}{dt} = \pi\int_0^{R_\infty} \left[\left(u^2+v^2+2P\right)ur\right]_{x=x_0} dr\ . \tag{2.16}$$

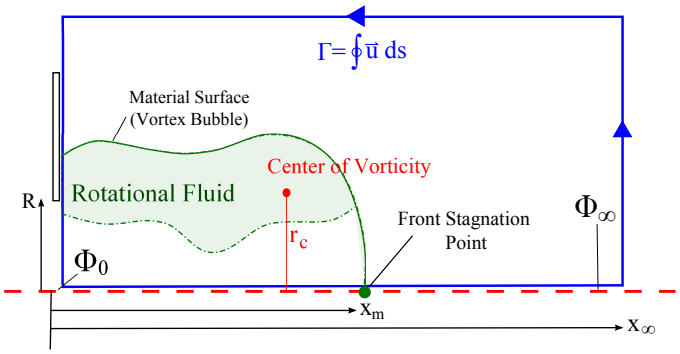

Figure 2.2: The emanating jet flow is depicted along with the line integral used to calculate jet circulation, which is the closed blue loop. The velocity potential at the entrance boundary and farfield boundary are marked by Φ_0 and Φ_∞ respectively, all of these are on the axis of symmetry.

Therefore, the kinetic energy of the jet is dependent on both the radial velocity, v, and the pressure at the nozzle exit plane, P, both of which are non trivial in non-parallel jet flows.

We assume that there is no heat transfer taking place, and there is also no change in potential energy since the control volume remains stationary. Therefore, there is no net change in internal energy and the rate at which shaft work must be performed by a mechanical system used to generate the flow is equal to the rate of change of kinetic energy of the system, $\dot{W} = \frac{dE}{dt}$.

In order to calculate equation (2.16) for an arbitrary jet flow entering the control volume, the pressure along the entrance boundary must be determined in terms of the jet velocity profiles. This analysis is presented next.

2.4 Pressure at the Nozzle Plane

Since the starting jet is assumed to be axisymmetric, several simplifying assumptions can be made which aid greatly in determination of the pressure at the entrance plane. The pressure is determined in terms of the velocity potential along the axis of symmetry; moreover, this analysis does not require that the vortex ring leading material surface be equated to translating flat plate potential flow like the model derived in [39].

The axis of symmetry is a streamline, given the axisymmetric condition that radial velocity is equal to zero at the centerline. The axis of symmetry is also devoid of vorticity if the axial velocity

profile is assumed to be continuous and smooth across the axis. Therefore, the pressure along this axis can be described by the unsteady form of Bernoulli's equation,

$$\frac{\partial \varphi}{\partial t} + \frac{1}{2}\vec{u}^2 + P = f(t) \; , \tag{2.17}$$

where φ is the velocity potential, and $f(t)$ is an arbitrary function which only depends on time. Here we replace the velocity potential, φ, with Φ, defined as $\Phi = \varphi + \int_0^t f(\tau)\, d\tau$, so that Bernoulli's equation can be written without dependence on $f(t)$, but the new potential still has the same gradient, $\nabla\Phi = \nabla\varphi$. Since the axis of symmetry is irrotational, the velocity potential can be determined from the axial velocity by definition of the potential function, $\nabla\varphi \equiv \vec{u}$. In cylindrical coordinates the axial velocity becomes $u = \partial\varphi/\partial x = \partial\Phi/\partial x$. This flow is illustrated in Figure 2.2. At the far boundary in the axial direction, $x = x_\infty$, the fluid is at stagnation pressure P_∞. Integrating the axial velocity we have a relationship between velocity potential at the far boundary, Φ_∞, and the potential at the entrance plane, Φ_0,

$$\Phi_0 = \Phi_\infty - \int_{x_0}^{x_\infty} u\, dx \; . \tag{2.18}$$

The velocity along the centerline is not easily determined; however, the line integral of this velocity is contained in the total jet circulation. The circulation is, by definition, equal to the closed loop line integral of velocity around the axisymmetric plane, which can be separated into sections. Since the line integrals along the far field boundaries drop to zero, by a similar order of magnitude analysis as that presented in the previous section, the circulation is,

$$\Gamma = \oint \vec{u} \cdot \vec{dl} = \int_{R_\infty}^{0} -v\, dr + \int_{x_0}^{x_\infty} u\, dx \; . \tag{2.19}$$

Combining equations (2.18) and (2.19) gives the potential at the entrance plane as,

$$\Phi_0 = \Phi_\infty - \left[\Gamma - \int_0^{R_\infty} v\, dr\right] \; . \tag{2.20}$$

Applying Bernoulli's equation at the entrance and the farfield boundaries results in the relation,

$$\frac{\partial \Phi_0}{\partial t} + \frac{1}{2}u_0^2 + P_0 = \frac{\partial \Phi_\infty}{\partial t} + P_\infty \; , \tag{2.21}$$

where P_0 is the pressure on the centerline at entrance plane and u_0 is the centerline velocity at the entrance plane. Inserting the derivative of equation (2.20), and noting that the boundary $r = R_\infty$ remains stationary relates the centerline pressure to circulation and entrance kinematics,

$$P_0 = P_\infty + \frac{d\Gamma}{dt} - \int_0^{R_\infty} \frac{\partial v}{\partial t}\, dr - \frac{1}{2}u_0^2 \,. \tag{2.22}$$

The rate of change of circulation is equal to the flux of vorticity across the nozzle exit plane, inserting equation (2.5) into (2.22) allows the pressure on the centerline to be calculated,

$$P_0 = P_\infty + \int_0^{R_\infty} \left(u\frac{\partial v}{\partial x} - \frac{\partial v}{\partial t} \right) dr \,. \tag{2.23}$$

The pressure along the rest of the entrance plane can be determined by integrating the momentum equation in the radial direction,

$$P(r) = P_0 - \int_0^{r} \left(u\frac{\partial v}{\partial x} + \frac{\partial v}{\partial t} \right) d\varpi - \frac{1}{2}v(r)^2 \,, \tag{2.24}$$

where ϖ is a dummy variable for the radius of integration. Finally combining equations (2.23) and (2.24) gives the pressure distribution along the entrance plane in terms of surface integrals at the entrance boundary only involving jet velocity profiles,

$$P(r) = P_\infty - \frac{1}{2}v(r)^2 + \int_r^{R_\infty} u\frac{\partial v}{\partial x}\, dr - \int_0^{R_\infty} \frac{\partial v}{\partial t}\left(2 - H(\varpi - r)\right) d\varpi \,, \tag{2.25}$$

where H is the heaviside function, defined $H = 0$ for $\varpi < r$ and $H = 1$ for $\varpi \geq r$.

Now the pressure and kinetic energy of any axisymmetric jet flow can be determined as long as the jet kinematics are known at the entrance boundary. Chapter 4 describes the velocity profiles of jets which are expelled through nozzles to create both parallel starting jet flows and ones with a converging radial velocity. These profiles are then applied to the equations for circulation, impulse, pressure, and energy that were just derived, and compared to actual circulation, impulse, and energy of jet flows measured experimentally.

Chapter 3

Experimental Setup

To create the jet flows studied here a prototype thruster/flow generator was developed which can independently control all of the different characteristic jetting parameters. The vortex generator mechanism is sealed within a transparent canister which is submerged fully within a fluid reservoir in a static testing tank. A vertical rod runs from the canister to a frame mounting structure keeping the canister stationary and allowing direct measurement the thrust produced. A flow visualization setup is used to film the resulting jet flows in order to capture jet velocity fields using standard DPIV techniques. A data acquisition assembly sends driving signals to the motor of the vortex generator, sends trigger signals to the camera, records motor encoder data, and records load cell thrust measurements. All of these components are described here in detail.

3.1 Prototype Thruster/Vortex Generator

The thruster of this investigation consists of a clear canister (allowing immediate observation of any leaks, or mechanical issues), which is sealed off by a set of steel endcaps. The bottom endcap has a large circular opening which leads to an internal fluid cavity. Fluid is forced in and out of the opening by driving a plunger in the internal cavity. A CAD model of the internal mechanism of the thruster canister is shown in Figure 3.1, along with a conceptual diagram of the jetting process. The plunger is a semi-flexible accordion style bellows, which is reinforced by a helically wound metal rod to minimize changes in diameter, while allowing expansion of the plunger in the axial direction. This arrangement was chosen so that the volume of fluid ejected has a linear proportionality to

the deflection of the plunger. A set of nozzles were fabricated to attach to the thruster opening providing a wide range of jet flow characteristics.

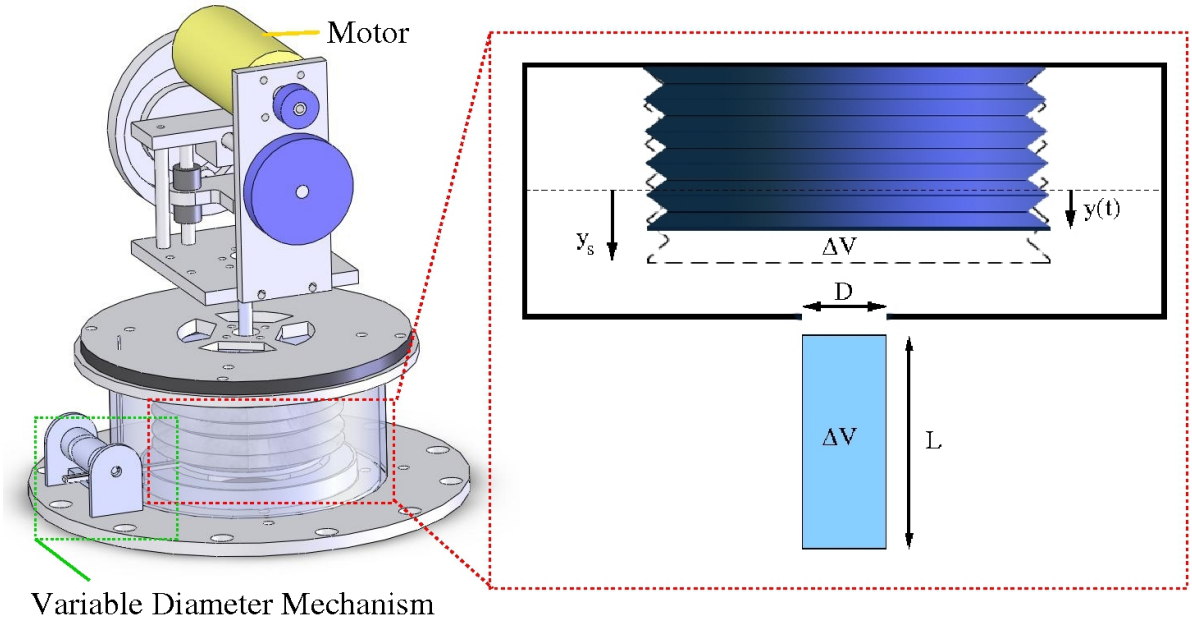

Figure 3.1: A CAD model of the vortex generator internal mechanism is shown along with a blown up schematic depiction of the internal cavity section

Static Nozzle Configurations There are two basic types of nozzles that are used in this study. Jet flows which leave the nozzle with nearly parallel streamlines (no radial velocity) are created using a tube nozzle, which is a long tube connected to the end of the cavity. The tube is sufficiently long, $> 6D$, to ensure parallel flow at the exit. The outside of the tube is tapered at the exit with an angle, γ, as shown in Figure 3.2. The tube nozzle is fabricated with a very small γ, very close to 11°. Converging starting jets are created with an orifice nozzle which is simply a flat plate with a central circular orifice. The converging internal streamlines persist downstream creating the converging jet flow.

Variable Diameter Nozzle The variable diameter nozzle is functionally very similar to the orifice nozzle. The mechanism is similar to an iris diaphragm/shutter used in photography, where a set of interwoven leaves can be actuated to increase or decrease the central opening. Though the opening is not a perfect circle, technically a regular 20 point polygon (corresponding

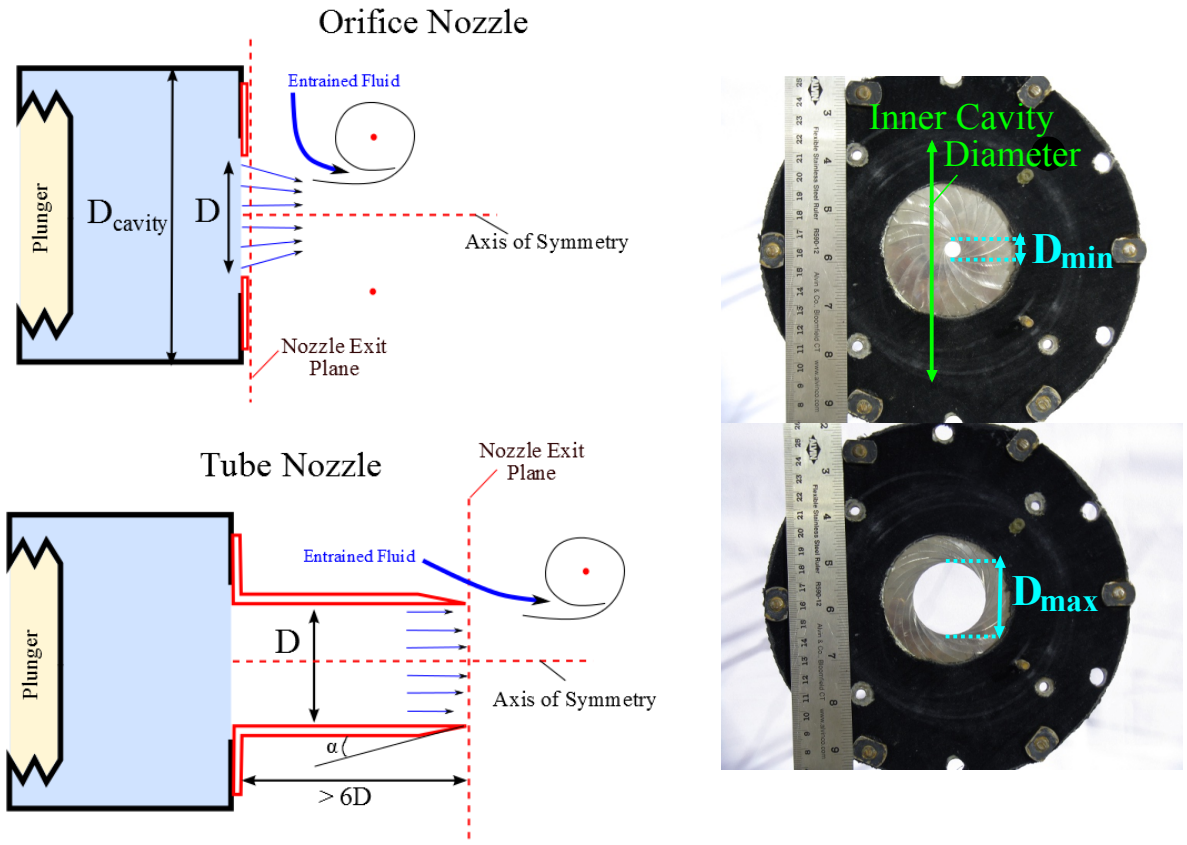

(a) Nozzle Configurations (b) Variable Diameter Nozzle

Figure 3.2: Conceptual diagram of the layout of different nozzles used to generate various jet flows for this experimentation (a) and the variable diameter nozzle shown at the limits of diameter actuation (b).

to the 20 leaves), It will be approximated as a circular opening diameter. The variable diameter nozzle is constructed out of thin stainless steel leaves, about 0.5 mm (0.02 in) in thickness. The nozzle can be actuated from 0.64 cm (0.25 in) to 4.5 cm (1.75 in) in diameter. The mechanism is shown at in Figure 3.2 at the maximum and minimum achievable diameters.

3.2 Testing Tank

The prototype thruster is placed in a controlled testing tank which was custom designed for this experiment. The thruster tank consists of an acrylic box measuring 4 ft (1.2 m) wide 3 ft. (0.91 m) deep and 6.5 ft. (2 m) tall, and is supported by an outer steel frame. The frame applies forces to the acrylic walls via individually tensioned pads, in order to counteract the water pressure forces. The construction of the thruster tank allows for complete visual access from all sides (including the bottom), to facilitate filming of the thruster jet flow. A schematic diagram of the thruster tank as well as an image of the tank itself is shown in Figure 3.2.

3.3 Flow Visualization

The flow visualization setup is composed of a high speed camera and illumination apparatus. As depicted in Figure 3.2, a 2D cross section of the flow is illuminated with a laser sheet. The flow is seeded with reflective polyamide particles ≈ 50 μm in diameter, with a density of 1.03 gcm^{-3} (manufactured by Dantec Dynamics). The laser sheet is generated by a 1W solid state 532 nm laser (Aixis GAM 1000B) expanded through a cylindrical lens within the tank. Placing the cylindrical lens within the fluid reservoir minimized the divergence of the laser prior to the sheet making optics, resulting in a laser-sheet thickness of ≈ 1 mm at the nozzle exit plane. The illuminated cross section of the flow is recorded using a high speed digital camera, operating at 150-250 fps depending on the piston velocity. The camera used is a monochrome Phantom v210. This camera has a resolution of 1 Mpixel (1280×800) and a light sensitivity of 6000 ISO, making it suitable for DPIV with the solid state laser.

Figure 3.3: A schematic of the experimental setup (a) as well as a picture of the actual experimental apparatus in operation (b).

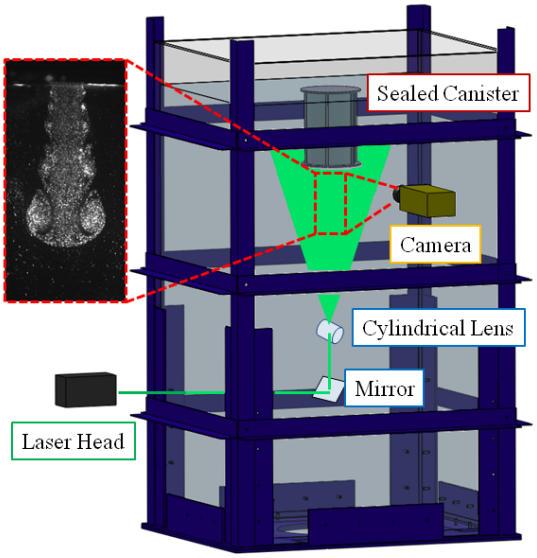

(a) Schematic of Setup

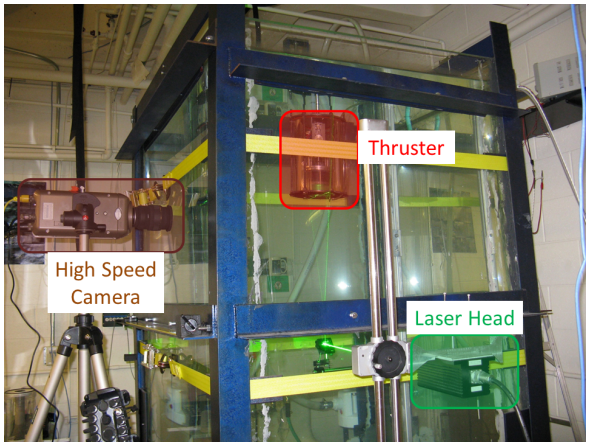

(b) Actual Setup

3.4 DPIV Analysis Description

The high speed video of the jet flow is analyzed using a commercial software, with DPIV algorithms similar to those described in [96, 70], to determine a velocity field $\vec{u} = [u, v]^T$ in the illuminated cross section of the jet flow. Frames (1280×800 pixel resolution), were divided into 36×36 pixel interrogation windows (with 50% overlap), to give the velocity field a 70×44 grid-point resolution (with the long dimension of the image aligned with the axis of symmetry). Strict care was taken to ensure that the laser sheet bisected the flow through the jet axis of symmetry, so that the filmed jet flow corresponds to the axisymmetric flow. An example of the velocity and vorticity fields determined with this process is presented in Figure 3.4.

Again, the flow is assumed to be axisymmetric with no swirl. Therefore, the total circulation, hydrodynamic impulse, and kinetic energy of the control volume can be calculated from the vorticity and velocity fields, [80, 45],

$$\begin{aligned} \Gamma &= \int_{x_0}^{x_\infty} \int_0^{R_\infty} \omega \, dr \, dx \, , \\ I &= \pi \int_{x_0}^{x_\infty} \int_0^{R_\infty} \omega r^2 \, dr \, dx \, . \\ E &= \pi \int_{x_0}^{x_\infty} \int_0^{R_\infty} \left(u^2 + v^2\right) r \, dr \, dx \, . \end{aligned} \tag{3.1}$$

The axisymmetric formulation implies that the velocity/vorticity field is known for a single half plane extending from the axis of symmetry. The DPIV analysis determines the velocity field for the entire plane which gives two axisymmetric sections π rad out of phase. The axis of symmetry, which separates the two half-planes, is determined in the image as the mid-line between the peak in positive and negative vorticity, and is shown as the dashed line in Figure 3.4. In order to determine the axis of symmetry with sub piv-window accuracy, the peak location is interpolated from a small vorticity field surrounding the peak measured value. In general quantities of interest will be calculated for both half planes given by DPIV analysis and averaged to give a more accurate value.

The boundary of the vortex ring core, δ, is determined from the vorticity field as an isovorticity

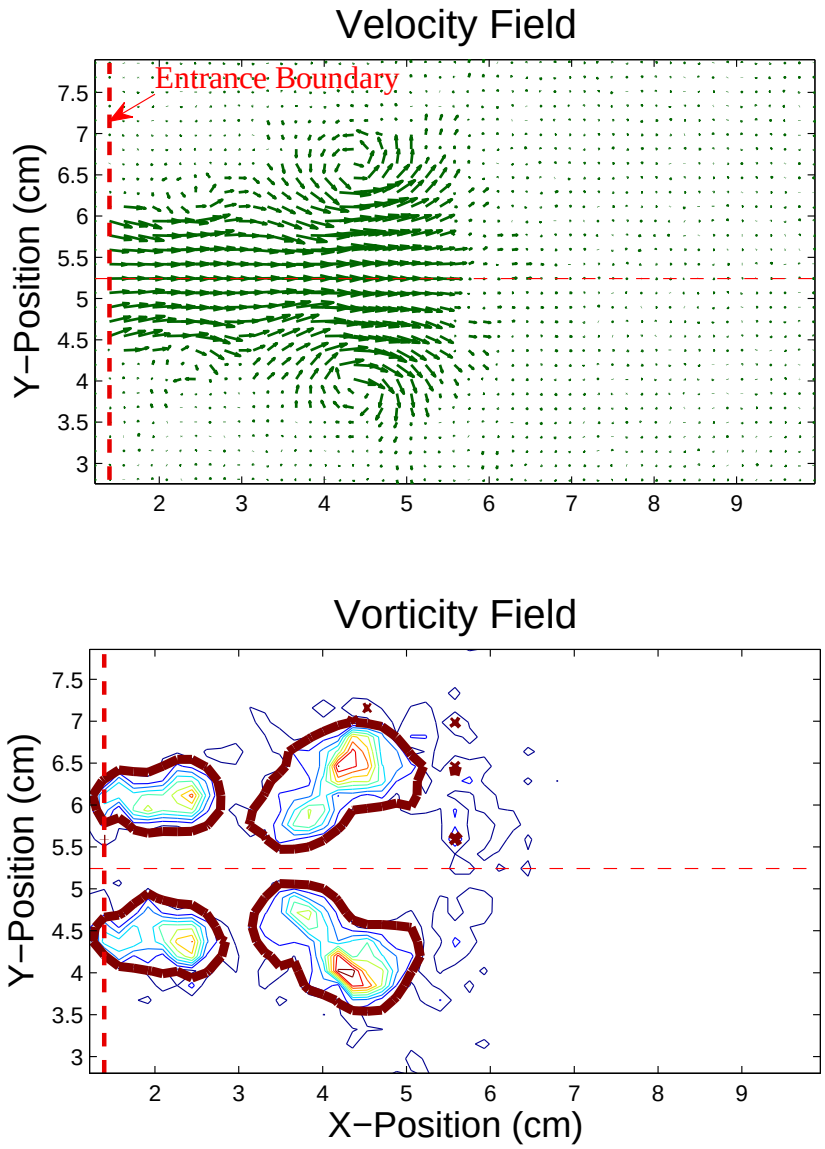

Figure 3.4: Sample image of the velocity field and vorticity field determined from the DPIV analysis. The axis of symmetry is shown by the dashed red line running horizontal through the center and the vertical dashed line marks the nozzle exit plane. This sample flow field was generated by a jet ejected from an orifice nozzle with a nozzle radius of 0.93 cm and a piston velocity of 6.8cm s^{-1}. This corresponds to experimental case 4, as summarized in table 6.1

contour at some small threshold value ω_ϵ, which is above the background noise level. It should be noted that the isovorticity contour corresponding to the vortex boundary often includes multiple rings in the trailing wake. Therefore, the leading vortex ring core boundary is determined as the closed isovorticity contour enclosing the peak vorticity. Figure 3.4 also shows the vorticity contours used to identify core boundaries. The isovorticity contour at $\omega_\epsilon = 2$ cm^{2}s^{-1} is depicted by the thicker red contour, which is composed of two distinct closed contours; one around the leading vortex ring and the other around a vortex ring in the trailing wake. Defining the core area, A_c, as the region encompassed by the core boundary, δ, the circulation, impulse, and energy of the leading vortex ring can be determined from the same integrands as the total quantities with a closed boundary of integration.

$$\begin{aligned} \Gamma_c &= \oint_{A_c} \omega \, dr dx \ , \\ I_c &= \pi \oint_{A_c} \omega r^2 \, dr dx \ , \\ E_c &= \pi \oint_{A_c} \left(u^2 + v^2\right) r \, dr dx \ . \end{aligned} \tag{3.2}$$

Of course the center of vorticity of the vortex ring, which will be utilized for the model in Chapter 5, is not necessarily at the same location as the peak vorticity value. The definition of the center of vorticity is given in [42, 49] in terms of vorticity integral quantities. Restricting the integrals to the vortex core area, A_c, allows the vortex center of vorticity to be determined,

$$l^2 = \frac{\int_{A_c} \omega_\phi r^2 \, dr dx}{\int_{A_c} \omega_\phi \, dr dx} \ , \quad x_c = \frac{\int_{A_c} \omega_\phi r^2 x \, dr dx}{\int_{A_c} \omega_\phi r^2 \, dr dx} \ . \tag{3.3}$$

Now the invariants of motion of experimentally generated jet flows can be determined from DPIV data, along with characteristics of the leading vortex ring, which allows validation of the jet and vortex ring modeling.

Chapter 4

Velocity Profiles at the Exit of a Family of Nozzles

The evolution of circulation, hydrodynamic impulse, and kinetic energy of the control volume, have been derived in terms of surface integrals of the jet kinematics along the entrance plane in equations (2.5), (2.10), and (2.16), respectively, in Chapter 2. The pressure profile along the entrance plane which is needed to calculate the kinetic energy is described by equation (2.25). The equations are valid for determining the circulation, impulse, and energy of any inviscid axisymmetric starting jet flow, provided the exact kinematics are known at the source of the flow. The velocity profiles of various starting jets are heavily dependent on the nozzle used to generate the flow. As was mentioned a starting jet expelled through a long cylindrical nozzle will create a nearly parallel starting jet, whereas converging conical nozzles and the flat plate orifice nozzle create a starting jet with a converging radial velocity at the entrance boundary. Here we describe jet velocity profiles for starting jets created from both tube and orifice nozzles as observed in previous experiments and measured here. We also present multiple approximations to these profiles. Using the approximated jet velocity profiles we calculate the rate of circulation, impulse, and energy added to the control volume in terms of characteristic parameters.

4.1 Axial Velocity Profile, u

The axial jet velocity for flows expelled from tube nozzles has been extensively studied. The jet velocity is a dynamic function of both radial position and time, even for programs with constant volume flux. At the onset of the flow the axial jet velocity is nearly uniform with a small peak near

the edge due to the influence of the primary vortex ring. This peak is very similar to Richardson's annular effect observed in oscillating pipe flow [73], and is seen for jets expelled through both tube nozzles [18] and plate/conical nozzles [77]. As the piston continues to push out fluid, the boundary layer on the cylinder wall becomes more developed and the jet velocity profile becomes parabolic in tube nozzle flows. Since there is minimal boundary layer development on the orifice nozzle prior to ejection, the development of a parabolic velocity profile is less pronounced, or completely absent if the ratio of the nozzle to cavity diameter is low enough [77], and a small peak near the edge is observed even in the final development stages. The axial velocity profile at the nozzle exit plane (as determined from DPIV analysis, see section 3.4) is shown for starting jets ejected from both tube and orifice nozzles in figure 4.1.

For a nozzle of radius, R, which has a volume flux, Ω, passing through it, the piston velocity is defined $u_p \equiv \Omega/\pi R^2$. This terminology is derived from piston cylinder mechanisms, but the definition is valid for all jetting mechanisms.

4.1.1 1D Slug Model

The simplest approximation of the jet flow at the nozzle plane is the 1D slug model, which makes the assumption that the jet is ejected with a uniform axial velocity and no radial velocity, $u(r) = u_p$ for $0 \leq r < R$. Under these assumptions equations (2.5), (2.10), (2.25), and (2.16) simplify to the more familiar form,

$$\frac{d\Gamma}{dt}_{1\mathrm{D}} = \frac{1}{2}u_p^2 \,, \tag{4.1a}$$

$$\frac{dI}{dt}_{1\mathrm{D}} = \pi u_p^2 R^2 \,, \tag{4.1b}$$

$$P_{1\mathrm{D}} = P_\infty \,, \tag{4.1c}$$

$$\frac{dE}{dt}_{1\mathrm{D}} = \frac{\pi}{2}u_p^3 R^2 \,. \tag{4.1d}$$

This approximation is used frequently for simple calculations, but is only accurate for a very limited range of jet flows. Therefore we will define a more general axial velocity profile which can be adjusted to fit jet flows found at the outlet of various nozzles at any given time.

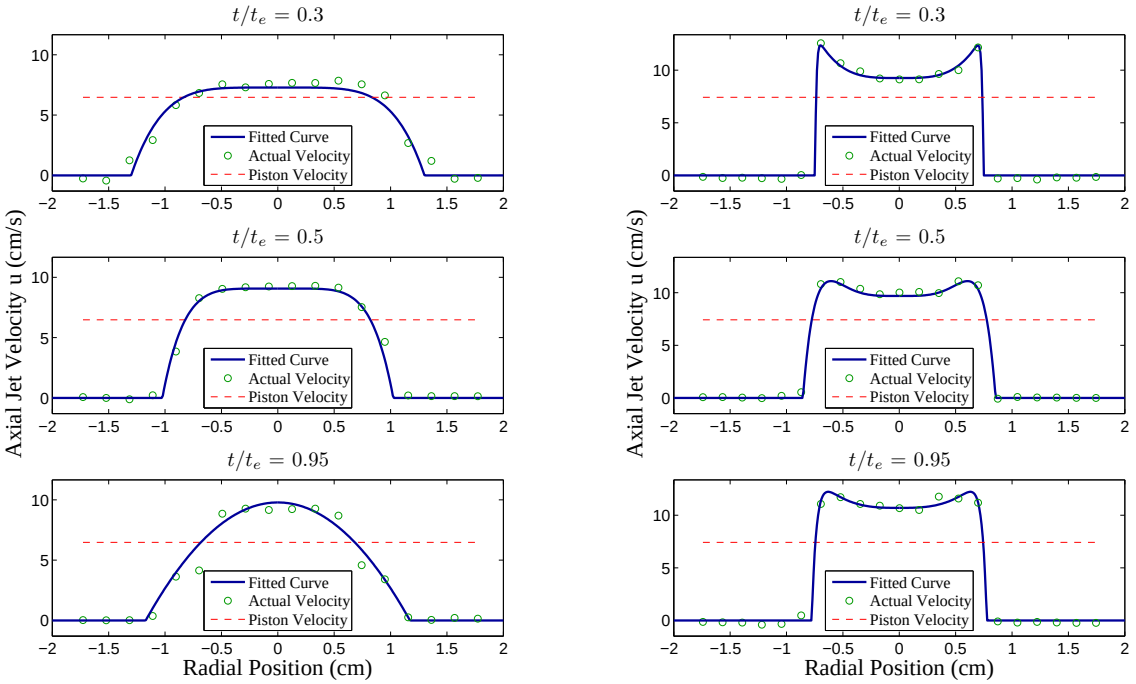

(a) Tube Nozzle

(b) Orifice Nozzle

Figure 4.1: Axial velocity profile at the nozzle exit throughout pulsation for a (a) tube nozzle and (b) orifice nozzle. The data was fitted to a curve of the form (4.2) described in section 4.1.2. The velocity profiles shown in (a) and (b) correspond to experimental cases 2 and 4, respectively, as summarized in Table 6.1.

4.1.2 Shape Factor Model

There is a large variation in axial velocity profile between different types of nozzles, and at different formation times. As a second order approximation to the axial velocity profile we define a generic polynomial velocity profile, which allows the jet flows emanating from any nozzle at any stage of formation to be defined by a limited number of parameters.

$$u(r) = a\left(\frac{r}{R_{\text{eff}}}\right)^n - (u_0 + a)\left(\frac{r}{R_{\text{eff}}}\right)^m + u_o \ , \tag{4.2}$$

where R_{eff} is the 'effective radius' which is the radial extent of the jet velocity crossing the nozzle exit plane (for the present explanation it suffices to consider this the nozzle radius R), and a, m and n are coefficients which control the shape of the velocity profile. This velocity profile is defined on the domain $0 \leq r < R_{\text{eff}}$, outside of this domain the axial velocity is assumed to be zero. The effective mass flux, Ω_{eff}, is the total mass flux crossing the nozzle exit plane, which is the sum of the mass flux coming from the jet source and the flux of fluid across the entrance boundary which is entrained into the jet. In accordance with the definition of the piston velocity we have an 'effective piston velocity' defined by the effective radius and mass flux, $u_{\text{eff}} = \Omega_{\text{eff}}/\pi R_{\text{eff}}^2$. Restricting the axial velocity profiles to a family of solutions whose integral over the nozzle exit plane is the effective mass flux, the centerline velocity can be defined in terms of the shape factors,

$$u_0 = \frac{\Omega_{\text{eff}}}{\pi R_{\text{eff}}^2}\frac{m+2}{m} - a\frac{2(m-n)}{m(n+2)} \ . \tag{4.3}$$

For flows generated through orifice nozzles the effective mass flux, effective piston velocity and effective radius are equal to the mass flux, piston velocity, and nozzle radius, respectively; however, these values differ for flows generated through tube nozzles.

This general form axial velocity profile can be used to describe several useful jet flows, which are graphically described in figure 4.2. A flow with peaks at the outer edges can be described by setting $a < 0$. The profile has a single peak at the centerline for the special case where $a = 0$, or $m = n$. In this case the profile describes a fully developed Poiseuille flow with shape factor $m = 2$. The hypothetical top hat velocity profile (1D slug model) is the limit of the generic profile as the

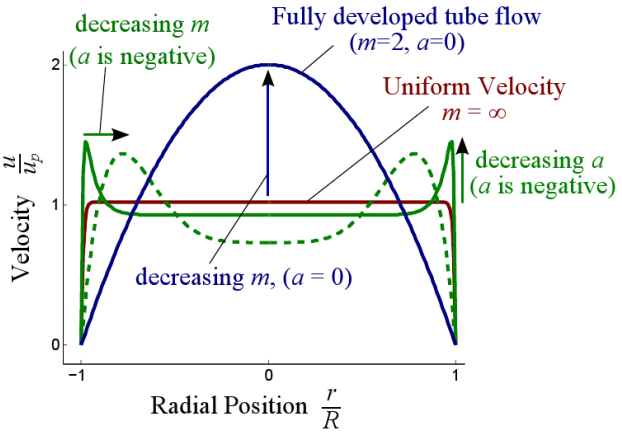

Figure 4.2: Various jet velocity profiles available to the general axial velocity profile. The effect of adjusting the shape factors a and m are shown with graphical examples, and n is set much higher than m.

exponential coefficients, m and n, approach infinity, independent of a. If a becomes large and positive the velocity profile develops a local minimum, which is negative, before returning to zero at the effective radius. In order to maintain a purely positive axial velocity profile the constraint, $\partial u/\partial r \leq 0$, must be imposed at the point $r = R_{\text{eff}}$; which directly translates to the constraint $a \leq \frac{u_0 m}{n-m}$.

If it is assumed that the fluid crosses the entrance plane with no radial velocity and an axial velocity profile defined by Equations (4.2) and (4.3) then the rate of change of circulation, impulse, and energy of the control volume can be calculated from equations (2.5), (2.10), and (2.16), again with zero radial velocity $P = P_\infty$,

$$\frac{d\Gamma}{dt}_{\text{SF}} = \frac{1}{2}u_0^2 = \frac{1}{2}\left[\frac{\Omega_{\text{eff}}}{\pi R^2}\frac{m+2}{m} - a\frac{2(m-n)}{m(n+2)}\right]^2 , \tag{4.4a}$$

$$\begin{aligned}\frac{dI}{dt}_{\text{SF}} = \rho 2\pi R_{\text{eff}}^2 \Bigg[&\frac{a^2}{2n+1} - \frac{2a\,(u_0+a)}{m+n+2} + \frac{(u_0+a)^2}{2m+2} - \frac{2u_0\,(u_0+a)}{m+2} \\ &+ \frac{2au_0}{n+2} + \frac{1}{2}u_0^2\Bigg] ,\end{aligned} \tag{4.4b}$$

$$\begin{aligned}\frac{dE}{dt}_{\text{SF}} = \pi R^2 \Bigg[&\frac{u_0^3}{2} + \frac{a^3}{3n+2} + \frac{3a^2u_0}{2n+2} + \frac{3au_0^2}{n+2} - \frac{(a+u_0)^3}{3m+2} - \frac{3u_0^2\,(a+u_0)}{m+2} \\ &+ \frac{3u_0\,(a+u_0)^2}{2m+2} - \frac{3a^2\,(a+u_0)}{m+2n+2} + \frac{3a\,(a+u_0)^2}{2m+n+2} - \frac{6au_0\,(a+u_0)}{m+n+2}\Bigg] .\end{aligned} \tag{4.4c}$$

In a crude sense the shape factor m can be considered inversely proportional to the thickness of the shear layer coming into the control volume. As m increases the axial velocity profile approaches the uniform velocity distribution, and the circulation, impulse, and energy predicted by the shape factor approximation asymptotically approach the circulation, impulse, and energy of the 1D slug model.

So far the jet velocity characterization has only described the axial velocity profile for jet flows. Next we define a characterization for the radial velocity profile in non-parallel starting jets.

4.2 Radial Velocity Profile (v)

At the onset of pulsation the emerging fluid rapidly rolls into a vortex ring. As a result of the primary vortex ring's close proximity to the nozzle exit plane, the emerging flow from both nozzles experiences an induced velocity in the radial direction. As the vortex ring travels downstream, a jet emanating from the tube nozzle quickly becomes parallel; while the flow emerging from the orifice nozzle maintains a consistent radial velocity throughout pulsation. It is expected that the radial component of velocity reach a maximum near the edge of the nozzle. Experimental DPIV velocity data shows that this is the case and more specifically, that the radial velocity profile at the nozzle is nearly linear, at least for orifice nozzles. A typical radial velocity profile at the exit of an orifice nozzle was averaged over time and is shown in figure 4.3, along with the velocity gradient $\partial v/\partial x$.

2D Model The simplest radial velocity profile (keeping in mind that axisymmetric flows must have no radial velocity at the axis of symmetry) is a linear proportionality, $v(r) = k_1 r$ for $0 \leq r < R$. In fact, the radial velocity profile at the exit of an orifice nozzle is seen to be very close to linear, as was just illustrated. The gradient of the radial velocity in the axial direction will also be assumed to be linear over the same domain, $\partial v/\partial x = k_2 r$, which is a fair approximation. A linear fit to both the radial velocity profile and the velocity gradient profile are also shown in figure 4.3. Taking these approximations for the radial velocity profile, and again assuming a uniform axial velocity the contributions to circulation, impulse, nozzle pressure, and energy from the radial velocity terms are calculated from (2.5), (2.10), (2.25), and (2.16) to be,

$$\left.\frac{d\Gamma}{dt}\right|_{2\mathrm{D}} = \frac{1}{2}k_2 u_p R^2 \ , \tag{4.5a}$$

$$\left.\frac{dI}{dt}\right|_{2\mathrm{D}} = \frac{\pi}{4}k_2 u_p R^4 - \frac{\pi}{4}k_1^2 R^4 \ , \tag{4.5b}$$

$$P_{2\mathrm{D}} = \frac{1}{2}R^2\left(u_p k_2 - \frac{\partial k_1}{\partial t}\right) - \frac{1}{2}r^2\left(k_1^2 + u_p k_2 + \frac{\partial k_1}{\partial t}\right) \ , \tag{4.5c}$$

$$\left.\frac{dE}{dt}\right|_{2\mathrm{D}} = \frac{\pi}{4}u_p R^4\left[u_p k_2 - 3\frac{\partial k_1}{\partial t}\right] \ . \tag{4.5d}$$

The slope of the radial velocity, k_1, has the units of s^{-1}, and the slope of the velocity gradient, k_2, has units $\mathrm{cm}^{-1}\mathrm{s}^{-1}$. Additionally, these slopes are dependent on the exact nozzle configuration

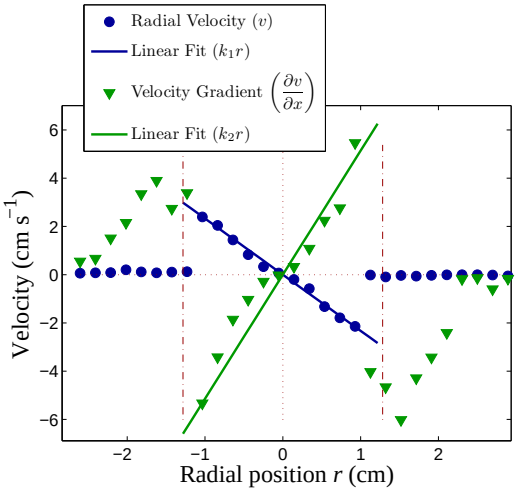

Figure 4.3: Radial velocity and gradient of the radial velocity ($\frac{\partial v}{\partial x}$) as a function of radius, at the at the exit of an orifice nozzle. The jet is expelled with a piston velocity of 6.8 cm s^{-1} and a nozzle radius of 1.3 cm. This corresponds to experimental case 3 as summarized in Table 6.1. Actual values are shown by markers and a linear fit is shown by the solid line

and jetting velocity. Using the piston velocity, u_p, and nozzle diameter, D, as characteristic velocity and length scales the slope of the radial velocity and velocity gradient can be normalized, $k_1^\star = k_1 2R/u_p$, and $k_2^\star = k_2 4R^2/u_p$. Interestingly, if the contributions to circulation, impulse, and energy from radial velocity terms are calculated with respect to the non-dimensional parameters $k_1^\star$ and $k_2^\star$ they take on a similar dependency to piston velocity and nozzle radius as the 1D slug model, which is

$$\frac{d\Gamma}{dt}_{2\mathrm{D}} = \frac{1}{8}u_p^2 k_2^\star = \frac{d\Gamma}{dt}_{1\mathrm{D}} \frac{k_2^\star}{4} , \tag{4.6a}$$

$$\frac{dI}{dt}_{2\mathrm{D}} = \frac{\pi}{16}u_p^2 R^2 \left(k_2^\star - k_1^{\star 2}\right) = \frac{dI}{dt}_{1\mathrm{D}} \frac{k_2^\star - k_1^{\star 2}}{16} , \tag{4.6b}$$

$$P_{2\mathrm{D}} = \frac{1}{8}u_p^2 \left[k_2^\star - \left(\frac{r}{R}\right)^2 \left(k_2^\star + k_1^{\star 2}\right)\right] = \frac{d\Gamma}{dt}_{1\mathrm{D}} \frac{k_2^\star - \left(\frac{r}{R}\right)^2 \left(k_2^\star + k_1^{\star 2}\right)}{4} , \tag{4.6c}$$

$$\frac{dE}{dt}_{2\mathrm{D}} = \frac{\pi}{16}u_p^3 R^2 k_2^\star = \frac{dE}{dt}_{1\mathrm{D}} \frac{k_2^\star}{8} . \tag{4.6d}$$

The contributions due to the radial velocity are calculated assuming uniform axial velocity for simplicity; however, these contributions will later be added to the shape factor model to give a reasonable approximation. Though the most accurate method would be to use the generic axial profile (4.2) when calculating the contributions from non-zero radial velocity terms (4.5), the small increase in accuracy does not justify the increased complexity of the radial contribution terms, and equations (4.6) will be used to describe the contributions from radial velocity for all cases.

Chapter 5

Jet and Vortex Ring Modeling

5.1 Characteristic Parameters

There are several features which should be considered when trying to characterize jet flows and the resulting vortex rings. A parameter which is useful when describing any flow is the Reynolds number, Re. Starting jet flows specifically are often characterized by a quantity known as the formation time.

5.1.1 Reynolds Number

The Reynolds number is often defined for jet flows as,

$$Re = \frac{2\Gamma_0}{\nu} \ , \tag{5.1}$$

where Γ_0 is the total circulation of the jet flow, and ν is the kinematic viscosity of the fluid. Γ_0 is often approximated from the 1D slug model (4.1), but we would like to avoid this definition, since it ignores the contributions from non-zero radial velocity terms. For any Reynolds number presented herein, Γ_0 will be calculated as the total jet circulation determined from DPIV, just after pulsation has stopped.

Glezer [25] showed that starting jets/vortex rings become turbulent at a critical Re of 25000. This critical Reynolds number is significantly lower for pulsatile jets, as is described in Appendix A.

5.1.2 Formation Time

The formation time is a dimensionless measure of time since initiation of the flow normalized by the piston velocity and a characteristic diameter. Formation time is defined by Gharib et al. [23] to be,

$$t^\star = \frac{\int_0^t u_p \, d\tau}{D} \, , \tag{5.2}$$

where D is the characteristic diameter which is the nozzle diameter for jets with static nozzles. The formation time is equal to the stroke ration, L/D, at the final formation time, for cylinder piston devices. Therefore, we will define the stroke ration as the formation time at the end of pulsation for all cases. The definition of formation time becomes ambiguous for jet flows expelled through variable diameter nozzles, and we need to define a characteristic diameter for the case of dynamic nozzles. Dabiri and Gharib [17] suggest,

$$t^\star_{\mathrm{DG}} = \int_0^t \frac{u_p}{D} \, d\tau \, , \tag{5.3}$$

as a new definition for the formation time, which seems a natural choice but doesn't necessarily incorporate the dynamics of the problem. We suggest an alternative definition,

$$t^\star_{\mathrm{RMS}} = \frac{\int_0^t u_p \, d\tau}{2R_{\mathrm{RMS}}} \, , \tag{5.4}$$

where R_{RMS} is the root mean square of the nozzle radius, $R_{\mathrm{RMS}} = \left[1/t \int_0^t R^2 \, d\tau\right]^{1/2}$. While both definitions reduce to the original definition for static nozzles, we believe the second is more directly related to the jet dynamics. The energy of the jet nondimensionalized by the circulation and impulse is defined as $\alpha = E_c / \left(I_c^{1/2} \Gamma_c^{3/2}\right)$, as was done in [23, 54, 55, 53, 56]. It can be shown that the formation time is inversely proportional to the dimensionless energy of the jet if the piston velocity and nozzle radius are held constant. If we assume that the axial velocity profile is constant and the radial velocity profile is linear, then the total circulation, impulse and energy of the jet can be calculated as the sum of equations (4.1) and (4.6) multiplied by the total pulsation time.

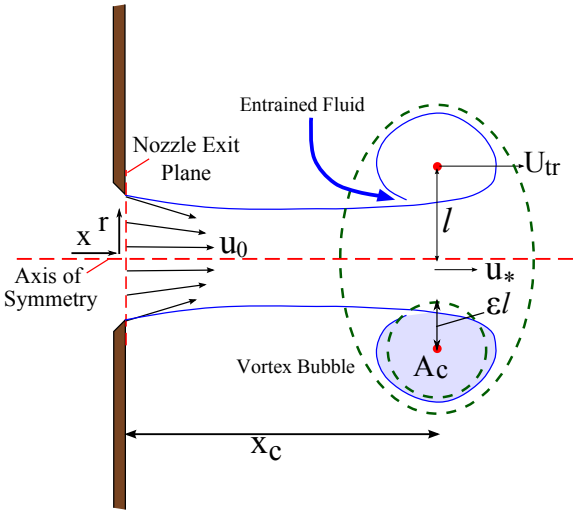

Figure 5.1: Diagram of vortex ring formation, and important flow characteristics

Inserting these into the definition of, α, and rearranging terms results in the relationship,

$$t^\star = \frac{u_p t_e}{D} = \frac{C_\alpha}{\alpha}\ , \qquad C_\alpha = \sqrt{8\pi}\frac{8+k_2^\star}{\left[16+k_2^\star-k_1^{\star 2}\right]^{1/2}\left[4+k_2^\star\right]^{3/2}} = \sqrt{\frac{\pi}{2}}\bigg|_{k_1^\star=k_2^\star=0}\ . \tag{5.5}$$

Meaning that in a very loose generalization a universal formation number corresponds to a minimum dimensionless energy, α, for forming vortex rings. Again holding the piston velocity constant but allowing the nozzle diameter to vary during pulsation, the circulation, impulse, and energy calculated from equations (4.1) and (4.6) will be the same as before, except that the terms R^2 will be replaced with R^2_{RMS}. Plugging these values back into the definition of α results in,

$$\frac{u_p t_e}{2R_{\mathrm{RMS}}} = \frac{C_\alpha}{\alpha}\ . \tag{5.6}$$

Only the definition of formation time in (5.4) preserves the relationship between formation time, $t^\star$, and dimensionless energy, α, for variable diameter jets with constant piston velocity.

5.2 Predicting Formation Number

Here the physical mechanism of vortex ring pinch-off is briefly described as well as a methodology for predicting when the pinch-off will take place for any general starting jet flow. Consider

a starting jet flow which is still attached to the leading vortex ring as depicted in Figure 5.1. The shear layer (tube), which extends into the domain with the jet flow, coils up at the free end starting the vortex ring formation process. As the vortex ring grows the induced velocity on the spiraling shear layer increases, approaching the feeding velocity of the of the starting jet. When the induced velocity surpasses the feeding velocity the trailing shear tube becomes unstable, and the shear layer crossing the vortex boundary (vortex bubble) is driven towards the axis of symmetry under the induction of the vortex ring. Vorticity cancellation at the axis of symmetry causes the shear layer in this region to break, separating the primary vortex ring from the trailing shear layer. The free end of the trailing shear layer rolls into a secondary vortex ring and the primary vortex ring settles upon a stable arrangement. The primary vortex ring quickly travels downstream out of range of the influence of the secondary slower moving vortex ring, and the evolution of the ring becomes only dependent on viscosity (refer to the work of Maxworthy [50, 51]). This process is depicted graphically in Figure 5.2 where a diagram of the shear layer shape is shown alongside actual vorticity contours for several formation times.

In order to model this process and predict jet formation number we need to define a criterion which coincides with the shear layer instability. Similar to Shusser and Gharib [86], we will use the relationship between a characteristic feeding velocity and a characteristic vortex ring velocity to define this criterion; however, the important quantities will be treated very differently and our analysis will not be restricted to specific nozzle configurations, piston velocity programs, or nozzle radius programs. The model of Shusser and Gharib suggested that an appropriate criterion for vortex ring pinch-off is when the propagation velocity of the primary vortex ring surpasses the jet velocity driving the flow, making corrections to the jet velocity based on conservation of mass flux, we will refer to this as the SG criterion throughout this manuscript. We derive an approximation for the translational velocity of the vortex ring and demonstrate that this velocity is sensitive to formation dynamics, and moreover show that this criterion does not exactly coincide with vortex ring pinch-off so that, U_{tr}, might not be the best choice for the characteristic vortex ring velocity. Alternatively, a velocity criterion is proposed here which compares feeding velocity

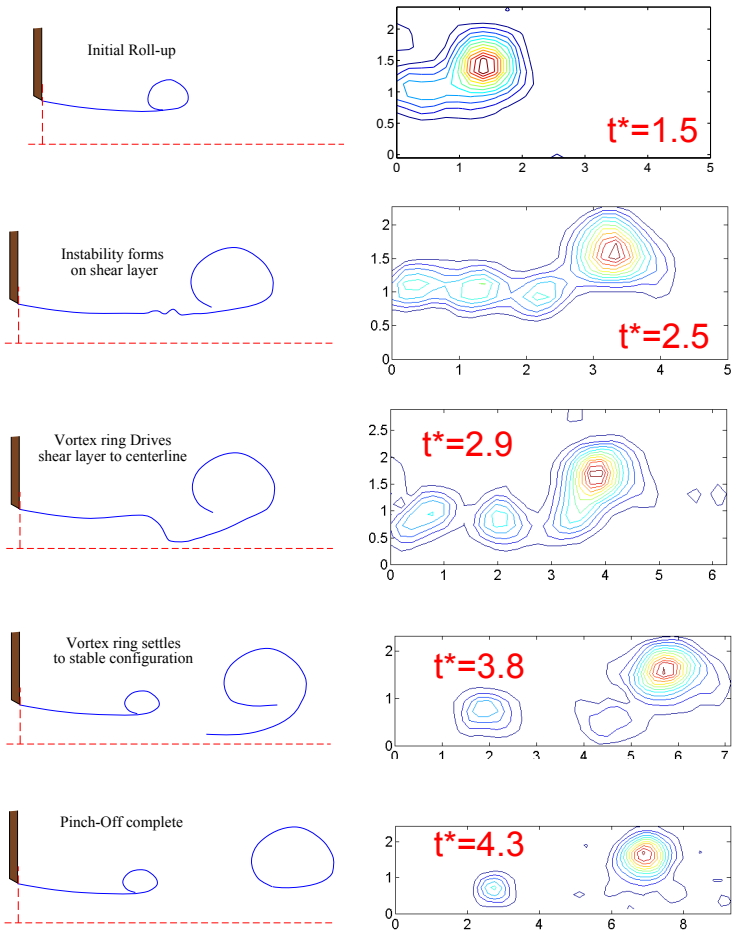

Figure 5.2: At several characteristic formation times the evolution of the shear layer is represented schematically on the left and actual corresponding vorticity contours are shown to the right. The vorticity contours were taken from a converging jet with a stroke ratio $L/D = 2.4$, and piston velocity of $u_p = 6.8$. This corresponds to experimental case 3 as summarized in Table 6.1

to the velocity induced by the forming vortex at a specific interface location, as the characteristic vortex ring velocity. Both the propagation velocity and the induced velocity are approximated from the circulation, impulse, and energy of the vortex ring which determine a unique stable ring configuration. The characteristic feeding velocity will be determined from the velocity profiles at the nozzle exit plane for both pinch-off criteria.

The rate of circulation, impulse, and energy added to a starting jet flow were derived for any starting jet flow in Chapter 2, in terms of the velocity profiles at the nozzle exit plane. These profiles were parameterized for several specific nozzle configurations in Chapter 4, so that the total circulation, impulse, and kinetic energy can be determined for any jet flow if the piston velocity, u_p, radial slopes, $k_1^\star$ and $k_2^\star$, and shape factors, a, m, and n are all known during the entire pulsation.

Next the flow's total invariants of motion will be equated to properties of stable vortex rings to allow a direct comparison of characteristic feeding and vortex ring velocities.

In contrast to the jet modeling presented in previous chapters, the majority of vortex ring models are parameterized by the vortex ring torroidal radius, l, translational velocity, U_{tr}, mean core radius, ϵ, and vorticity density function, Ω. The mean core radius, ϵ, is a dimensionless parameter which describes the 'thickness' of the vortex ring. For a vortex ring of core area A_c, the mean core radius is defined $\epsilon \equiv [A_c/\pi l^2]^{1/2}$, and can range from $\epsilon = 0$ for vortex filaments to $\epsilon = \sqrt{2}$ for Hill's spherical vortex. The vorticity density function is defined $\Omega(x, r) \equiv \omega/r$; if the vorticity density is assumed to be constant then there is a unique set of stable solutions for the vortex core boundary, δ, which we refer to as the Norbury family of vortex rings [60, 59, 21, 22] (or sometimes called 'standard' vortex rings). All vortex rings of this family can be collapsed onto a self-similar ring, and this set of rings varies purely as a function of the mean core radius, ϵ. The circulation, impulse, and energy of Norbury vortices are normalized by torroidal radius, mean core

radius, and vorticity density,

$$\Gamma_c = \left(\Omega\epsilon^2 l^2\right) l\Gamma_N \ , \tag{5.7a}$$

$$I_c = \rho\left(\Omega\epsilon^2 l^2\right) l^3 I_N \ , \tag{5.7b}$$

$$E_c = \rho\left(\Omega\epsilon^2 l^2\right)^2 l^3 E_N \ . \tag{5.7c}$$

Here the subscript c refers to the values of the vortex ring and the subscript N refers to the normalized quantities as presented in [60]. Instead of scaling by the characteristic ring parameters the ring energy can be nondimensionalized by the other two invariants, as in the dimensionless energy, α. Note that this normalization eliminates the geometric scaling terms of (5.7), so that for vortex rings in the Norbury family $\alpha = E_N / \left(I_N^{1/2}\Gamma_N^{3/2}\right)$, which is purely a function of ϵ.

Similarly, if the translational velocity of the vortex ring, U_{tr}, is known then the circulation can also be made dimensionless $\beta = \Gamma_c / \left(I_c^{1/3} U_{tr}^{2/3}\right)$ [56, 53]. Again the dimensionless circulation is purely a function of mean core radius $\beta = \Gamma_N / \left(I_N^{1/3} W^{2/3}\right)$, where W is the normalized translational velocity of the vortex ring defined in [60], $U_{tr} = \left(\Omega\epsilon^2 l^2\right) W$.

Therefore if the circulation, impulse, and energy of the vortex ring are all known, then the mean core radius can be interpolated from the dimensionless energy, α. Additionally the translational velocity can then be determined from the dimensionless circulation corresponding to that mean core radius, $U_{tr} = \Gamma_c^{3/2} / \left(I_c^{1/2}\beta^{3/2}(\epsilon)\right)$. For reference the dimensionless energy and circulation, as determined from [60], are depicted in Figure 5.3(a) with respect to mean core radius. Fortunately the dimensionless energy and circulation have a relationship which eliminates the need to interpolate ϵ. Figure 5.3(b) shows the inverse of the nondimensional energy, $1/\alpha$, plotted with respect to the corresponding nondimensional circulation taken to the power of 3/2, $\beta^{3/2}$. It can be seen in this figure that the quantities have a nearly linear proportionality, which is demonstrated by the line fitted to the form $\beta^{3/2} = c_1 + c_2/\alpha$, with $c_1 = 1.13$ and $c_2 = 0.52$. This allows the translational velocity of the vortex ring to be written in terms of the invariants of motion.

$$U_{tr} = \frac{\Gamma_c^{3/2} E_c}{c_1 I_c^{1/2} E_c + c_2 I_c \Gamma_c^{3/2}} \ , \tag{5.8}$$

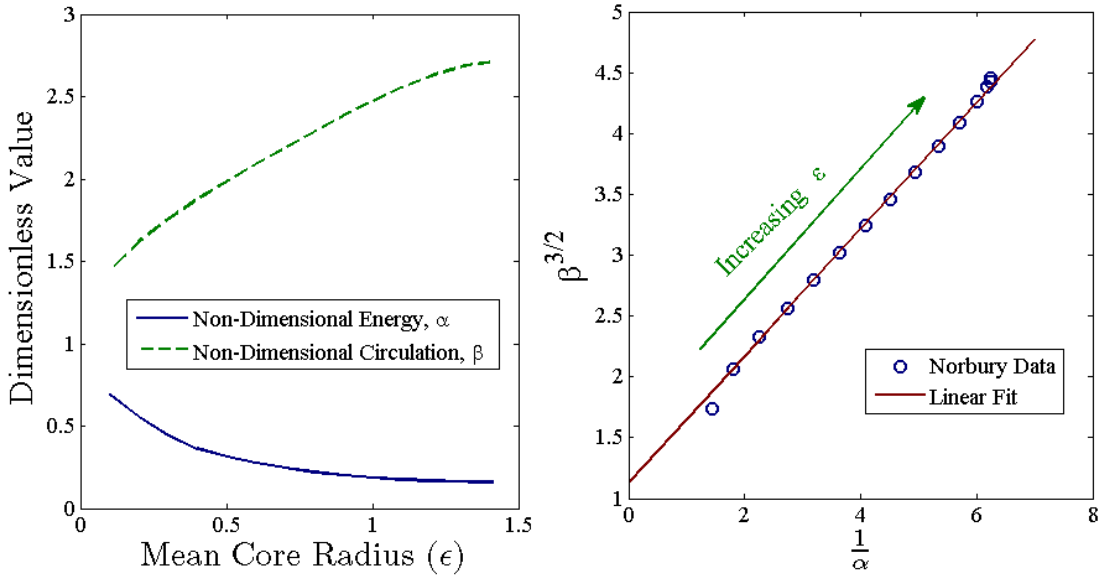

Figure 5.3: Dimensionless energy and circulation, as reported by [60], are shown with respect to mean core radius, ϵ, (a), and with respect to each other (b).

Furthermore, when the formation time is below the formation number, it is assumed that all the circulation, impulse, and energy supplied by the jet will end up in the leading vortex ring so that $\Gamma_c = \Gamma$, $I_c = I$, and $E_c = E$ prior to pinch-off.

The translational velocity of the vortex ring was used as the characteristic vortex ring velocity for the SG criterion; however, the local velocity anywhere within the torroidal radius will be significantly higher than this propagation velocity, with the exception of extremely thin core vortex rings. The velocity along the shear layer at the interface between the vortex ring and the driving jet flow, which is at the vortex bubble, see Figure 5.1, is most directly related to the development of instability in the shear layer; unfortunately, the exact location and velocity field of that region is very difficult to determine (and next to impossible analytically). However, at the time when the vortex ring separates, the shear layer has moved very close to the axis of symmetry; therefore, as an approximation we will define the characteristic feeding velocity as the axial velocity on the centerline produced by the jet flow (ignoring roll-up) and define the characteristic vortex ring velocity as the velocity on the centerline induced by the developing vortex ring.

For simplicity the induced velocity on the axis of symmetry at the origin of the vortex ring, $u_\star = u(0, x_c)$, (see Figure 5.1) will be used as the characteristic vortex ring velocity. The velocity profile along the axis of symmetry in the vicinity of a vortex ring can be determined from the stream function. For any axisymmetric vorticity distribution, with vorticity confined to the region A_c, the stream function is defined [42, 1],

$$\Psi(r,x) = \frac{1}{2\pi} \int_{A_c} \omega' (r_1 + r_2) [K(\lambda) - E(\lambda)] \, d\vec{x}' \, . \tag{5.9}$$

Here Ψ is the Stokes stream function evaluated at point $\vec{x} = [r, x]^T$, $\vec{x}' = [r', x']^T$ is a dummy position specifying the location of integration, ω' is the vorticity at $\vec{x}'$, K and E are the complete elliptic integrals of the first and second kind, λ is the modulus of the elliptic integrals defined $\lambda = (r_2 - r_1)/(r_2 + r_1)$, and r_2 and r_1 are distances defined $r_2 = \left[(x - x')^2 + (r + r')\right]^{1/2}$ and $r_1 = \left[(x - x')^2 + (r - r')\right]^{1/2}$. The axial velocity field can be determined from the definition of the

stream function.

$$u(r,x) \equiv \frac{1}{r}\frac{\partial \Psi}{\partial r} = \frac{1}{2\pi}\int_{A_c} \frac{\omega'}{r}\left(A+B\right) \ , \tag{5.10}$$

where,

$$A = \left[\frac{r-r'}{r_1} + \frac{r+r'}{r_2}\right]\left[K(\lambda) - E(\lambda)\right] \ ,$$
$$B = \frac{2\left(\frac{\partial K}{\partial \lambda} - \frac{\partial E}{\partial \lambda}\right)}{r_2 + r_1}\left[\frac{r_1}{r_2}\left(r+r'\right) - \frac{r_2}{r_1}\left(r-r'\right)\right] \ .$$

There is an infinite series representation of the elliptic integrals K and E which is presented in the following form by Gradshteyn and Ryzhik [29],

$$K = \frac{\pi}{2}\left\{1 + \left(\frac{1}{2}\right)^2\lambda^2 + \left(\frac{3}{8}\right)^2\lambda^4 + ... + \left[\frac{(2n-1)!!}{2^n n!}\right]^2\lambda^{2n} + ...\right\} \ , \tag{5.11a}$$

$$E = \frac{\pi}{2}\left\{1 - \frac{1}{4}\lambda^2 - \frac{3}{64}\lambda^4 - ... - \left[\frac{(2n-1)!!}{2^n n!}\right]^2\frac{\lambda^{2n}}{2n-1} - ...\right\} \ . \tag{5.11b}$$

In this equation !! represents the double factorial operator. This is a convenient expansion when analyzing behavior at the axis of symmetry because at $r = 0$, the modulus of the elliptic integrals is also zero, $\lambda = 0$, which means that the elliptic integrals evaluated at this location are, $K(0) = E(0) = \pi/2$. The form of (5.11) allows us to exactly calculate the m'th order derivative of the elliptic integrals at the axis of symmetry,

$$\left.\frac{\partial^m K}{\partial \lambda^m}\right|_{r=0} = \begin{cases} 0 & if \quad m = \text{`odd'} \\ m!\left[\frac{(m-1)!!}{2^{m/2}\frac{m}{2}!}\right]^2 & if \quad m = \text{`even'} \end{cases} \ , \tag{5.12a}$$

$$\left.\frac{\partial^m E}{\partial \lambda^m}\right|_{r=0} = \begin{cases} 0 & if \quad m = \text{`odd'} \\ \frac{m!}{m-1}\left[\frac{(m-1)!!}{2^{m/2}\frac{m}{2}!}\right]^2 & if \quad m = \text{`even'} \end{cases} \ . \tag{5.12b}$$

Therefore, the quantities A and B in (5.10) are equal to zero at the axis of symmetry which makes the fractions A/r and B/r undefined. We can use L'Hopital's rule to define the axial velocity along the axis of symmetry.

$$u(0,x) = \frac{1}{2\pi}\int_{A_c}\omega'\left(\left[\frac{\partial A}{\partial r}\right]_{r=0} + \left[\frac{\partial B}{\partial r}\right]_{r=0}\right)dx'dr' \tag{5.13}$$

The First derivative term, $\partial A/\partial r$, is equal to zero when evaluated at the axis of symmetry. Incorporating (5.12) the second derivative term can be shown to be equal to $\partial B/\partial r = \pi r'^2/r_1^3$, which means that the exact velocity profile along the axis of symmetry is,

$$u(0,x) = \frac{1}{2}\int_{A_c} \omega' \frac{r'^2}{\left[(x-x')^2 + r'^2\right]^{3/2}}\, dr'dx' \ . \tag{5.14}$$

For the point vortex (zero cross sectional area), the velocity profile becomes very simple,

$$u(0,x) = \frac{\Gamma_c}{2}\frac{l^2}{\left[(x-x_c)^2 + l^2\right]^{3/2}} \tag{5.15a}$$

and,

$$u_\star = u\left(0, x_c\right) = \frac{\Gamma_c}{2l} \ . \tag{5.15b}$$

The point vortex (and other thin core vortex rings) has a well defined torroidal radius [42, 1], $l = \sqrt{I_c/\pi\Gamma_c}$, so that an approximation for the induced velocity can be made in terms of the vortex ring circulation and impulse,

$$u_\star = \sqrt{\frac{\pi\Gamma_c^3}{4I_c}} \ . \tag{5.16}$$

It should be noted that the characteristic induced velocity, $u_\star$, is a maximum velocity along the centerline induced by the vortex ring; therefore, maintaining consistency, the characteristic feeding velocity should be defined as the maximum jet velocity on the centerline before roll-up. This feeding velocity is approximated as twice the piston velocity, $2u_p$, which is the centerline velocity of a fully developed pipe flow (Poiseuille flow).

Now the SG velocity criterion for the time when the propagation velocity surpasses the corrected jet velocity can be written,

$$U_{tr} = \left(\frac{R}{l}\right)^2 u_p \ , \tag{5.17}$$

and U_{tr} can be approximated by equation (5.8). The alternative velocity criterion proposed here of induced centerline velocity (5.16) surpassing the maximum centerline feeding velocity predicts

pinch-off at the time when,

$$\sqrt{\frac{\pi\Gamma_c^3}{4I_c}} = 2u_p \ . \tag{5.18}$$

Both criteria suggest that for a given vortex ring configuration, the pinch-off can be delayed by accelerating piston velocity for a given critical configuration.

Chapter 6

Thruster Testing Results

In order to validate the analysis and modeling presented in Chapters 2, 4, and 5 a wide variety of jet flows needed to be examined. These jet flows will be created with both tube and orifice nozzles to create parallel vs. non-parallel flows. Flows are created with expanding or contracting shear layer diameter using the variable diameter nozzle. Multiple piston velocity programs are created by switching out a cam in the mechanical plunger driving mechanism, these piston velocity programs are discussed presently.

6.1 Piston Velocity Programs

The vast majority of jet flows examined in this study have a nearly impulsive velocity program. This means that the piston velocity of the jet rapidly accelerates at the onset of flow, then maintains a nearly constant piston velocity for the remainder of pulsation. The experimental trials which utilize a nearly impulsive velocity program are summarized in table 6.1. In this table the piston velocity, u_p, normalized radial slope, $k_1^\star$, and normalized radial gradient slope, $k_2^\star$, are all average value for the entire pulsation.

The actual piston velocity programs of cases 1-6 are presented in Figure 6.1. These velocity programs were determined from the recorded motor encoder data, and this technique is validated using a particular nozzle in Appendix B. The velocity programs are shown for these cases in particular because quantities of these cases will be plotted individually in later figures. Cases 7-12 are not plotted individually, and are mainly used in the velocity profile parameterization, but

Table 6.1: Summary of experimental trials with nearly impulsive velocity programs. All values which vary with time are taken as the average over the entire pulsation.

Case	u_p	Nozzle Type	Nozzle Radius	$\frac{L}{D}$	$k_1^\star$	$k_2^\star$	Re
1	6.7	Tube	1.3 cm	2.4	0.16	1.3	3046
2	7.5	Tube	0.91	6.9	0.12	0.27	7879
3	6.8	Orifice	1.3	2.4	-0.78	4.0	6044
4	7.4	Orifice	0.93	6.8	-0.91	4.2	10491
5	5.1	Orifice	[0.96 - 1.38]	4.2	-0.8	4.2	3622
6	3.3	Orifice	[1.23 - 0.84]	4.7	-0.78	3.5	2056
7	12.8	Tube	1.3	2.5	0.17	1.1	4863
8	10.8	Tube	0.91	6.9	0.12	0.25	10178
9	12.5	Orifice	1.3	2.4	-0.81	4.1	8454
10	8.7	Orifice	1.3	2.4	-0.89	4.0	5976
11	10.4	Orifice	0.93	6.8	-0.88	3.9	11241
12	5.4	Orifice	0.93	6.8	-0.85	3.8	7205

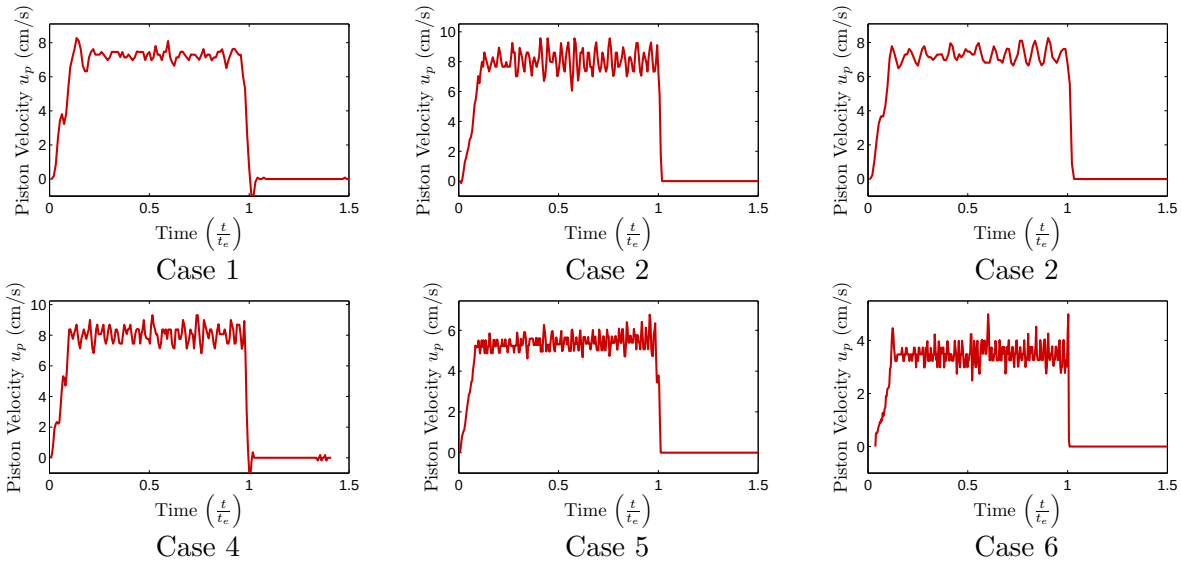

Figure 6.1: Piston velocity programs for several trials, summarized as Cases 1-6 in Table 6.1.

their velocity programs are very similar to those shown in Figure 6.1. Cases 5 and 6 use the variable diameter nozzle, Case 5 has a linearly increasing nozzle diameter, and case 6 has a linearly decreasing nozzle diameter. For both of these cases the volume flux of the prototype thruster was compensated for the expanding or contracting nozzle radius in order to maintain a nearly constant piston velocity program. For the remainder of the analysis we will consider these flows to be truly impulsive with a constant piston velocity reached at the onset of flow.

The jets with constant piston velocity are very useful while validating the control volume analysis of Chapter 2 and jet velocity parameterization in Chapter 4; however, validation of the vortex ring pinch-off model of Section 5.2 requires testing of a jet flow with an accelerating piston velocity. For this trial a jet was created with a linearly accelerating piston velocity and a constant nozzle radius of 0.98 cm (0.4 in). This velocity program is shown in Figure 6.2.

6.2 Resulting Jet Flow Parameters

Here we describe the characteristic parameters of the jet flow throughout pulsation for the various experimental trials. These parameters are required to evaluate the modeling of Chapters 2 and 4, and will be used in the model validation Section 6.3.

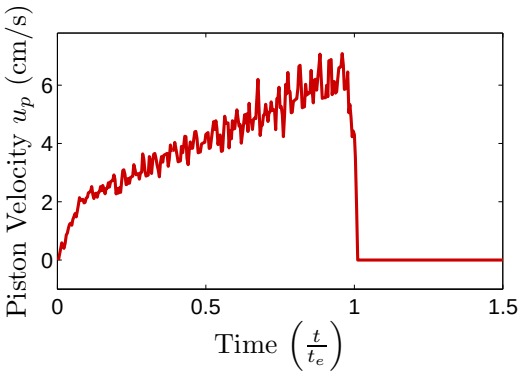

Figure 6.2: Velocity program for the accelerating jet velocity trial.

6.2.1 Volume Flux and Entrained Fluid

The volume flux, corresponding to jet flow, through any plane at some axial location, x_{V}, which is orthogonal to the axis of symmetry, can be determined from the velocity field, $d\mathrm{V}/dt = \int_0^{R_\infty} u(r, x_{\mathrm{V}}) 2\pi r dr$. The total jet volume to pass through this plane is simply, $\mathrm{V} = \int_0^{t_+} \int_0^{R_\infty} u(r, x_{\mathrm{V}}) 2\pi r dr dt$, where t_+ is some time after the entire jet has passed through the plane. For any plane downstream of the nozzle exit plane, t_+ must be greater than the time when the jet flow is terminated, t_e. We calculated the total jet volume to pass through every plane in the control volume which is presented as a function of axial distance from the nozzle in Figure 6.3. In this figure the curve for tube nozzle jets is averaged from cases 2 and 8 and the curve for the orifice nozzle jets is averaged from cases 4, 11, and 12. This figure only shows the first ≈ 5 cm (2 D) from the nozzle. It is assumed that the entire jet has passed through every plane in this region, which was qualitatively verified by the lack of flow in this region at the final time.

Also shown in Figure 6.3, is the ejected jet volume, or volume of fluid expelled from the vortex generator. It can be seen that the jets expelled from the tube nozzle entrained 8 ml of fluid right at the nozzle plane. This instantaneous entrainment of fluid can be explained by the fact that the driving flow is expelled out of a long thin cylindrical tube; which allows fluid upstream of the nozzle plane to be drawn into the low pressure roll up (see Figure 3.2). After this initial entrainment the shear tube travels downstream under its own induction velocity without entraining

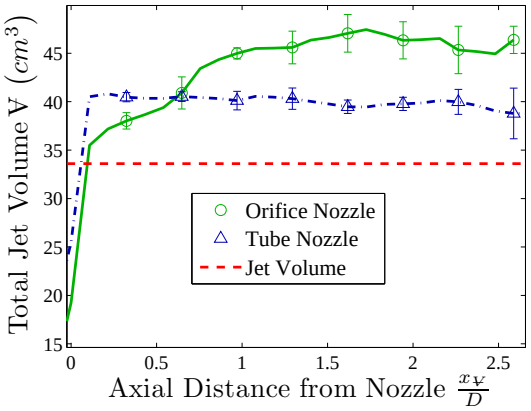

Figure 6.3: Total volume flux in the axial direction as a function of distance from the nozzle plane. Any volume flux above the jet volume (total fluid volume ejected out of the vortex generator) corresponds to entrained fluid. The tube nozzle data is averaged from cases 2 and 8 and the orifice nozzle data from cases 4, 11, and 12. For all cases the stroke ration is $L/D \approx 7$ and the errorbars indicate the standard deviation between cases.

any additional fluid, where it eventually rolls into the primary vortex ring or is left in the trailing wake. This entrainment corresponds to 25% of the jet volume expelled from the vortex generator, which is similar to entrainment fractions observed by [16] and [62]. Dabiri and Gharib measured entrainment fractions around $30-40\%$ for jets expelled with no counterflow, and Olcay and Krueger observed entrainment fractions from 20% to 45% depending on the stroke ratio, showing a large increase in entrainment fraction at very low stroke ratios ($L/D \leq 1$). The entrained volume analysis presented here is not meant to augment or verify these results, but rather show that the entrainment takes place at or around the nozzle exit plane, for tube nozzle flows, which will greatly affect the volume flux at the entrance plane, Ω_{eff}.

The fact that the orifice nozzle forms a physical barrier at the entrance plane means that there is no flow normal to the nozzle plane. Therefore, all entrained fluid must come from the radial direction, and the total jet volume to pass through the nozzle exit plane is much closer to that of the ejected jet volume, for the orifice nozzle nozzle flow. Setup limitations prevent the velocity profile from being determined exactly at the nozzle exit plane, and is instead measured a very short distance, ≈ 2 mm, downstream. This is why there is a small amount of initial entrained fluid being measured. However, this measured initial entrainment is very small and the vortex generator flow rate can be used as the volume flux at the nozzle exit plane, Ω_{eff}, without compromising accuracy. Within a short axial distance (less than a diameter) the converging jet has entrained the same volume of fluid as the parallel jet and continues to entrain fluid while contracting until reaching the vena contracta plane, at which point the converging jet has entrained 15 ml of fluid, close to 50% of the ejected jet volume.

6.2.2 Shape Factors

The shape factor model (Section 4.1.2) defines the axial velocity profile at the nozzle exit plane, in terms of the parameters Ω_{eff}, R_{eff}, a, m, and n. The volume flux was determined at the nozzle plane (as well the rest of the control volume) as was described in Section 6.2.1, which was used to define the effective mass flux, $\Omega_{\text{eff}} = d\mathcal{V}/dt|_{x=x_0}$; the remainder of the coefficients were

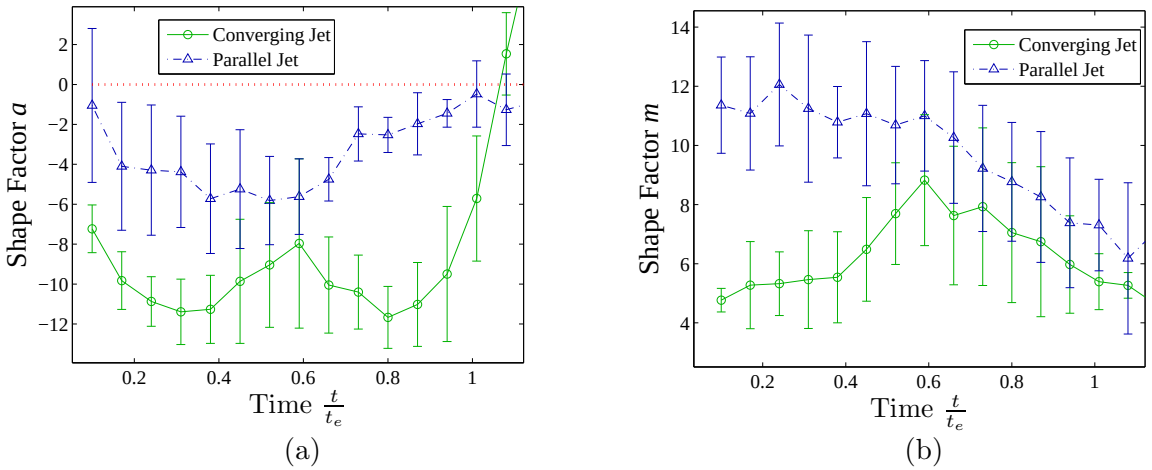

Figure 6.4: Fitted velocity profile coefficients a and m shown throughout pulsation for both parallel and non-parallel starting jets, with a nozzle radius of 1.3 cm. Each series represents the average of multiple trials, and time has been normalized by the final time at the end of pulsation. Parallel jets are averaged from cases 1 and 7 and non-parallel jets are averaged from cases 3, 9, and 10.

determined by fitting the DPIV data to the form of equation (4.2) with constraint (4.3). The fitting of the larger exponential shape factor, n, is observed to be sensitive to noise in the DPIV velocity data and fluctuates randomly. However, there is little correlation between change in n and characteristic vortex generator parameters, and a good approximation of the jet flow can be reached if this parameter is set much larger than the smaller exponential coefficient, m. The other two shape factors were averaged for multiple trials for jets ejected from both tube and orifice nozzles. Cases 1 and 7 (as summarized in Table 6.1) are averaged to give parameters of the low stroke ratio parallel jets, cases 2 and 8 are averaged for large stroke ration parallel jets, cases 3, 9, and 10 are averaged for low stroke ration converging jets, and cases 4, 11, and 12 are averaged for large stroke ratio converging jets.

Figure 6.4 shows the parameters a and m for low stroke ratio parallel and non-parallel jets. The standard deviation of the averaged experimental trials is depicted by the errorbars in the figure. A velocity profile which peaks towards the edges and drops off in the middle has a negative value for a. The value of a, determined for the converging jet, remains at a relatively constant negative value throughout pulsation demonstrating that the velocity profile has a persistent peak towards

the nozzle radius. The peak towards the edge is clearly seen in the axial velocity of the converging jet at all 3 formation times shown in Figure 4.1(b), which are sampled from case 3. The value for m also remains fairly constant throughout pulsation, indicating that the shear layer maintains a constant thickness. The parallel starting jet has a very brief period with a peak near the edges due to the influence of the forming vortex ring, but this profile quickly develops a peak on the centerline, and the value for a becomes slightly positive. The value for m starts out very high, meaning that the velocity profile is nearly uniform, but shows a slight decrease over time where development of the boundary layer on the tube nozzle increases shear layer thickness.

As would be expected the influence of the primary vortex ring during formation is marginalized over the entire pulsation for the large stroke ratio jets. The averaged shape factors a and m for both parallel and non-parallel jets with $L/D \approx 7$ is shown in Figure 6.5. Since the jet with the larger stroke ratio corresponds to a larger formation time, the boundary layer on the tube nozzle becomes more developed towards the end of pulsation. The value for m drops very low for the large stroke ratio parallel jet due to this boundary layer growth, and asymptotically approaches $m = 2$, corresponding to a fully developed pipe flow. The developed flow can clearly be seen in the axial velocity of the parallel jet in Figure 4.1(a) at the final time sample. Other than this the shape factors are very similar for the different stroke ratios.

6.2.3 Radial Velocity Profile

The normalized slopes $k_1^\star$ and $k_2^\star$ are averaged for the same cases as the shape factors. The dimensionless slope of the radial velocity, $k_1^\star$, is shown vs. time in Figure 6.6(a), for both parallel and converging jets with a low stroke ratio, $L/D \approx 2.5$. At the initiation of motion the jet flow expands outwards and both jets show a positive slope (diverging radial velocity) corresponding to the initial roll up of the leading vortex ring. As the vortex ring moves downstream, the radial velocity of the parallel jet drops to zero until the flow is terminated and the development of a stopping vortex induces a negative radial velocity profile. The slope of the radial velocity profile for the converging jet quickly reaches a negative value (converging radial velocity) which it maintains throughout the

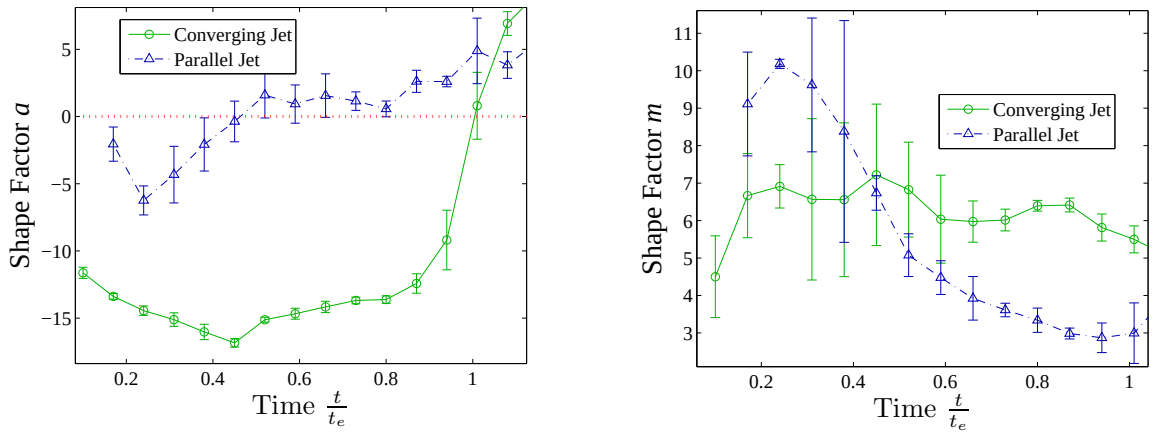

Figure 6.5: Fitted velocity profile coefficients a and m shown throughout pulsation for both parallel and non-parallel starting jets with large stroke ratio. Each series represents the average of multiple trials, and time has been normalized by the final time at the end of pulsation. Parallel jets are averaged from cases 2 and 8 and non-parallel jets are averaged from cases 4, 11, and 12.

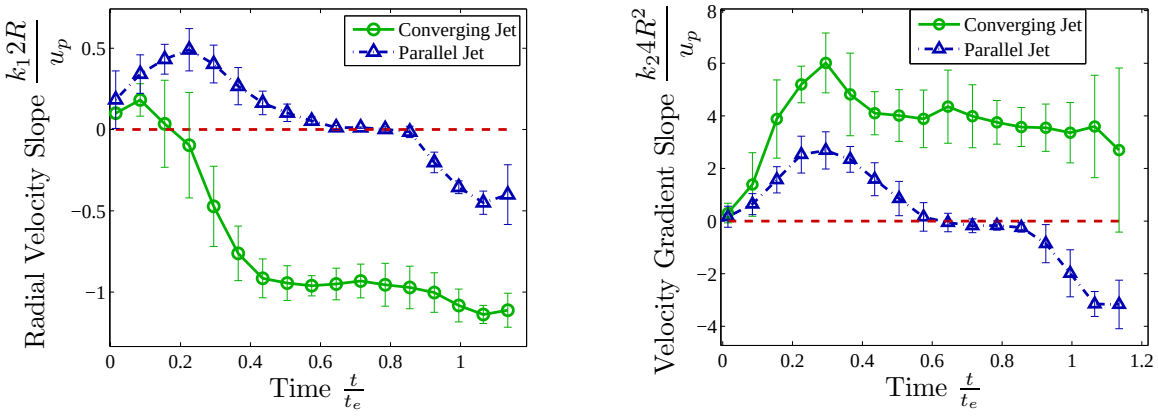

Figure 6.6: The dimensionless slope of the (a) radial velocity profile, $k_1^\star$ and (b) gradient of the radial velocity profile, $k_2^\star$, for jets with a stroke ratio of $L/D \approx 2.5$, expelled through both tube and orifice nozzles. Parallel jets are averaged from cases 1 and 7 and non-parallel jets are averaged from cases 3, 9, and 10.

rest of the pulsation. Figure 6.6(b) shows the dimensionless slope of the gradient of the radial velocity in the axial direction, $k_2^\star$. Again the parallel jet radial velocity is due to the roll-up of the leading vortex ring and stopping vortex ring with nearly zero slope in between. The slope of the converging jet radial velocity gradient is larger and persists throughout pulsation as would be expected, but here the primary vortex ring has a more significant presence increasing the slope of $\partial v/\partial x$ in the initial formation period.

The dimensionless slopes $k_1^\star$ and $k_2^\star$ are shown in Figure 6.7 for the jets with a large stroke ratio. The converging jet shows the same behavior as the low stroke ratio trials, but the influence of the primary vortex ring is much less noticeable and can be considered negligible. It should be noted here that k_1 and k_2 actually vary significantly between different trials not just because of the different piston velocities, but also because the ratio of nozzle diameter to inner cavity diameter varies between trials and this will also change the radial velocity independently of piston velocity. Fortunately the normalization employed to scale these slopes results in a convergence of $k_1^\star$ and $k_2^\star$, not just for trials with different piston velocities, but also for the different nozzle diameters.

The slope of the radial velocity and velocity gradient of the parallel jet also display the same behavior as the low stroke ratio trials but as would be expected the jet spends a longer period of time with no induced radial velocity. Additionally the radial velocity gradient of the parallel jets has a negative value for a very short period of time, due to the rapid acceleration of fluid during vortex ring formation. This phenomenon was not observed for the low stroke ratio case because the acceleration of piston velocity occurred before any significant vortex ring formation.

Here it is interesting to note that nearly the entire jet will end up in the primary vortex ring for the parallel jet with low stroke ratio (cases 1 and 7). Despite the lack of separation between the vortex ring and the trailing shear flow, Figures 6.6 and 6.7 shows that there is a clear point where the primary vortex no longer induces any appreciable radial velocity at the nozzle exit plane, which is at a formation time of, $t^\star \approx 1.2$, which is well before the vortex ring separates from the shear flow.

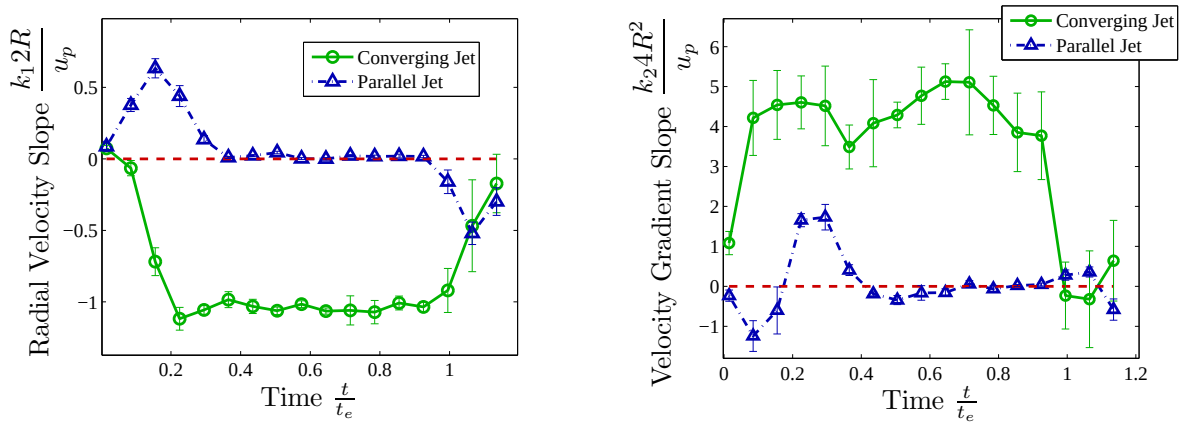

(a) $k_1^\star$ (b) $k_2^\star$

Figure 6.7: The dimensionless slope of (a) radial velocity profile, $k_1^\star$ and (b) gradient of the radial velocity profile, $k_2^\star$, for jets with a stroke ratio of $L/D \approx 7$, expelled through both tube and orifice nozzles. Parallel jets are averaged from cases 2 and 8 and non-parallel jets are averaged from cases 4, 11, and 12.

6.3 Validation of Starting Jet Model

The circulation, hydrodynamic impulse, and kinetic energy of the control volume are calculated according to the 1D slug model, equation (4.1) and the shape factor model, equation (4.4) both with and without contributions from the radial velocity terms, equation (4.6) for all experimental cases, using the parameters $k_1^\star$, $k_2^\star$, a, and m identified for these cases in the previous section. The actual circulation, impulse, and kinetic energy of the total jet was determined from the DPIV analysis (Section 3.4). The accuracy of all 3 models is presented here for the different nozzles and stroke ratios.

6.3.1 Circulation

Figure 6.8 shows the evolution of circulation for both parallel and converging starting jets with a stroke ratio of $L/D \approx 2.5$ and piston velocity of $\approx$7 cm s^{-1} (cases 1 and 3). It can be seen from this figure that the total circulation of the jet is well predicted by the shape factor model with contributions from the radial velocity included, for both nozzle configurations.

The circulation of the parallel jet (case 1) is fairly closely approximated by all three models, with the 1D slug model predicting the lowest circulation at the final time when the jet flow is terminated. The maximum circulation reached by the jet is 34% larger than the 1D slug model prediction. The rate of circulation added to the system is dependent on the centerline axial velocity and not the piston velocity; therefore, a parabolic velocity profile will have a greater flux of circulation for the same piston velocity. The shape factor model accurately captures the parabolic axial profile, but still under-predicts the final circulation. Despite the parallel flow in the cylinder, the development of the primary vortex ring induces a small radial velocity in the jet flow crossing the nozzle exit plane, as was mentioned in previous sections. Including contributions from non-zero radial velocity brings the predicted circulation very close to the final jet circulation.

The total circulation of the converging jet (case 3) just after pulsation is significantly higher than the circulation predicted by the 1D slug model and the shape factor model. In this config-

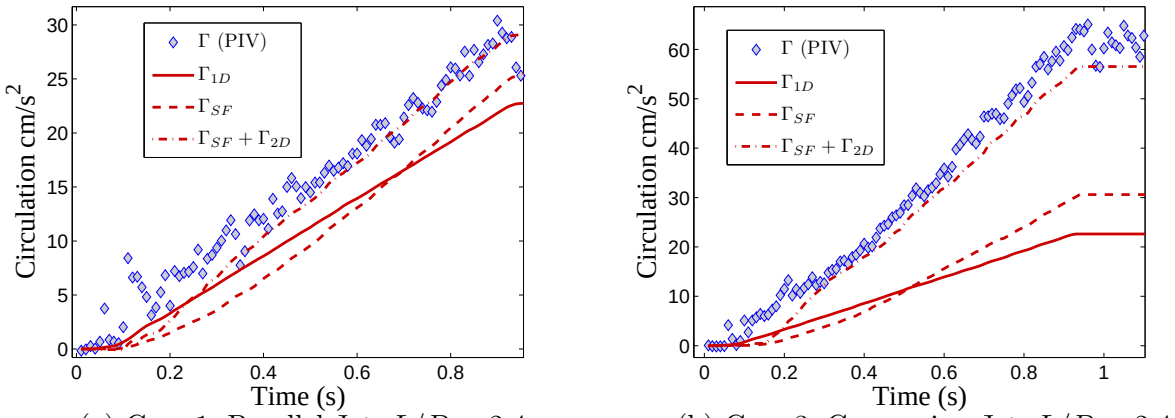

(a) Case 1, Parallel Jet, $L/D = 2.4$ (b) Case 3, Converging Jet, $L/D = 2.4$

Figure 6.8: Evolution of circulation for a (a) parallel jet and (b) converging jet, with a stroke ratio of, $L/D = 2.4$ and a jet velocity of ≈ 7cm s^{-1}.

uration the centerline velocity still experiences a slight increase, which causes the shape factor to predict a higher circulation than the 1D slug model, but the effect of the converging radial velocity at the entrance boundary is much more apparent. Including the contribution from the radial terms nearly doubles the predicted circulation, and brings the prediction very close to the actual circulation of the jet. This radial velocity component causes the total circulation of the converging jet to be double the total circulation of the parallel jet, 103% larger, for the same piston velocity and a low stroke ratio, $L/D = 2.4$.

The circulation of both parallel and converging jets with a larger stroke ratio, $L/D \approx 7$ (cases 2 and 4), is shown in Figure 6.9, and again the shape factor model, with contributions from the radial velocity component included, provides a good predictor of total circulation for both parallel and converging jets. Here the longer formation time and more developed axial velocity profile of the parallel jet (case 2) produces a large increase in circulation; as is shown by the larger circulation predicted by the shape factor model compared the 1D slug model. Whereas the effect of the radial velocity component, which exists for a short period of time during initial ring formation, only increases the predicted circulation by a negligible amount. The converging jet (case 4) experiences less development in the axial velocity profile due to boundary layer growth and the shape factor model for this case predicts a similar increase over the 1D slug model as the low stroke ratio case

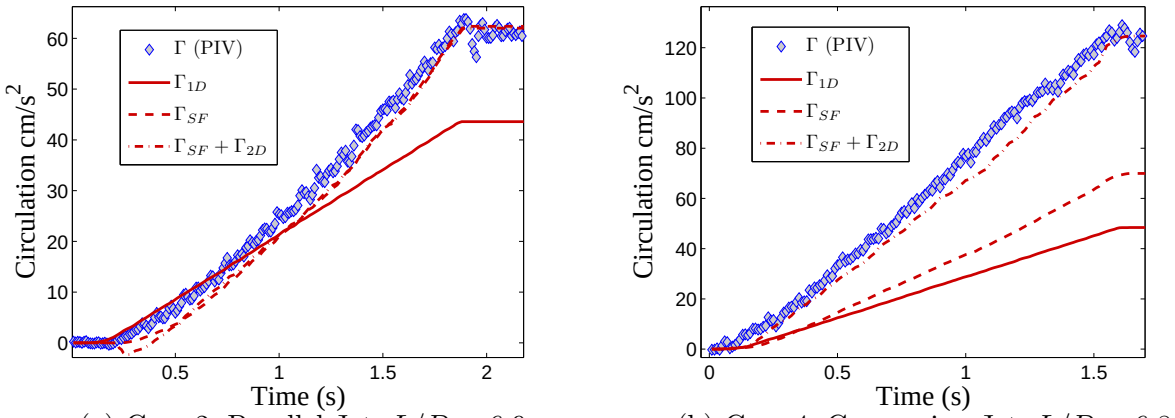

(a) Case 2, Parallel Jet, $L/D = 6.9$ (b) Case 4, Converging Jet, $L/D = 6.8$

Figure 6.9: Evolution of circulation for a (a) parallel jet and (b) converging jet, with a stroke ratio of, $L/D \approx 7$ and a jet velocity of ≈ 7cm s^{-1}.

(case 3). The persistent radial velocity profile again nearly doubles the total jet circulation which is captured by the 2D model contributions. In total the converging jet produces 94% more circulation than the parallel jet with a stroke ratio $L/D \approx 7$

6.3.2 Impulse

The impulse is fairly insensitive to the parameter, m, when $a \approx 0$, which means that any deviation of the shape factor model from the 1D slug model for parallel jets is mostly due to the change in the effective mass flux, Ω_{eff}, and effective radius, R_{eff}, which are in part due to entrainment of fluid at the entrance boundary. Interestingly the initial entrained fluid increases the effective mass flux for the parallel jet, but it also increases the effective radius, sometimes to the point where there is a slight decrease in effective piston velocity. This effect results in a total jet impulse which is lower than that predicted by the 1D slug model as can be seen in Figure 6.10, which shows the total impulse of both parallel and converging jets with a stroke ratio $L/D = 2.4$ (cases 1 and 3). This fairly minimal decrease in impulse of the parallel jet is captured by the shape factor model, and the contribution from the radial velocity terms is negligible for this case. Krueger and Gharib [40] measured the total impulse imparted by expelling a parallel jet with a stroke ratio of $L/D = 2$, to be 40% larger than the 'momentum impulse' (see equation 2.12) for certain velocity programs.

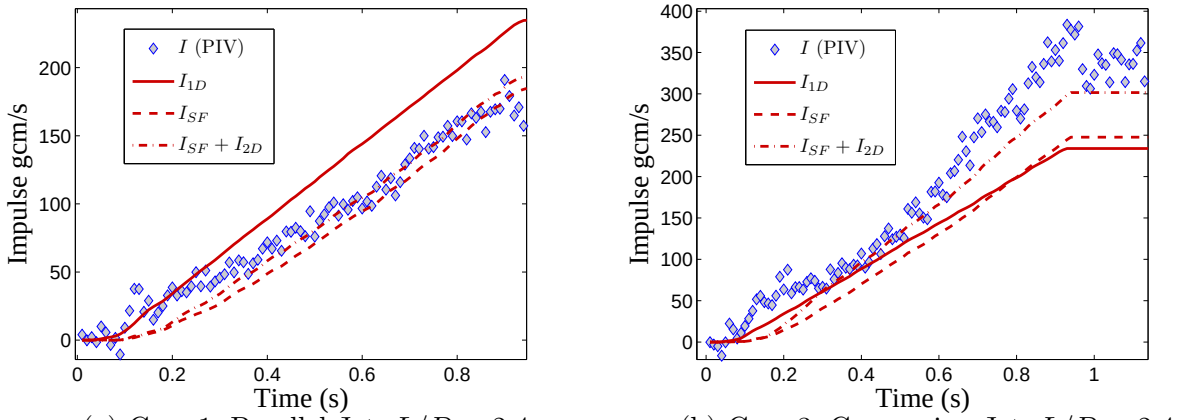

(a) Case 1, Parallel Jet, $L/D = 2.4$ (b) Case 3, Converging Jet, $L/D = 2.4$

Figure 6.10: Evolution of impulse for a (a) parallel jet and (b) converging jet, with a stroke ratio of, $L/D = 2.4$ and a jet velocity of ≈ 7cm s^{-1}.

The discrepancy between those results and impulse measured for parallel jets in this investigation could result from a number of differences in the experimental setup. The velocity program used here has a very fast acceleration then levels off and remains at a constant value for the rest of the pulsation, as opposed to the velocity programs of Krueger and Gharib which are more triangular than trapezoidal. This might cause the vortex ring to grow close to the nozzle exit for a longer period of time and induce a more significant radial velocity on the starting jet, especially since the slope of the radial velocity gradient, $k_2^\star$, was observed in Figure 6.7 to be sensitive to the acceleration during the vortex ring formation stages. Additionally, the jets of Krueger and Gharib have a Reynolds number on the order of 20000, whereas the parallel jet of Figure 6.10a (case 1) has a Reynolds number of 3046, and the thinning of the shear layer associated with increased Reynolds number likely helps keep the effective radius small.

The total impulse of the low stroke ratio converging jet (case 3) is 35% larger than the impulse predicted by the 1D slug model. The shape factor model prediction shows that the converging jet impulse experiences an increase due to the peak of the axial velocity towards the edge of the nozzle, but the jet impulse is mostly affected by the radial velocity, and again the increase is accurately captured by the 2D model contributions. Overall the converging jet impulse is 73% higher than the parallel jet for the same piston velocity with stroke ratio $L/D = 2.4$.

Figure 6.11 shows the hydrodynamic impulse of both parallel and converging jets with a stroke ratio $L/D \approx 7$ (cases 2 and 4). The impulse of the parallel jet is actually fairly well predicted by the 1D slug model, but the shape factor model slightly over-predicts the total impulse for this case. This overshoot can be attributed to the difficulty in capturing the velocity directly on the nozzle exit plane, compounded by an inadequacy of the jet velocity parameterization. For this particular case even a very short distance from the nozzle the forming vortex ring induces a substantial upstream flux, just outside the nozzle radius area. The generalized velocity model, equations (4.2 and 4.3), were intended to approximate the jet velocity profile right at the nozzle exit boundary using a limited number of parameters. As a result any negative flux outside of the nozzle radius is not captured in the model. While there is no limitation in extending the jet velocity model to capture profiles which are more typical further downstream, this would introduce at least two more model parameters drastically increasing the complexity of the model; hence that is not pursued in this investigation. Since the generalized jet velocity model cannot capture negative velocity, and therefore cannot capture the negative flux during formation, the shape factor model will predict impulse slightly above the actual jet impulse when the entrance boundary is chosen just downstream of the nozzle exit plane. However, the shape factor model will accurately predict the circulation for the same case since it still properly captures the centerline velocity (as can be seen in Figure 6.9). The effect of the radial velocity induced by the formation of the primary vortex ring is almost non-existent for the parallel jet with a large stroke ratio (case 2).

The velocity profile of the converging jet is much more consistent throughout pulsation even for the large stroke jet (case 4), so that the effect of axial velocity shape as well as the effect of radial velocity on total impulse is very similar between the converging jets with a low stroke ratio and those with a high stroke ratio. Again the total jet impulse is well predicted by the shape factor model, with contributions from the radial velocity terms included. In total the converging jet has 75% more impulse than the parallel jet with the same piston velocity and stroke ratio, $L/D \approx 7$. Again the impulse measured for the parallel jet does not acquire the 'pressure impulse' reported by [40] for a stroke ratio $L/D = 8$; however, it should be noted that at such large stroke

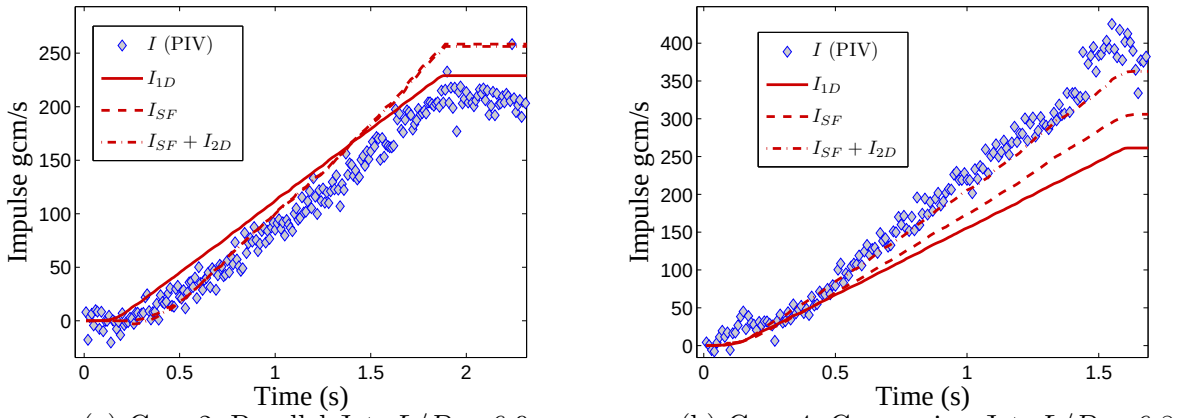

(a) Case 2, Parallel Jet, $L/D = 6.9$ (b) Case 4, Converging Jet, $L/D = 6.8$

Figure 6.11: Evolution of impulse for a (a) parallel jet and (b) converging jet, with a stroke ratio of, $L/D \approx 7$ and a jet velocity of ≈ 7cm s^{-1}.

ratios the additional thrust attributed to 'nozzle overpressure' is greatly diminished because of the marginalized influence of the initial vortex ring formation.

6.3.3 Kinetic Energy and Nozzle Pressure

The kinetic energy of the jets were determined using the DPIV algorithms and recorded over time. Unfortunately, there is no direct pressure measurement at the nozzle exit plane, so the accuracy of nozzle pressure calculation is difficult to determine. However, the energy model requires the knowledge of the pressure at the nozzle (pressure work done at the boundary), so that validation of the kinetic energy model indirectly validates the pressure model as well. Even though the pressure distribution was not measured experimentally, it was calculated at the nozzle exit plane from the jet velocity profile according to equation (2.25). The pressure profile is shown with respect to radius in Figure 6.12, for parallel and non-parallel jets with $L/D = 2.4$ (cases 1 and 3). It can be seen in this figure that the initial stages of vortex ring formation induce overpressure (pressure above stagnation pressure) within the nozzle exit area and under-pressure just outside the nozzle radius, for the parallel jet (case 1). The overpressure on the orifice nozzle is very minimal at the start of motion. After this formation period the converging jet maintains overpressure at the nozzle exit area but the parallel jet drops to stagnation pressure.

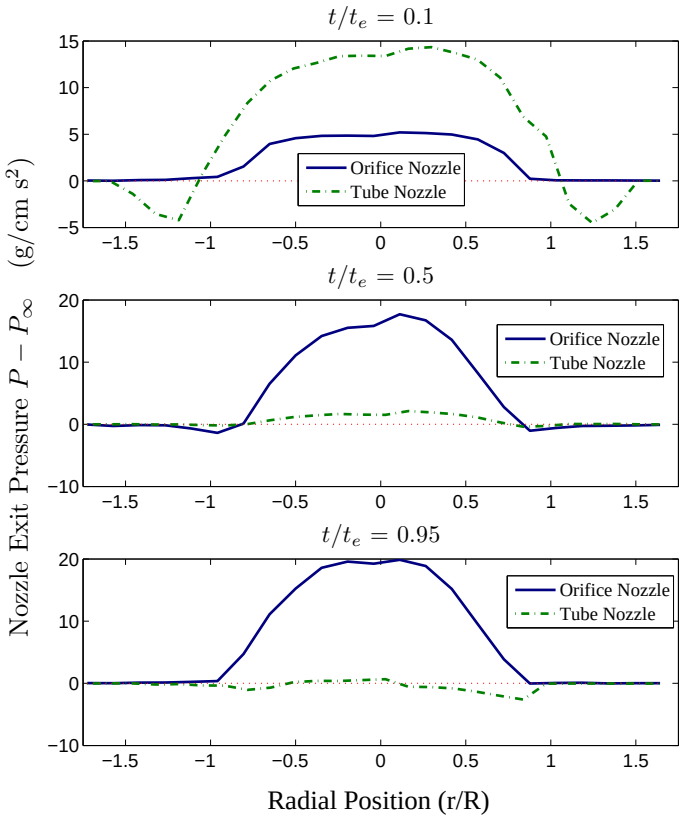

Figure 6.12: Pressure distribution is shown over the nozzle exit area for both tube and orifice nozzles. Both cases are shown for low stroke ratio jets with a piston velocity of ≈ 7 cm s^{-1} (cases 1 and 3).

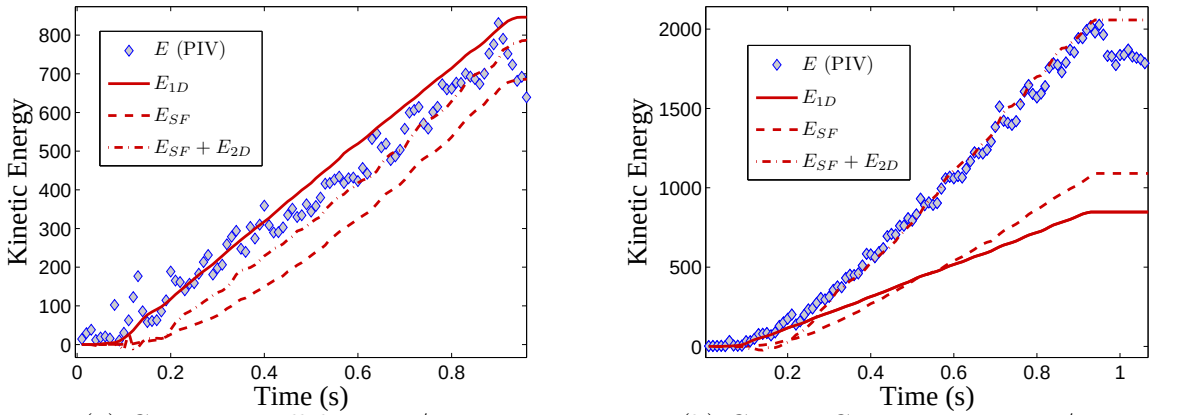

(a) Case 1, Parallel Jet, $L/D = 2.4$ (b) Case 3, Converging Jet, $L/D = 2.4$

Figure 6.13: Kinetic energy of a jet created with a piston velocity of ≈ 7 cm s^{-1} and stroke ratio of $L/D = 2.4$. (a) parallel jet and (b) converging jet.

The kinetic energy of both parallel and converging starting jets, expelled with equivalent piston velocities $u_p \approx 7$ cm s^{-1} and low stroke ratio $L/D = 2.4$ (cases 1 and 3) are shown in Figure 6.13. The converging jet has a much larger kinetic energy than the 1D slug model prediction. Some of the additional energy is due to the peak in axial velocity towards the nozzle edge, which is captured by the shape factor model prediction; however, a much larger portion of the increased energy is due to the increased pressure along the nozzle plane required to support the radial velocity gradient. The shape factor model with contributions from the radial velocity provides a very close approximation to the actual kinetic energy of the jet. Overall the converging jet has a kinetic energy more than double (135%) the parallel jet. The parallel jet's energy is fairly well approximated by all three models, all coming within 15% of the final jet energy. But the shape factor model with contributions from the radial velocity terms provides the best approximation.

For the jets with a large stroke ratio, $L/D \approx 7$ (cases 2 and 4), again all three models provide a decent approximation of the parallel jet energy, as can be seen in Figure 6.14. The converging jet has a much larger kinetic energy than the 1D slug model prediction. The shape factor model prediction shows that the peak in axial velocity plays a role in increasing the total jet energy, but the added pressure associated with radial velocity gradient still has a more significant effect. Again the shape factor model with radial components included accurately predicts kinetic energy of the

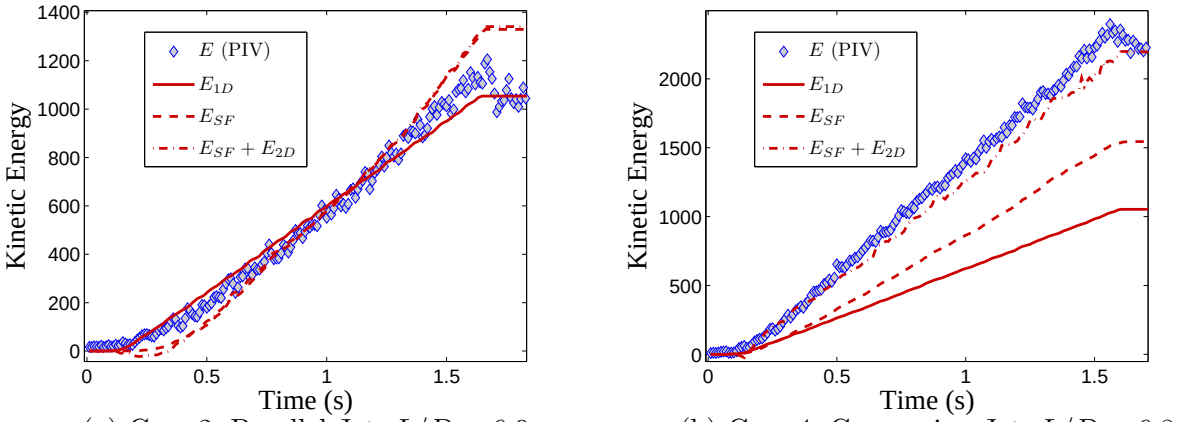

(a) Case 2, Parallel Jet, $L/D = 6.9$ (b) Case 4, Converging Jet, $L/D = 6.8$

Figure 6.14: Kinetic energy of a jet created with a piston velocity of ≈ 7 cm s^{-1} and stroke ratio of $L/D \approx 7$. (a) parallel jet and (b) converging jet. Total energy is marked by a gray diamond.

converging jet. Overall the converging jet contains 105% more kinetic energy than the parallel jet, for $L/D \approx 7$.

6.4 Validation of Characteristic Vortex Ring Velocities

The formation number modeling in Chapter 5 relies on the approximation of multiple velocities associated with a translating vortex ring. This section addresses the accuracy of those approximations.

6.4.1 Vortex Ring Translational Velocity

Lord Kelvin stated that the motion of a vortex system will minimize the energy Hamiltonian of the system, under area preserving iso-vortical perturbations [32, 33]; this equates the translational velocity, a Lagrange multiplier of impulse in the energy Hamiltonian, to the ratio $U_{tr} = \frac{\delta E}{\delta I}$. Using the 1D slug model approximation and equating the vortex system to the Norbury family of vortex rings, Mohseni [55, 53] derived the translational velocity in terms of piston velocity. This analysis showed that the translational velocity will be approximately half the piston velocity, $U_{tr} \approx \frac{1}{2}u_p$. This relationship has been well documented for parallel starting jets; however, the 1D slug model is demonstrated to be a poor prediction of non-parallel starting jets so the relationship between

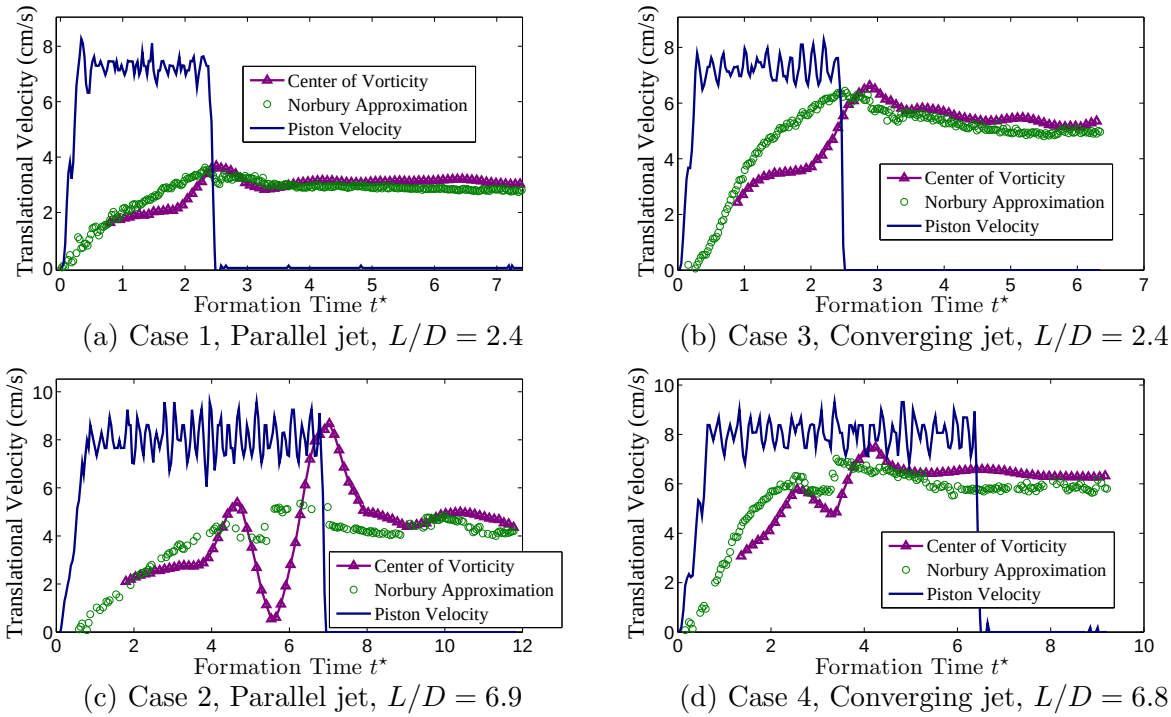

(a) Case 1, Parallel jet, $L/D = 2.4$

(b) Case 3, Converging jet, $L/D = 2.4$

(c) Case 2, Parallel jet, $L/D = 6.9$

(d) Case 4, Converging jet, $L/D = 6.8$

Figure 6.15: Vortex ring translational velocity and piston velocity vs. formation time, $t^\star$, for case 1 (a), case 3 (b), case 2 (c), and case 4 (d).

piston and ring velocity is likely very different.

Equation (5.8) gives an approximation for the translational velocity of a steady vortex ring in the Norbury family with specified circulation, impulse, and energy. The actual translational velocity of several vortex rings was determined from the motion of the center of vorticity of the leading vortex ring given by the DPIV analysis. The measured translational velocity is shown in Figure 6.15, as well as the translational velocity as predicted by equation (5.8) using circulation, impulse, and energy of the primary vortex ring measured from DPIV data, equation (3.2). Figure 6.15 also shows the piston velocity over the same time period as a reference velocity.

Figures 6.15a and 6.15b (corresponding to cases 1 and 3) show that when the jets are ejected with a low stroke ratio equation (5.8) provides an excellent prediction of translational velocity, after the formation dynamics have subsided and the ring settles upon a stable configuration. However, during the period of substantial vortex ring growth, the actual vortex ring translational velocity is substantially less than the predicted velocity. The jets expelled with a higher stroke ratio, Figures 6.15c and 6.15d (corresponding to cases 2 and 4), experience a much more energetic/dynamic pinch-off which results in large oscillations in both U_{tr} and l as the primary vortex ring settles upon a stable configuration, due to the interaction of the leading vortex ring with the trailing jet. Eventually these vortex rings stabilize and translational velocity closely approaches the predicted velocity of (5.8), but the vortex ring does not acquire a stable configuration until well after pinch-off, when there is a large enough distance between the leading vortex ring and the trailing jet. This demonstrates that the propagation velocity is very sensitive to the formation dynamics.

It can also be seen that despite the nearly identical piston velocities ($\approx$7 cm/s for all cases) the vortex ring formed from the converging jet has a significantly larger translational velocity. After settling on a stable configuration, the vortex rings crated from parallel jets have an average translational velocity which is close to half the piston velocity, 48% for low stroke ratio (case 1) and 54% for large stroke ratio (case 2). Whereas the converging jet vortex rings have average translational velocities which are 74% of the piston velocity for low stroke ratio (case 3) and 73% of the piston velocity for large stroke ratio (case 4). This could help explain a large variation in

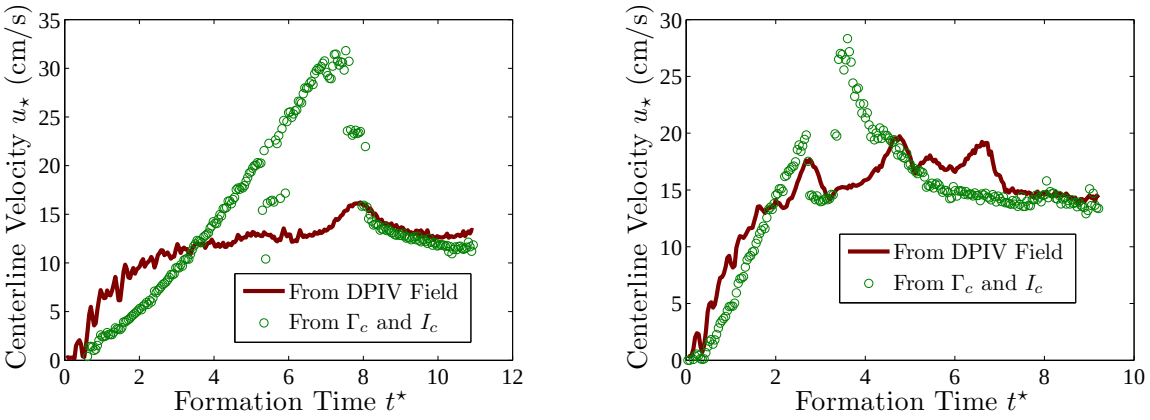

(a) Case 2, Parallel Jet, $L/D = 6.9$ (b) Case 4, Converging Jet, $L/D = 6.8$

Figure 6.16: Centerline velocity of the vortex ring, $u_\star$, vs. formation time $t^\star$. Actual values calculated from PIV velocity data along axis of symmetry, predicted values calculated from equation (5.16).

reported vortex ring translational velocities with the same piston velocity.

6.4.2 Vortex Ring Centerline Velocity

This study uses the centerline velocity of the vortex ring, $u_\star = u(0, x_c)$, as the characteristic induced velocity to define a kinematic pinch-off criterion. The simplest approximation of this velocity is the centerline velocity of an equivalent point vortex ring (identical circulation) whose velocity is defined in (5.16). Figure 6.16 shows the actual centerline velocity of vortex rings created from both converging and parallel jet flows (cases 2 and 4), and the approximated centerline velocity is calculated from (5.16) using values for ring circulation and impulse determined from (3.2). For both cases the stroke ratio is large $L/D \approx 7$, which corresponds to a more energetic pinch-off process resulting in large oscillations in the translational velocity of the vortex ring. It can be seen in Figure 6.16 that the centerline velocity of the vortex ring is reasonably well approximated by the point vortex approximation (5.16).

6.5 Validation of Pinch-Off Criterion

Now that the velocity approximations have been validated we will examine the exact formation number of different starting jet flows, and the validity of the different pinch-off criteria. Starting with the the most simple flow having constant piston velocity, u_p, and static nozzle ($R =$ constant). A converging radial velocity significantly decreases the jet formation number, and this is accurately captured by the centerline velocity criterion used in this paper. Next the formation number is measured for jets with expanding and contracting nozzle radius programs, showing little change from the constant diameter orifice nozzle. Finally, an accelerating piston velocity program is investigated exhibiting a vastly increased formation number over the constant piston velocity jet with the same nozzle configuration. The new pinch-off criterion is observed to be valid for both variable nozzle radius programs and accelerating piston velocity programs.

6.5.1 Constant u_p Constant R

From a qualitative standpoint, the much larger induced/translational velocity of the converging jet should cause a decrease in formation number if the kinematic pinch-off criterion truly corresponds to the vortex ring separation mechanism.

The formation number can be predicted from (5.18) if the circulation and impulse of the forming vortex ring are known. If we assume that the piston velocity is constant, and that, up until pinch-off, the circulation and impulse of the vortex ring are equal to the total jet circulation and impulse, then those quantities can be approximated by the product of the rates given in (4.1) and (4.6) and the total pulsation time, t_e. Substituting these circulation and impulse approximations into (5.18) and recognizing that the stroke length is equal to, $L = u_p t_e$, for constant piston velocity, allows the formation number to be calculated as,

$$t_p^\star = \left.\frac{L}{D}\right|_{2u_p=u_\star} = \left[\frac{128\left(16 + k_2^\star - k_1^{\star 2}\right)}{\left(4 + k_2^\star\right)^3}\right]^{1/2} . \tag{6.1}$$

Using the values of $k_1^\star$ and $k_2^\star$ from table 6.1, equation (6.1) predicts a formation number of 4.1 for parallel jets (case 1 specifically) and 2.1 for converging jets. Both of these formation numbers will

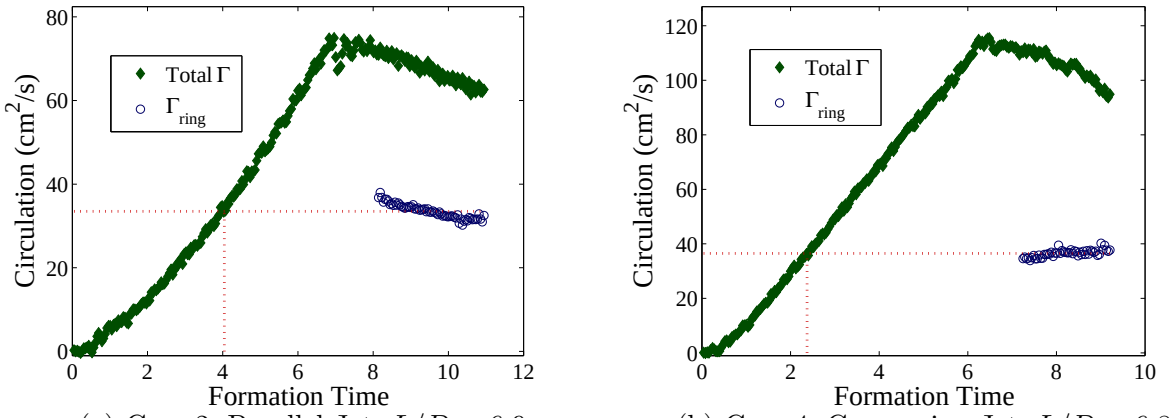

(a) Case 2, Parallel Jet, $L/D = 6.9$ (b) Case 4, Converging Jet, $L/D = 6.8$

Figure 6.17: Circulation vs. Formation time of the entire jet and the leading vortex ring for both parallel and non-parallel jets.

be shown to be reasonable predictions of the actual formation number of parallel and converging jets, respectively.

The circulation for a converging starting jet (case 4) is plotted with respect to formation time in Figure 6.17(b) next to the circulation for a parallel starting jet (case 2) in Figure 6.17(a). The vortex core boundary was identified as described in 3.4. The circulation integrated over this region, after the primary vortex ring had settled, is also shown for both jet flows. Some time after the jet flow has been terminated the total circulation drops accounting for vorticity cancellation at the axis of symmetry. This decay is typical of thick vortex rings and has been reported in [57], also the fluid from the shear layer which rolls into the leading vortex ring just before separation is compressed towards the axis of symmetry, as was described in Section 5.2 (Figure 5.2), adding to the vorticity cancellation. In addition to the cancellation of vorticity, the large trailing wake becomes unstable with time which can result in bifurcation/blooming of forming vortex rings in the wake, making the flow asymmetric about the centerline and driving the vortex rings in the wake out of the illuminated cross section. See [72] for a description of blooming jets.

Figure 6.17 demonstrates that vortex rings formed from converging starting jets pinch-off at a significantly lower formation time. It can be seen that the formation number for the parallel jet is ≈ 4 as would be expected, but the formation number for the converging jet drops to ≈ 2.3, which

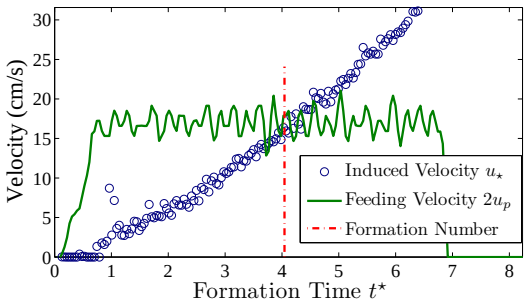

(a) Case 2, Parallel Jet, $L/D = 6.9$

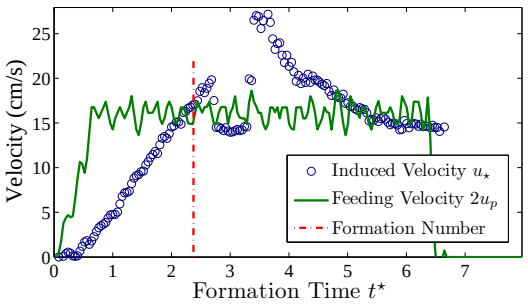

(b) Case 4, Converging Jet, $L/D = 6.8$

Figure 6.18: Induced and feeding velocity vs. formation time for a jets created with tube and orifice nozzles. Formation number for these cases is also shown.

is very close to the formation number predicted by our pinch-off criterion under the assumption of constant piston velocity (6.1). Figure 6.18 shows the induced velocity, defined by (5.16), as well as the feeding velocity, $2u_p$, for the two jet flows represented in Figure 6.17 (cases 2 and 4). It can be seen here that the induced velocity surpasses the feeding velocity almost exactly at the formation number for both types of jet flows, affirming the use of the centerline kinematic criterion for predicting pinch-off in both parallel and non-parallel starting jets.

Figure 6.19 shows the vortex ring translational velocity, U_{tr}, determined from the motion of the vortex centroid, as a function of formation time as well as the adjusted jet velocity in accordance with the SG criterion. To determine the adjusted jet velocity the vortex ring radius was calculated from DPIV data according to equation (3.3). This criterion predicts pinch-off at a later formation time than observed, mostly because the axial velocity at the jet/ring interface is substantially larger than the propagation velocity. Furthermore, the large fluctuations in both translational velocity and torroidal radius (used to determine adjusted jet velocity) result in some ambiguity of predicted formation number, for the converging jet, since when the translational velocity approaches the adjusted velocity it drops briefly before surpassing the adjusted jet velocity well after pinch-off.

However, it is not exactly clear that the shift in formation number associated with a converging radial velocity is due to a change in the final vortex ring configuration. The drop in formation number seen in starting jet simulations with fully developed pipe flow at the entrance boundary (see [78]) is closely related to the definition of formation time. As was pointed out by Rosenfeld

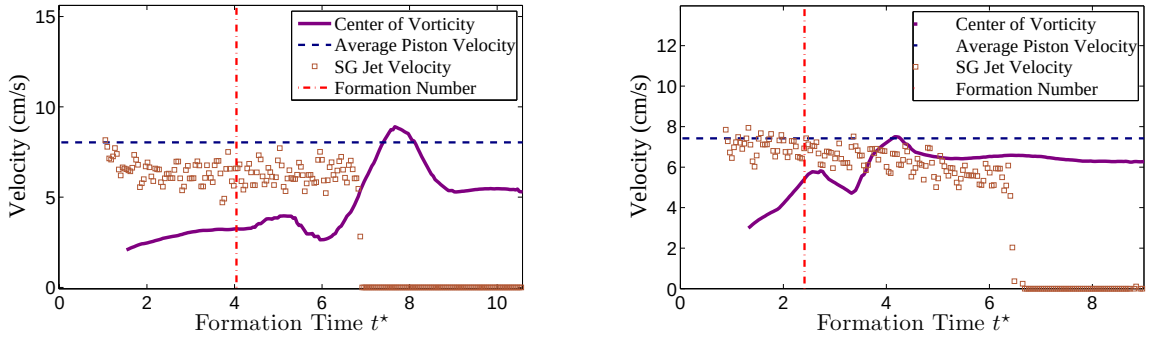

(a) Case 2, Parallel Jet, $L/D = 6.9$ (b) Case 4, Converging Jet, $L/D = 6.8$

Figure 6.19: Propogation and adjusted jet velocity vs. formation time for a jets created with tube and orifice nozzles.

et. al. the rate of circulation flux across the entrance plane for parallel starting flows is exactly proportional to the centerline velocity, $d\Gamma/dt = \frac{1}{2}u_0^2$, independent of the jet velocity profile. However, the formation time is scaled by the piston velocity, which is much less than the centerline velocity for parabolic jet velocity profiles; meaning that flows with a parabolic velocity profile will produce a higher vorticity flux for the same volume flux compared to flows with a uniform velocity profile. Similarly converging starting jets generate a significantly larger vorticity flux than the parallel starting jet with the same piston velocity, as was just shown in Section 6.3. As would be expected these flows have a formation number, much lower than the trend seen in [23]. Therefore, we calculated the mean core radius of the vortex ring, as well as the hypothetical mean core radius of the total jet, by taking the non-dimensional energy and interpolating mean core radius from the data given in [60]. The mean core radius of vortex rings generated from parallel and converging starting jets (cases 2 and 4) are shown in Figure 6.20. The mean core radius of the parallel jet vortex ring settles to about $\epsilon = 0.57$, which is very similar to values found in [23] for parallel jets. The mean core radius of the converging jet vortex ring is a bit lower $\epsilon = 0.47$, corresponding to a 'thinner' vortex ring with larger dimensionless energy, α. This means that the centerline velocity criterion accurately predicts pinch-off without requiring a specified final ring configuration.

Next we extend our analysis to include more complicated jetting programs, starting with an accelerating piston velocity program, while still using a static nozzle.

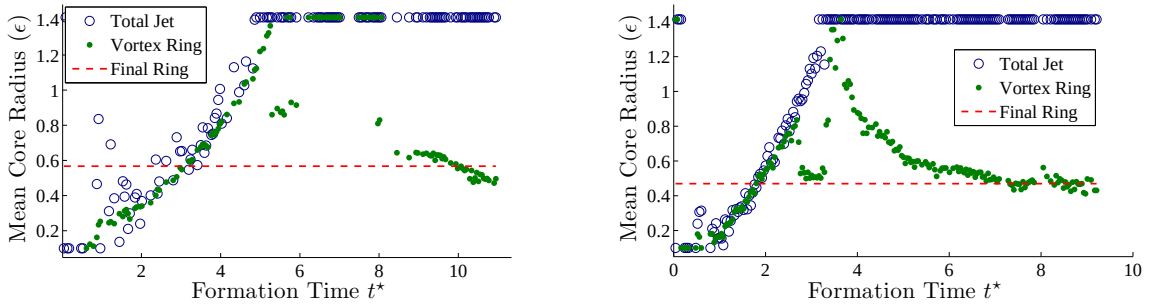

(a) Case 2, Parallel Jet, $L/D = 6.9$ (b) Case 4, Converging Jet, $L/D = 6.8$

Figure 6.20: Mean core radius, ϵ, vs. formation time of the total jet and leading vortex ring for parallel and converging jets.

6.5.2 Accelerating u_p Constant R

It was hypothesized earlier that the formation number could be increased for a given vortex ring configuration by accelerating the jet flow to compensate for the quickly accelerating induced velocity. To investigate this, the vortex generator was driven with a linearly increasing piston velocity. Figure 6.21 shows the total jet circulation as well as the circulation of the primary vortex ring for an accelerating jet expelled through an orifice nozzle. The piston velocity program was depicted earlier in Figure 6.2 for this trial. It can be seen that the formation number of this flow is approximately 4, which is a drastic increase over the formation number of the jets expelled through the same nozzle with constant piston velocity.

Figure 6.22 shows that the centerline velocity criterion still coincides with the jet formation number even for jets with accelerating piston velocity. The mean core radius of the vortex ring is shown in Figure 6.23, which shows that after pinch-off the vortex ring settles on a configuration with mean core radius $\epsilon = 0.66$, which means that jets with accelerating piston velocity are able to create significantly 'thicker' vortex rings than any jet expelled with a constant piston velocity.

Finally we analyze the formation number dynamics with the inclusion of a variable diameter orifice nozzle.

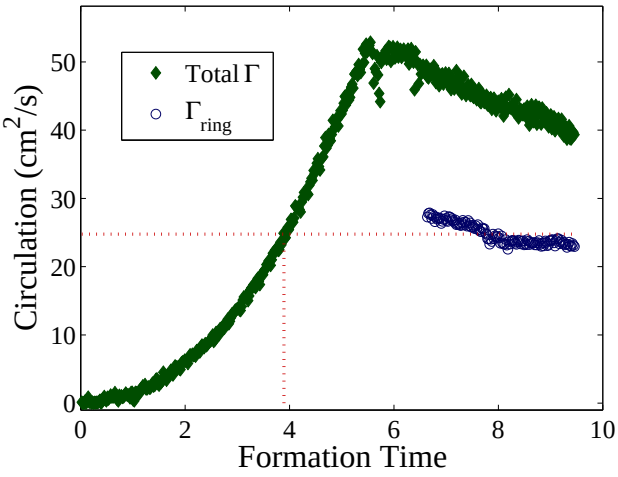

Figure 6.21: Circulation vs. Formation time for a jet ejected from an orifice nozzle with a nozzle radius of 0.9 cm and an accelerating piston velocity.

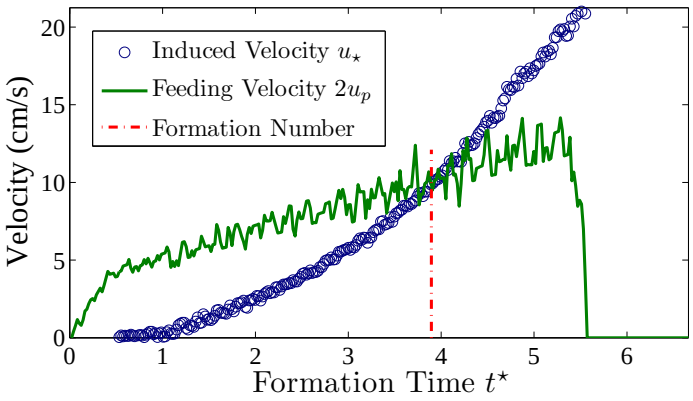

Figure 6.22: Feeding and Induced velocity of the accelerating jet vs. formation time.

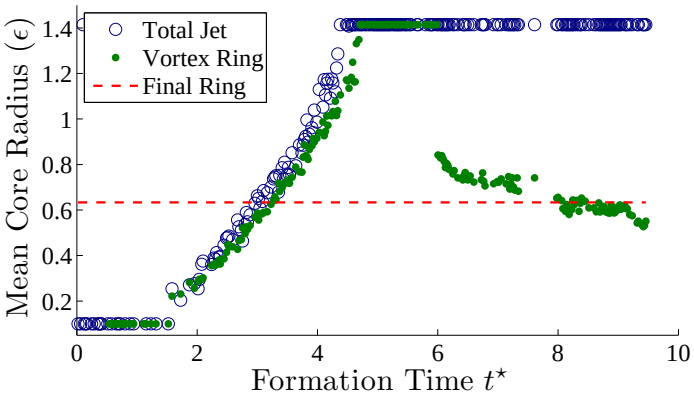

Figure 6.23: Mean core radius, ϵ, of the leading vortex ring shown with respect to formation time, for the jet with accelerating piston velocity.

6.5.3 Constant u_p Variable Nozzle Diameter

Here we would like to take a minute to note the nature of variable diameter nozzles. A jet flow discharging from a variable diameter nozzle will almost inherently contain some component of radial velocity. The most straight forward way to create a parallel jet flow with a variable diameter, is to create a tube nozzle with the ability to expand uniformly along its length, which is well out of the range of our own manufacturing ability. Variable diameter nozzles which change conical shape dynamically pose an interesting problem since at some formation times they create a nearly parallel jet flow, and at other formation times they create a jet flow with significant radial velocity. This makes the effect of these types of nozzles difficult to determine since they are not functionally similar to any single type of static nozzle for comparison. The variable diameter nozzle of this investigation is an iris nozzle which is essentially a flat plate with an adjustable circular orifice in the center. This allows a direct comparison with static orifice type nozzles to determine the effect of increasing/decreasing nozzle radius, independent of any other factors.

The vortex generator was driven with both a linearly increasing and linearly decreasing nozzle radius program. The desired and actual nozzle radii for these tests are shown in Figure 6.24, corresponding to cases 5 and 6 in Table 6.1. For both cases the volume flux program, V(t), was designed to compensate for the variable nozzle diameter and maintain a constant piston velocity, despite the changing nozzle area. Figure 6.24 also shows the the torroidal radius of the leading vortex ring, demonstrating that an increasing radius nozzle will dynamically increase the vortex radius, but the most crucial factor controlling the vortex radius is the initial nozzle radius.

Since the piston velocity is held constant and the nozzle radius program is nearly linear, the formation time defined by (5.3) and (5.4) are nearly identical, with some negligible variations due to an inability to guarantee a perfectly linear nozzle radius program. The total circulation and vortex ring circulation of the jets created with the nozzle radius programs depicted in Figure 6.24 (cases 5 and 6), are plotted in Figure 6.25 with respect to formation time as defined by (5.4). It can be seen in this figure that jets created with both increasing and decreasing nozzle radius have

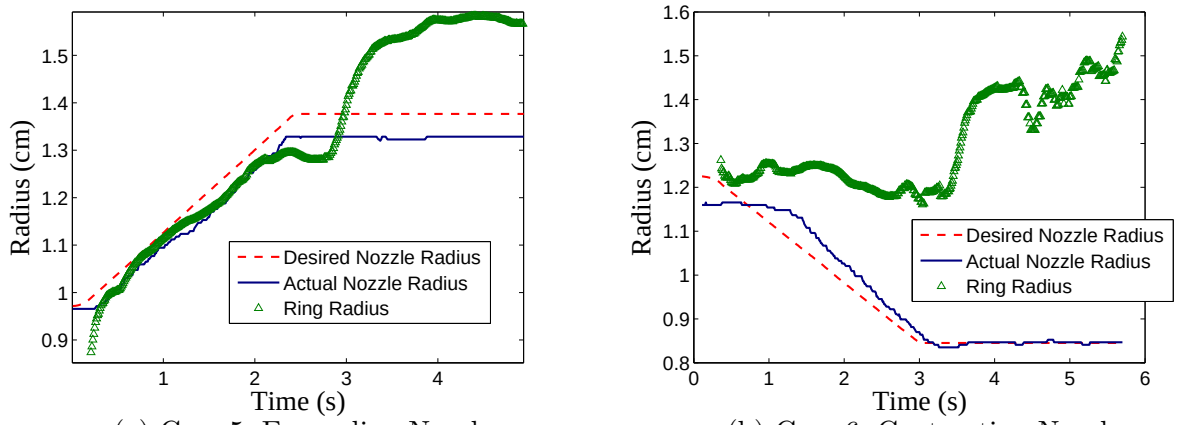

(a) Case 5, Expanding Nozzle

(b) Case 6, Contracting Nozzle

Figure 6.24: The desired and actual nozzle radii are shown for increasing and decreasing radius programs, cases 5 and 6. Also shown is the torroidal radius of the resulting vortex rings.

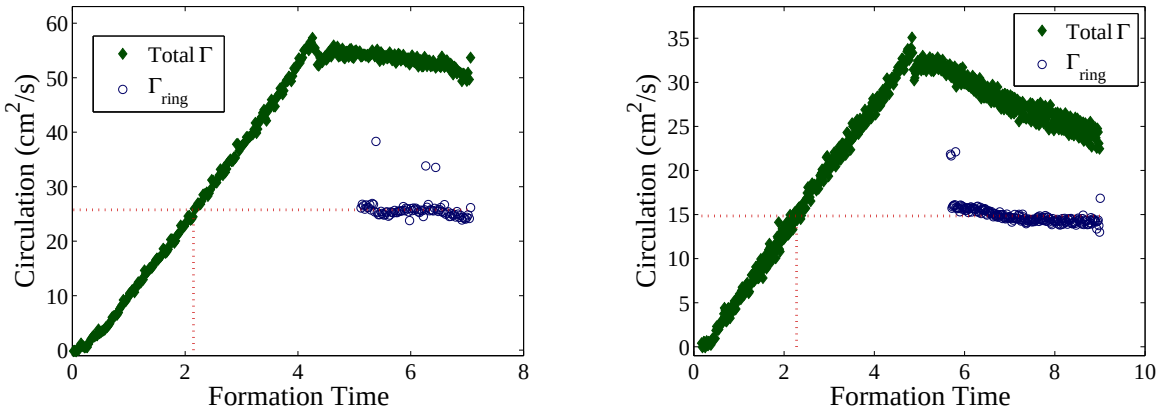

(a) Case 5, Expanding Nozzle, $L/D = 4.2$ (b) Case 6, Contracting Nozzle, $L/D = 4.7$

Figure 6.25: Circulation vs. Formation time, as defined by (5.4), for jets created with linearly increasing and decreasing nozzle radii.

a formation number nearly identical to the constant diameter jet.

Figure 6.26, shows that the centerline velocity criterion still coincides with vortex ring pinch-off for starting jets with variable diameter nozzles. As was just mentioned the formation time is defined as (5.4) for variable diameter devices in an attempt to maintain the relationship between formation number and the configuration of the final vortex ring. To verify this relationship we show the mean core radius of the vortex rings in Figure 6.27. It can be seen that the decreasing radius jet (whose formation number is nearly identical to the formation number of the constant radius jet) has a final mean core radius of $\epsilon \approx 0.55$ which is very close to the mean core radius of the jet expelled through the constant radius nozzle. Similarly the mean core radius of the increasing radius jet is $\epsilon \approx 0.5$, corresponding to a very slight decrease in mean core radius. This decrease in mean core radius is likely due to the increase in vortex ring torroidal radius which accompanies the increasing nozzle radius, see Figure 6.24.

6.6 High Frequency Operation

The dynamics of jet formation have been modeled and verified for a wide variety of nozzle configurations and jet driving programs. However, in all cases the modeling and testing were restricted to cases where both the jetting fluid and the fluid reservoir are starting at rest, and the

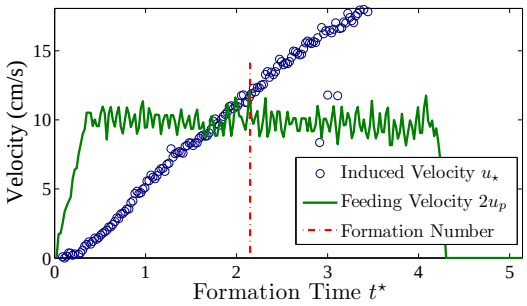

(a) Case 5, Expanding Nozzle

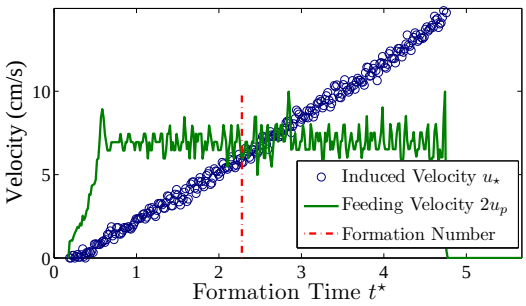

(b) Case 6, Contracting Nozzle

Figure 6.26: Induced and feeding velocity vs. formation time, as defined by (5.4), for jets created expanding and contracting nozzles.

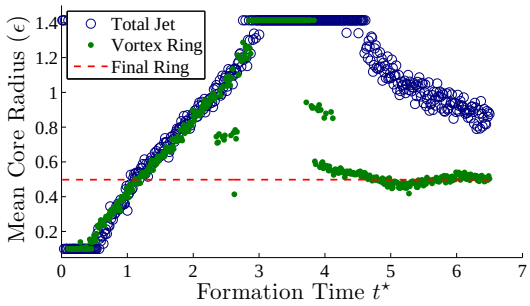

(a) Case 5, Expanding Nozzle

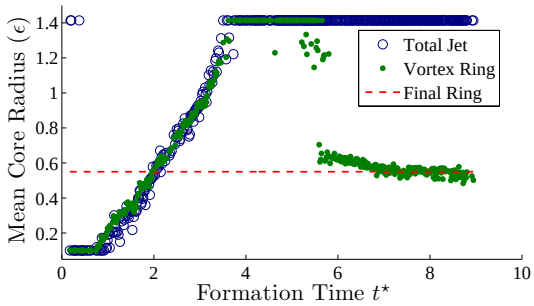

(b) Case 6, Contracting Nozzle

Figure 6.27: Mean core radius, ϵ, vs. formation time, as defined by (5.4), for jets created with expanding and contracting nozzles

jet consists of a single pulsation. Invariably if this technology is used for vehicle maneuvering, then the thruster will be required to operate continuously at some stage. This section describes the average thrust of the thruster pulsating at high frequencies and shows that the average thrust is closely related to vortex ring pinch-off dynamics. The average thrust is defined $\bar{T} = If$, where I is the total jet impulse of each pulsation, and f is the frequency of actuation. It should be noted that the high frequency jets become turbulent at a much lower Reynolds number, as is described in Appendix A, which makes the jets unsuitable for PIV analysis. Here the average jet thrust is determined from direct thrust measurements using a load cell.

In between pulsations the prototype thruster must refill the internal cavity in preparation for the next jet. The prototype thruster of this investigation ingests fluid through the same aperture through which the jet is expelled. Alternatively, the refilling could be supplied from a separate vent, but this option requires complicated valving mechanisms and introduces additional structure to vehicle frameworks, both of which we would like to avoid. Additionally, jellyfish (which loosely inspired this technology) refill the velar cavity through the same opening, and although squid refill through separate vents behind the head they are still on the anterior side of the animal (see Figure 1.1), so losses associated with this type of refilling mechanism might be minimized for certain conditions.

During the refilling phase the impulse transfered to the vehicle cannot be modeled by the starting jet equations (2.5), (2.10), (2.25), and (2.16), because the internal cavity violates the assumption that the only unbounded surface is the nozzle plane, and the interaction of the incoming fluid and the internal cavity walls are significant. In the most simple qualitative sense since the fluid which gets ingested starts out at rest in the reservoir and ends at rest in the internal cavity before being expelled, the net change in momentum of the ingestion cycle is equal to zero. Of course, there is work associated with moving the fluid to the new location, and the pressure at the nozzle plane is not being considered; however, as a first order approximation we will assume that the net impulse of jet refilling is zero.

The thruster analyzed in this section has a sinusoidal piston velocity program with frequency

f. Since the mechanical driving system guarantees a regular controlled piston velocity program at every pulsation, the Buckingham Π theorem predicts that the average thrust equation should reduce to a function of two non-dimensional parameters. The first is a coefficient of thrust defined by,

$$C_T = \frac{\bar{T}}{4R^4\rho f^2} \tag{6.2}$$

The other non-dimensional parameter which characterizes the jet pulsation is the stroke ratio of the jet $\frac{L}{D}$. If the average thrust $\bar{T}$ is calculated from (4.1) with the sinusoidal piston velocity program used by the thruster, then the average thrust is,

$$\bar{T} = \rho\frac{\pi^3}{4}L^2R^2f^2 \tag{6.3}$$

or in non-dimensional terms,

$$C_T = \frac{\pi^3}{16}\left(\frac{L}{D}\right)^2. \tag{6.4}$$

The model assumes that all ingested fluid starts from rest initially and ignores the effect that previously formed vortex rings have on the flow field of the jet. This effect should not be ignored given the rapid succession in which jets are expelled. Experiments were performed by Krueger and Gharib [41], which showed that cyclical jet pulsing had the effect of augmenting the jet thrust as much as 1.9 times the thrust produced by a single jet. The thrust augmentation was considered to be caused by overpressure at the nozzle opening and observed to degrade as the stroke ratio and jet expulsion frequency were increased. The device used to generate the jets studied in [41] differs significantly from the thrusters studied in this paper; due to the fact that the expelled fluid used in [41] was all supplied by an external fluid source, whereas the actuator of our investigation ingests its fluid from the surrounding reservoir.

The pulsation dynamics will be accounted for by a correction factor σ in the average thrust equation (6.4),

$$C_T = \sigma\frac{\pi^3}{16}\left(\frac{L}{D}\right)^2 \tag{6.5}$$

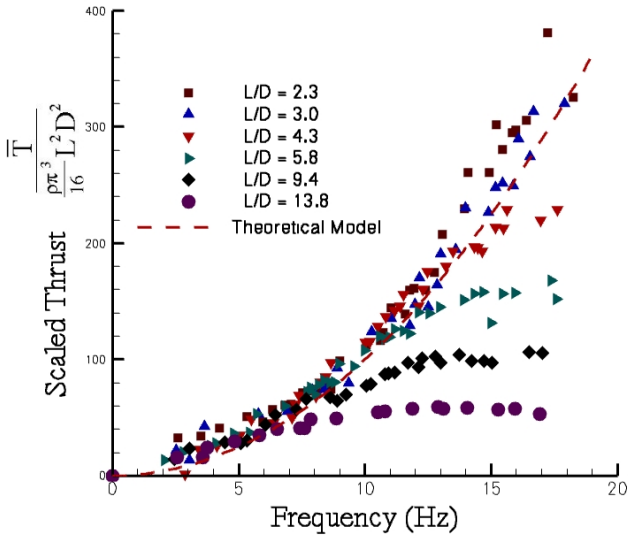

Figure 6.28: Thrust is plotted on the frequency domain for the entire range of stroke ratios tested.

6.6.1 Average Thrust Characteristics

When testing in high frequency mode the prototype thruster is equipped with a set of orifice nozzles which varied in diameter allowing jets to be created with stroke ratios ranging from $L/D = 2$ to $L/D = 14$, independent of velocity program and actuation frequency. In Figure 6.28 the thrust measured for each stroke length has been plotted versus the actuation frequency. The thrust response curves corresponding to low stroke ratios maintain a strong dependency on the square of the frequency, as predicted by equation (6.3), but the higher stroke ratios have a plateau in the thrust response curve as the frequency increases.

It should be noted that the testing was only conducted up to a frequency of $\approx$ 20 Hz. At higher frequencies we observed evidence of cavitation inside the actuator cavity, which is not accounted for in any of the modeling. When the actuator frequency becomes critically high, the pressure drop taking place during the fluid ingestion phase causes the water close to the plunger to expand into small cavitation bubbles. Through the use of a high speed camera (Phantom v4.3 with a wide angle lens) this phenomenon was captured visually. Figure 6.29 shows a close up image of the plunger within the thruster cavity during both phases of actuation (ingestion and expulsion).

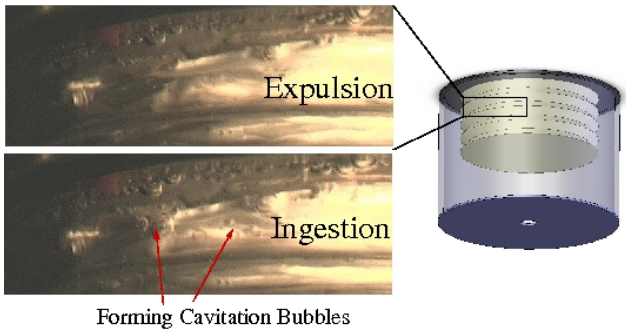

Figure 6.29: Cavitation bubbles within cavity of thruster operating with $f = 17$ Hz and $L/D = 4.3$.

The actuator is operating with a stroke ratio of 4.3 and a frequency of 17 Hz. The lower part of the image shows the plunger just after the ingestion stroke causes a pressure drop resulting in the formation of cavitation bubbles. The upper part of the image shows the piston just after the ejection stroke. Some of the bubbles remain at the top of the plunger, but many of them have imploded due to the sudden increase in pressure. This cycle has the effect of reducing the volume of the ejected jet, since part of the volume change induced by the plunger deflection goes into collapsing the cavitation bubbles instead of ejecting fluids from the orifice. Additionally implosion of the cavitation bubbles results in unpredictable forces acting on the plunger. Therefore, testing was terminated when the increasing frequency resulted in cavitation.

The non-dimensionalization theory predicts that the entire thrust frequency response should converge upon a single coefficient of thrust for each stroke ratio. All thrust measurements have been scaled by the actuation frequency, and orifice diameter to give the coefficient of thrust described in equation (6.2). The average coefficients of thrust measured for the stroke ratios tested have been plotted in Figure 6.30. In addition, the graph contains the theoretical thrust coefficient, as predicted by equation (6.4).

The coefficient of thrust described in equation (6.4) is in good agreement with the measured coefficients for stroke ratios up to ≈ 6 at which point the accuracy of the model degrades with the increasing stroke ratio. This loss of thrust accuracy can be attributed to the pinch-off effect.

The fact that each stroke ratio is represented by a single point in Figure 6.30 is misleading.

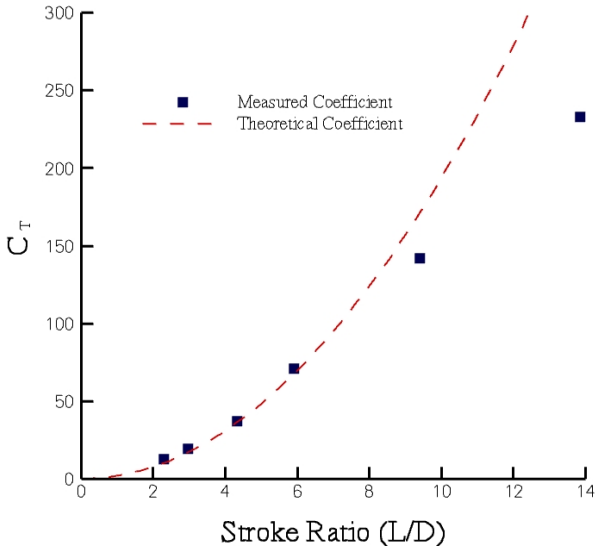

Figure 6.30: Theoretical and measured thrust coefficient as a function of the stroke ratio.

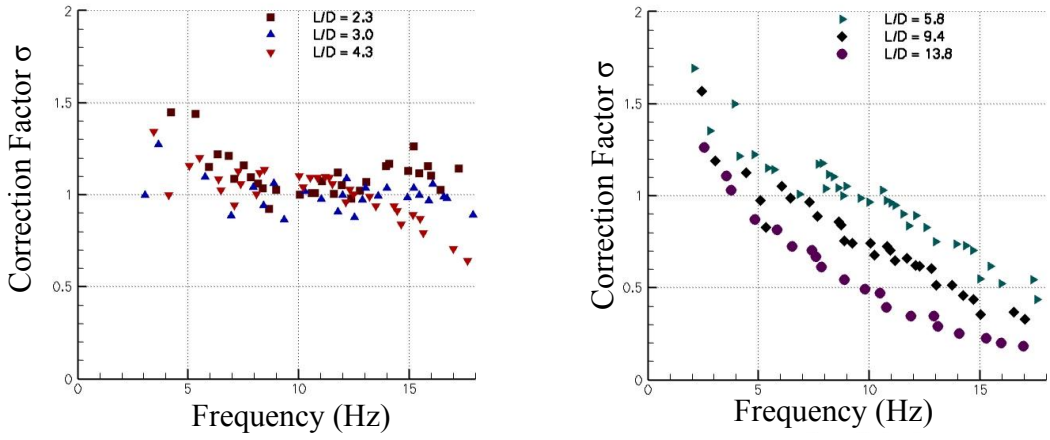

(a) Low L/D (b) High L/D

Figure 6.31: Correction factor σ defined on the actuator frequency domain for (a) stroke ratios below the formation number and (b) stroke ratios above the formation number.

This would suggest that all the thrust data for every formation number converges to a single coefficient of thrust. This is generally true for the thrust measured with stroke ratios below the formation number; however, the thrust coefficient measured for stroke ratios greater than the formation number showed a strong dependence on frequency, and the average was reported. The parameter σ was defined as a correction factor to the slug model approximation (6.3), and shows the accuracy of this model for various actuation frequencies and stroke ratios. Figure 6.31 shows σ for the set of stroke ratios and actuation frequencies tested.

It should be noted that the formation number for an orifice nozzle with a constant velocity program is close to two, but the sinusoidal velocity program must be considered more similar to the accelerating velocity program which has a formation number of four (see Section 6.5). First consider the thrust response of the actuator operating below the formation number Figure 6.31a. In the low frequency regime the average thrust is higher than that predicted by the slug model due to the converging radial velocity at the nozzle exit plane (which was discussed in great detail in Section 6.3). However, as the frequency increases the total thrust settles on the value predicted by the slug model, meaning that in this frequency range the increased impulse due radial velocity during expulsion, which is also referred to as the impulse due to overpressure, is equal to the impulse

due to under-pressure during refilling so that the net impulse transfer is that predicted by the slug model.

Now consider the thruster response when operating above the formation number, shown in Figure 6.31b. Again the low frequency ranges exhibit an added impulse due to the the radial velocity effects, but the high frequency range exhibits an added loss in thrust with respect to the slug model prediction. This relative loss is seen to increase monotonically with both actuation frequency and stroke ratio. This suggests that the assumptions made concerning impulse of the refilling phase are no longer valid when operating above the formation number. We assume that this loss in model accuracy is tied into the assumption made that all fluid being ingested between pulsations is at rest outside of the thruster. When a jet is ejected with a stroke ratio above the formation number, some of the shear flow is left behind in the trailing wake of the leading vortex ring. The trailing wake has a lower momentum than the leading vortex ring and travels at a much lower induced velocity, but still has a forward momentum substantially larger than the surrounding resting fluid. Therefore, the loss in model accuracy could be explained by the thruster ingesting some of the trailing wake during the refilling phase. Figure 6.32 shows successive frames from a video of the thruster's forming jet while operating at a low enough frequency to capture on film, and high stroke ratio, where some of the trailing wake is ingested back into the thruster during the refilling phase.

6.6.2 Transient Thrust

The thrust produced is a highly dynamic one exhibiting large oscillations associated with the pulsatile nature of the device. Section 6.6 presented the average thrust characteristics, and their dependence on driving frequency and stroke ratio. A complete description of the transient characteristics of the thruster in high frequency mode is not only desirable from a vehicle design standpoint, but necessary for the implementation of any high accuracy control algorithm

There are two major characteristics of the thruster's transient behavior, while operating in high frequency mode, which were observed in [35]. The first feature is a rise time associated with

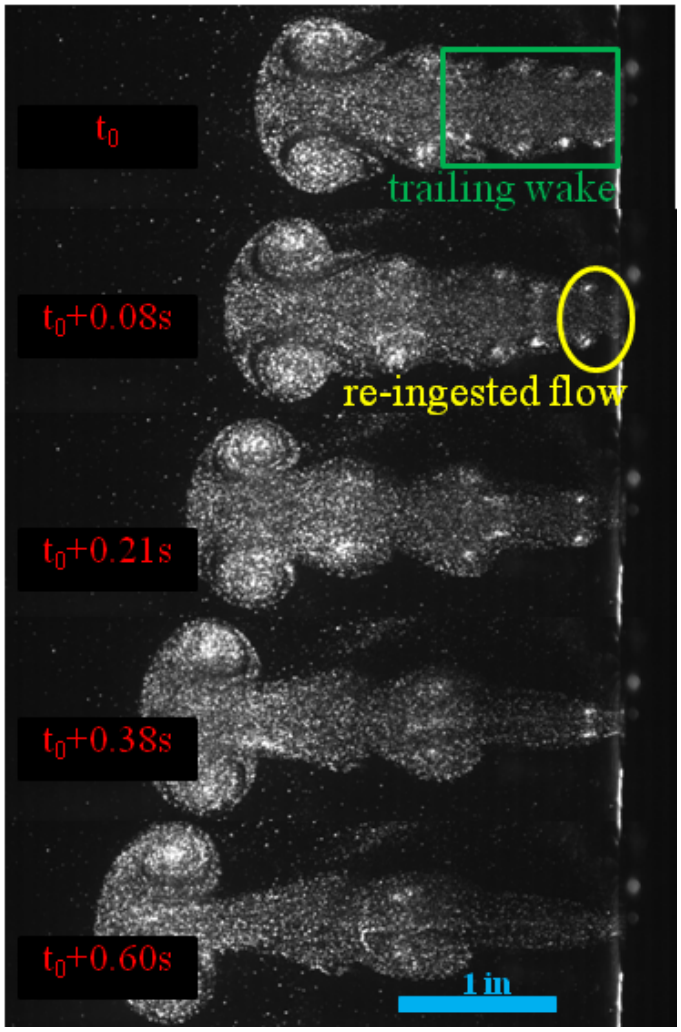

Figure 6.32: Successive frames of jet flow showing the thruster re-ingesting wake flow, of high stroke ratio jets.

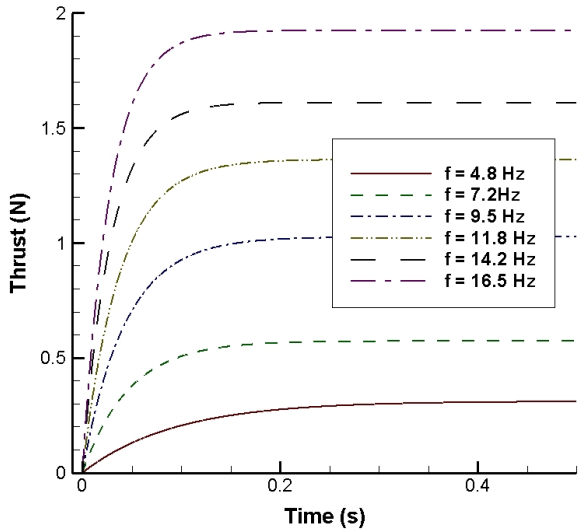

Figure 6.33: Thruster transient response fitted to a first order delay

reaching the average thrust. Similar to propeller type thrusters [98, 20], the VRT has time delays which are inversely proportional to the desired level of thrust. However, it should be noted that this type of thruster has rise times on the order of fractions of a second; whereas, typical propeller type thrusters experience rise times on the order of several seconds [98, 20]. The rise time can be modeled in similar terms to a first order linear damper $\frac{dT_{DC}}{dt} = \left(\bar{T} - T_{DC}\right)\frac{1}{\tau}$. In this expression $\bar{T}$ is the steady average level of thrust discussed in Section 6.6, which is purely a function of the driving parameters (and can therefore be thought of as a control signal), T_{DC} is the DC component of the transient thrust signal, and τ is a time constant which is a function of $\bar{T}$. Assuming that the thruster starts at rest and that the steady state thrust is held constant the solution of the thrust equation becomes

$$T_{DC}(t) = \bar{T}\left(1 - e^{-t/\tau}\right). \tag{6.6}$$

Several time dependent thrust data sets were analyzed to determine the rise time dependence on steady thrust level. Using a least square approximation the transient thrust sets were fit to the form (eq:damper) to determine the damping time constant τ for each set. The fitted curves for these dynamic data sets are given in Figure 6.33. Dimensional analysis suggests that the rise time dynamics should converge to a single non-dimensional equation. Consider the non-dimensional equation,

$$\bar{T}^{\star}(t^{\star}) = 1 - e^{-t^{\star}/\tau^{\star}}, \tag{6.7}$$

where $\bar{T}^{\star} = \frac{T_{DC}}{\bar{T}}$ is the thrust normalized by the average steady state thrust, and the time is normalized as $t^{\star} = tf$ with characteristic time scale selected to be the most pertinent time scale associated with the thrust level, the pulsation period, $\frac{1}{f}$. The data sets shown in Figure 6.33 were all normalized to the new variables $\bar{T}^{\star}$ and $t^{\star}$. The set of normalized curves are shown in Figure 6.34. This graph clearly shows that normalizing the thrust by the steady state value and the time by the oscillation period results in self similar behavior of the average thrust rise time. Depicted as a solid line is the average thrust rise time curve where $\tau^{\star} = 0.38$, which is the average of all the data sets. The actual normalized data sets are shown by the dotted lines.

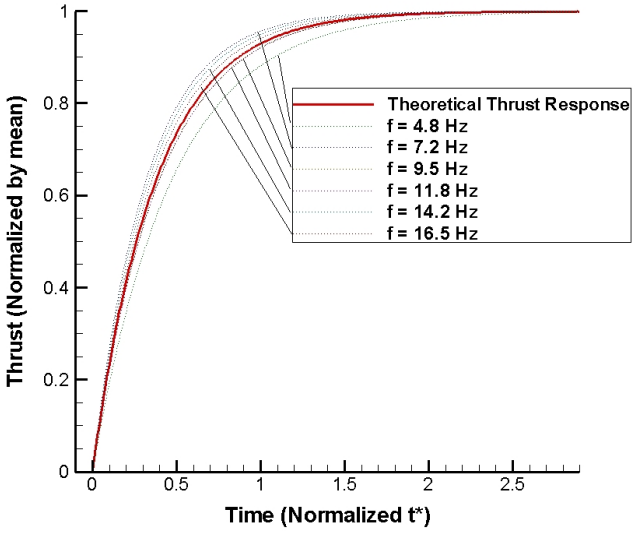

Figure 6.34: Normalized thrust $\bar{T}^{\star}$ vs. normalized time, for all cases of steady state thrust, $\bar{T}$. Actual thrust values shown with dotted lines, theoretical curve based on average time constant shown in solid red

The second feature of the transient thruster response (which remains undamped throughout actuation) is a sinusoidal wave mode associated with the pulsation of the actuator. When these two modes are incorporated into the average thrust equation it takes on the following form

$$T(t,f) \simeq \bar{T}\left(1 - e^{-tf/\tau^\star}\right) + a\sin(2\pi f t), \tag{6.8}$$

where f is the pulsation frequency of the thruster, and a is the amplitude of oscillation associated with the pulsation, which can be determined from the slug model along with the steady state thrust. The slug model predicts that the amplitude a is proportional to the square of the actuation frequency, so that the ratio $a/\bar{T}$ is a constant for all driving frequencies. This ratio will be denoted η. For a thruster with a sinusoidal jet velocity profile, like the one used in the high frequency experiments, this ratio has a value of $\eta = 4$. Taking this relation into account and incorporating the steady state thrust equation (6.3) gives an equation for the thrust as a function of time and actuation frequency,

$$T(t,f) \simeq C_v f^2 \left[\left(1 - e^{-tf/\tau^\star}\right) + \eta\sin(2\pi f t)\right] , \tag{6.9}$$

with $C_v = \rho\dfrac{\pi^3}{16}L^2D^2$ being a thruster constant describing the operating parameters of the thruster (since D and L are fixed during high frequency operation).

Chapter 7

Optimal Thruster Velocity Programs

In section 6.6 the prototype thruster was observed to suffer losses due to trailing wake re-ingestion when operating at high frequencies with a stroke ratio above the formation number. However, the formation number can be shifted by adjusting the rate of circulation and impulse added to the system (i.e. changing the piston velocity and nozzle radius during pulsation). This limitation on thruster performance provides a necessary constraint for determining optimal driving programs, as will be formalized in this section.

The optimization problem can be stated as finding the critical nozzle radius and piston velocity program, for a single pulsation, which maximizes certain design parameters (performance indices), while satisfying the dynamic constraint that the final jet stroke length is less than (or equal to) the resulting formation number for that jet flow. This optimization will not incorporate the refilling phase, as the dynamics of the refill phase are poorly understood.

The variable diameter mechanism works well for creating low velocity starting jets with either increasing or decreasing shear layer radius during pulsation; however, the variable diameter nozzle is very complicated mechanically, and may not be ideal for use in high frequency operation. This initial optimization analysis will assume that the nozzle radius remains constant throughout pulsation, but can vary from pulsation to pulsation. The piston velocity will be allowed to vary during pulsation, and the chosen velocity program will repeat every pulsation. The internal cavity diameter will also be prescribed as an initial condition meaning that the normalized radial slopes, $k_1^\star$ and $k_2^\star$, will also remain constant independent of the choice of nozzle radius or piston velocity

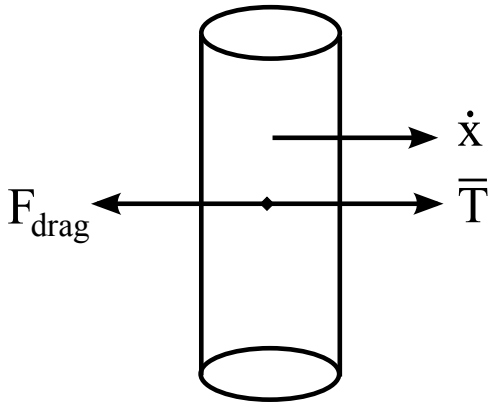

Figure 7.1: Hypothetical vehicle with one degree of freedom (in the x direction).

program; however, the values of $k_1^\star$ and $k_2^\star$ will change depending on whether an orifice or tube nozzle is attached to the thruster. Therefore, the control space for this optimization problem consists of the selection of the static nozzle radius, R, the piston velocity program, $u_p(t)$, and the nozzle configuration. The constant radius assumption also allows the feasible thruster control space to be conceptualized much more easily, which helps to clarify the effect of the dynamic formation number constraint.

7.1 Performance Indices (Cost Functions)

The first performance index we will investigate is the average thrust created by a single pulsation. This correlates to a critical mission scenario where vehicle survival is dependent on sufficient corrective thrust, and propulsive efficiency is less important. The average thrust of a single pulsation is just the final impulse of the propulsive jet, I_f, divided by the final time when the flow is terminated t_f,

$$\bar{T}_e = \frac{I_f}{t_f} \, . \tag{7.1}$$

The average thrust over the entire jetting cycle, $\bar{T}$, which was characterized in Section 6.6, is related to the average thrust of the pulsation phase as $\bar{T} = \bar{T}_e \lambda$, and λ is the limit cycle of the pulsation, or ratio of the time spent jetting to the time spent refilling.

The other performance index which is advantageous to a vehicle maneuvering system is an

optimal propulsive efficiency. In the absence of more critical concerns, the propulsive efficiency should always be maximized. However, propulsive efficiency is a difficult measure to quantify for a thruster independent of a specific vehicle environment. Propulsive efficiency is defined,

$$\eta_p = \frac{W_p}{W_s} \,, \tag{7.2}$$

where, W_s, is the total mechanical work required to create the propulsive flow, or shaft work, and W_p is the useful propulsive work done on the vehicle. If the vehicle is being acted on by propulsive force $\vec{F}$ and moves with position $\vec{x}$, then $W_p = \int \vec{F} \cdot d\vec{x}$. Consider a simple one degree of freedom vehicle as depicted by figure 7.1, which is being driven by the thruster of this study operating continuously at a high frequency. Due to the pulsatile nature of the thrust, the vehicle velocity will oscillate in phase with the thruster pulsations. After some time the vehicle will reach a quasi-equilibrium state where the velocity oscillates around a steady average velocity. Furthermore, if the vehicle is relatively large, with respect to the impulse of an individual pulsation, then the fluctuation in velocity will be small compared to the average velocity and the vehicle velocity can be approximated as a constant value.

With a constant velocity the propulsive work can be rewritten, $W_p = \bar{T}\Delta x$. Furthermore, when the vehicle is traveling at a constant velocity, the propulsive force and drag force are in equilibrium, $\bar{T} = F_{\text{drag}} = \frac{1}{2}\rho A_w C_D \left(\frac{dx}{dt}\right)^2$, where ρ is the fluid density, A_w is the wetted area of the vehicle in the direction of motion, and C_D is the coefficient of drag of the vehicle. The coefficient of drag of a cylinder is relatively constant in the high Reynolds number regime around $C_D \approx 0.81$, in the low Re regime the coefficient of drag is inversely proportional to the Reynolds number $C_D \approx 10/Re$. Here Reynolds number is defined, $Re = \dot{x}d/\nu$, where d is the vehicle diameter, and ν is the kinematic viscosity of the fluid. Therefore in the high Reynolds number regime the vehicle velocity can be approximated,

$$\frac{\Delta x}{\Delta t} = \left[\frac{2\bar{T}}{\rho A_w C_D}\right]^{1/2} \,, \tag{7.3}$$

and in the low Reynolds number regime,

$$\frac{\Delta x}{\Delta t} = \frac{d\bar{T}}{5\rho A_w \nu} \,. \tag{7.4}$$

The constant vehicle velocity approximation allows the propulsive work to be defined for a single pulsation cycle, in the high Re regime the propulsive work is,

$$W_p = \frac{\Delta t \bar{T}^{3/2}}{\left[\frac{1}{2}\rho A_w C_D\right]^{1/2}} = \frac{I_f^{3/2}}{\Delta t^{1/2}\left[\frac{1}{2}\rho A_w C_D\right]^{1/2}} , \tag{7.5a}$$

and for low Re

$$W_p = \frac{d\Delta t \bar{T}^2}{5\rho A_w \nu} = \frac{2dI_f^2}{5\Delta t \rho A_w \nu} , \tag{7.5b}$$

where I_f is the total impulse of the jet, and $\Delta t = 1/f = t_f/\lambda$ is the time it takes for a complete pulsation cycle. This analysis is not intended to drive the selection of fluid driving mechanism; therefore, all energy losses in the motor and plunger will be ignored. This means that the total shaft work during the expulsion phase is just the total kinetic energy of the jet at the end of pulsation, E_f. This leads to the definition of a quantity we call the jetting efficiency,

$$\eta_{JH} = \frac{I_f^{3/2}}{t_f^{1/2} E_f \left[\frac{1}{2}\rho A_w C_D\right]^{1/2}} , \tag{7.6a}$$

$$\eta_{JL} = \frac{I_f^2 d}{t_f E_f 5\rho A_w \nu} . \tag{7.6b}$$

The jetting efficiency does not consider the jetting limit cycle, or the shaft work required for the refilling phase both of which must be included to determine propulsive efficiency. However, the jetting efficiency should be considered similar to propulsive efficiency and the two will be maximized by similar piston velocity programs and nozzle radii, and the refill phase must be optimized independently to acquire a truly optimal propulsive efficiency. For this analysis we assume that the vehicle thruster has the same scale and geometry as the prototype thruster and is operating on a basic cylindrical vehicle with a diameter of, $d = 10$ cm, and a wetted area of, $A_w = 1000$ cm^2. The values of density and kinematic viscosity of water are set to 1 g/cm^3, and 0.01 cm^2/s, respectively.

7.2 System Dynamics

The circulation, impulse, and energy of the jet are calculated assuming that the axial velocity profile is uniform (4.1), and the radial velocity profile is linear (4.6), which can be summarized,

$$\frac{d\Gamma}{dt}_{\text{1D+2D}} = \frac{1}{8}u_p^2\left(4 + k_2^\star\right) \ , \tag{7.7a}$$

$$\frac{dI}{dt}_{\text{1D+2D}} = \frac{\rho\pi}{16}u_p^2 R^2\left(16 + k_2^\star - k_1^{\star 2}\right) \ , \tag{7.7b}$$

$$\frac{dE}{dt}_{\text{1D+2D}} = \frac{\rho\pi}{16}u_p^3 R^2\left(8 + k_2^\star\right) \ . \tag{7.7c}$$

It should be noted that the initial high frequency testing showed that the effect of the radial velocity is not observed in the average thrust above ≈ 4 Hz, meaning that the increased impulse due to the radial velocity components is negated by an equal negative impulse from the converging radial velocity during refilling. We leave the radial terms in the jet dynamics because it is possible that the refilling phase could be optimized in future studies to eliminate 'under-pressure', but results will still apply to the 1D slug model if the radial slopes are set to zero, $k_1^\star = k_2^\star = 0$.

7.3 Incorporating Constraints, Control Space Restrictions

In a truly unbounded control space, meaning that there are no limitations placed on possible nozzle radius and piston velocity, there is no local optimal velocity program which maximizes either performance index. In this case the maximum average thrust is generated by expelling the fluid with an infinite velocity in an infinitely short period of time, and the optimal jetting efficiency, η_J, is stationary with respect to piston velocity in the high Reynolds number regime, and is realized in both regimes by setting the nozzle radius infinitely large. Therefore, any locally optimal program relies on the constraints of the problem.

The first constraint on this thruster is that the jetting volume is finite, which is also one of the key differences between this type of propulsion and continuous jet propulsion used in recreational watercraft. This is a terminal constraint which is enforced by setting the final volume expelled from the thruster equal to the available jet volume, V_{jet}. Additionally, the rate at which volume

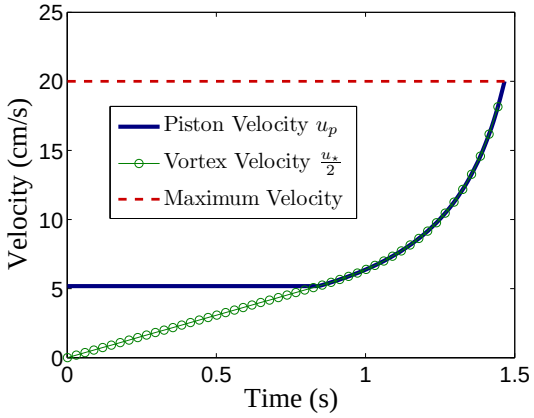

Figure 7.2: An example of possible piston velocity program under the formation number constraint.

is ejected $\dot{V} = \pi R^2 u_p$ is bounded by the physical limitations of the fluid driving mechanism. This is enforced by the inequality $u_p \leq \dot{V}_{\max}/\pi R^2$, which provides a boundary for an admissible region in the control space. If a local optimum exists within the admissible region then the inequality is ignored, otherwise the optimal controls will lie on the boundary of this admissible region.

The final constraint that the jet stroke ratio must be less than the formation number of the resulting flow can be enforced by the inequality, $2u_p \geq u_\star$, where $u_\star$ is the centerline velocity at the origin of the vortex ring (5.16). Again this constraint defines an additional boundary on the admissible region of the control space, but this boundary is a dynamic function of the velocity program itself, and optimal programs which lie on this boundary will be dependent on the initial conditions that created this boundary. To illustrate this point consider an example velocity program shown in Figure 7.2. This figure shows the piston velocity of a hypothetical jet which starts out at some constant piston velocity u_{p0}, and nozzle radius R, as well as the resulting vortex centerline velocity. It can be seen that the jet velocity starts out constant and is then forced to accelerate to account for the accelerating vortex ring velocity. This is a representation of the formation number constraint in the control space. At the onset of flow the vortex ring velocity is very small and the velocity program will remain unaffected since the dynamic formation number constraint is being satisfied in this initial stage. However, the vortex ring velocity grows until the boundary of the admissible control region intersects the constant piston velocity, which is forced to accelerate to

stay in the admissible region of the formation number constraint. It is not hard to imagine that changing the initial nozzle radius and piston velocity program will result in very different behavior because these quantities will change how the formation number constraint shapes the boundary of the admissible control region.

Therefore, the optimization of the piston velocity program and nozzle radius does not rely on finding a locally optimal trajectory within the admissible control region, but rather finding critical values of the initial nozzle radius and piston velocity program which optimize the admissible region in the control space resulting from the formation number constraint. Here we will make one final restriction that the piston velocity program will be held constant in the initial formation stages before the formation number constraint forces an acceleration of piston velocity. This restriction reduces the control space of the problem to the vector $\vec{u} = [u_{p0}, R]^T$, which is the selection of initial piston velocity and nozzle radius. This restriction also aids in conceptualizing the control space of the problem, which helps to identify the effect of the dynamic formation number constraint.

7.4 Velocity Program Derivation

If the nozzle radius is selected greater than some critical value $R^\star$, then the jet stroke ratio (which is only a dependent on nozzle radius since total jet volume is held constant) will always be lower than the resulting jet formation number independent of the choice of initial piston velocity. The critical radius can be defined in terms of the jet volume and radial slopes,

$$R^\star = \left[\frac{V_{\text{jet}} \left(4 + k_2^\star\right)^{3/2}}{2^{9/2}\pi \left(16 + k_2^\star - k_1^{\star 2}\right)^{1/2}} \right]^{1/3} . \tag{7.8}$$

If the nozzle radius is above the critical radius, then the entire control space will be within the admissible region of the formation number constraint. Therefore, ignoring this constraint gives the optimal piston velocity on the boundary of the thruster limitations, $u_p = \dot{V}_{\max}/\pi R^2$.

If the nozzle radius is below the critical value, $R^\star$, then at some time t_1 the piston velocity will intersect half the vortex ring velocity. We denote the circulation, impulse, energy, and volume at this time, Γ_1, I_1, E_1, and V_1 respectively. Setting $2u_{p0} = u_\star\left(\Gamma_1, I_1\right)$ allows the intersection time,

t_1, to be calculated, which also allows all the quantities at this time to be calculated.

$$t_1 = \frac{2^(9/2)A^(1/2)R}{u_{p0}\,(4+k_2^\star)}\ , \tag{7.9a}$$

$$\Gamma_1 = 2^{3/2}A^{1/2}Ru_{p0}\ , \tag{7.9b}$$

$$I_1 = \pi 2^{1/2}A^{3/2}R^3u_{p0}\ , \tag{7.9c}$$

$$E_1 = \pi 2^{1/2}A^{1/2}R^3u_{p0}^2\frac{8+k_2^\star}{4+k_2^\star}\ , \tag{7.9d}$$

$$V_1 = \frac{\pi 2^{9/2}A^{1/2}R^3}{4+k_2^\star}\ , \tag{7.9e}$$

where,

$$A = \frac{16+k_2^\star-k_1^{\star 2}}{4+k_2^\star}\ . \tag{7.9f}$$

After this time the piston velocity lies on the boundary of the formation number constraint meaning that $u_p = u_\star/2$. Inserting this relation for piston velocity back into the system dynamics (7.7) provides an ordinary differential equation for the jet circulation, since impulse is proportional to circulation reducing the vortex centerline velocity to a function of circulation, $u_\star \propto \Gamma$, when the nozzle radius is held constant.

Inserting this relation for piston velocity back into the system dynamics (7.7) gives an ordinary differential equation for the circulation. Solving this equation for circulation under the initial condition that $\Gamma(t_1) = \Gamma_1$ results in a function for the circulation on this boundary in terms of time and initial piston velocity,

$$\Gamma = \frac{2^6AR^2u_{p0}}{2^(11/2)A^{1/2}R-(4+k_2^\star)u_{p0}t}\ . \tag{7.10}$$

Which in turn allows the piston velocity to be determined for this region,

$$u_p = \frac{2^{9/2}A^{1/2}Ru_{p0}}{2^{11/2}A^{1/2}R-(4+k_2^\star)\,u_{p0}t}\ . \tag{7.11}$$

Given the piston velocity all other quantities can be solved from (7.7). As was mentioned previously, the terminal constraint is defined by the total available jet volume, V_{jet}. Setting the final volume (integrated from the piston velocity equation) equal to the total available jet volume

determines the final time,

$$t_f = \frac{2^{9/2} A^{1/2} R}{(4 + k_2^\star)\, u_{p0}} \left[2 - e^{1 - \frac{(4+k_2^\star) V_{\text{jet}}}{\pi 2^{9/2} A^{1/2} R^3}} \right] . \tag{7.12}$$

Finally, the physical limitations of the thruster driving mechanism bound the allowable piston velocity at the final time, which can be translated into a constraint on the choice of initial piston velocity, u_{p0}, for a given nozzle radius, R. By requiring $u_{pf} \leq \dot{V}_{\max}/\pi R^2$, the initial piston velocity is constrained to,

$$u_{p0} \leq \frac{\dot{V}_{max}}{\pi R^2} e^{1 - \frac{(4+k_2^\star) V_{\text{jet}}}{\pi 2^{9/2} A^{1/2} R^3}} . \tag{7.13}$$

Meaning that for a given nozzle radius there is a maximum initial piston velocity that can be chosen which will satisfy both the thruster driving constraint and formation number constraint throughout the entire pulsation.

Summary of Constrained Problem This means that under these constraints and restrictions we do not have complete control over the piston velocity program. Once a nozzle radius has been selected, the constraints on the problem limit the choice of initial piston velocity as is described by (7.13). The piston velocity for maximum average thrust will always tend towards the maximum allowable velocity for that region, and the initial piston velocity will be chosen as the maximum allowable value. Therefore, the optimization problem can be restated as finding the nozzle radius which maximizes average thrust, $\bar{T}_e$, or the nozzle radius initial piston velocity combination which maximizes jetting efficiency, η_J, with final pulsation time defined by (7.12), and total jet impulse and energy defined by integrating the system dynamics (7.7). The constraints are all automatically satisfied since the piston velocity program used to integrate the system dynamics is derived based on the constraints.

7.5 Results

It can be seen in the preceding section that the constraints placed upon the problem, reduce the control space to the selection of the initial nozzle radius, R, for the average thrust optimization, and the selection of the nozzle radius and initial piston velocity, $[R, u_{p0}]$ for the jetting efficiency

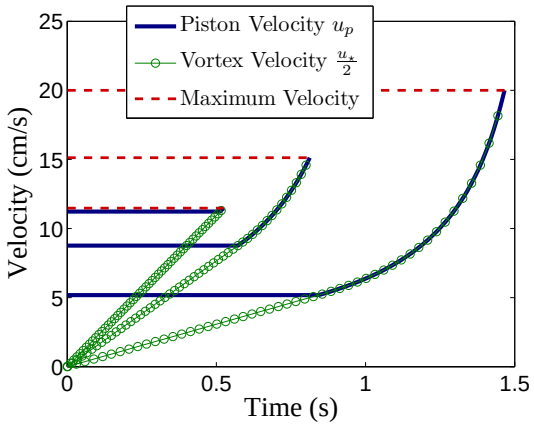

Figure 7.3: Piston velocity programs resulting from multiple nozzle radii.

optimization. Using typical values for V_{jet} and $\dot{V}_{\max}$ from the prototype thruster, the piston velocity program $u_p(t)$ and the performance indices, $\bar{T}_e$ and η_J were calculated for a range of feasible nozzle radii, and initial piston velocities. Multiple values were used for the radial slopes. $k_1^\star = 0$ and $k_2^\star = 0$ correspond to the dynamics of a truly parallel jet (1D slug model), but we also calculated the performance indices with $k_1^\star = -1$ and $k_2^\star = 4$ which are typical of starting jets expelled through orifice nozzles (see Table 6.1). Figure 7.3 shows multiple piston velocity programs resulting from the nozzle radius selection, and choosing the maximum allowable initial piston velocity. The general shape of the piston velocity was not affected by the radial velocity slopes.

The average thrust of the jet, $\bar{T}_e$, is depicted in Figure 7.4, as a function of nozzle radius for both sets of radial slopes. It can be seen that under the constraints used here the average thrust of the pulsation will be maximized, when the nozzle radius is equal to the critical nozzle radius, $R^\star$, and the resulting piston velocity program is just the maximum piston velocity bounded by the limitations of the thruster driving mechanism. For this particular control program, the piston velocity and vortex ring velocity do not intersect until the final pulsation time. This is the case for both sets of $k_1^\star$ and $k_2^\star$, even though the different slopes will result in jets with drastically different formation number. It should be noted that the case of $k_1^\star = -1$, and $k_2^\star = 4$ will have a lower formation number, and therefore, a larger critical radius and lower maximum piston velocity at the critical radius. As a result the maximum average thrust is actually lower for the converging

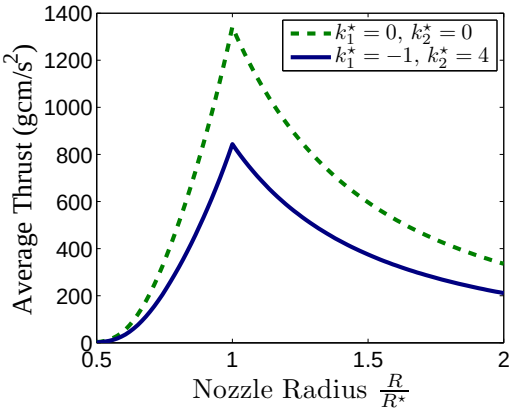

Figure 7.4: Average thrust, $\bar{T}_e$, resulting from choice of nozzle radius under the constraints that total ejected volume, V, is equal to jet volume, V_{jet}, piston velocity, u_p, is below the maximum piston velocity, $\dot{V}_{\max}$, and piston velocity is larger than half the vortex ring velocity, $u_\star/2$.

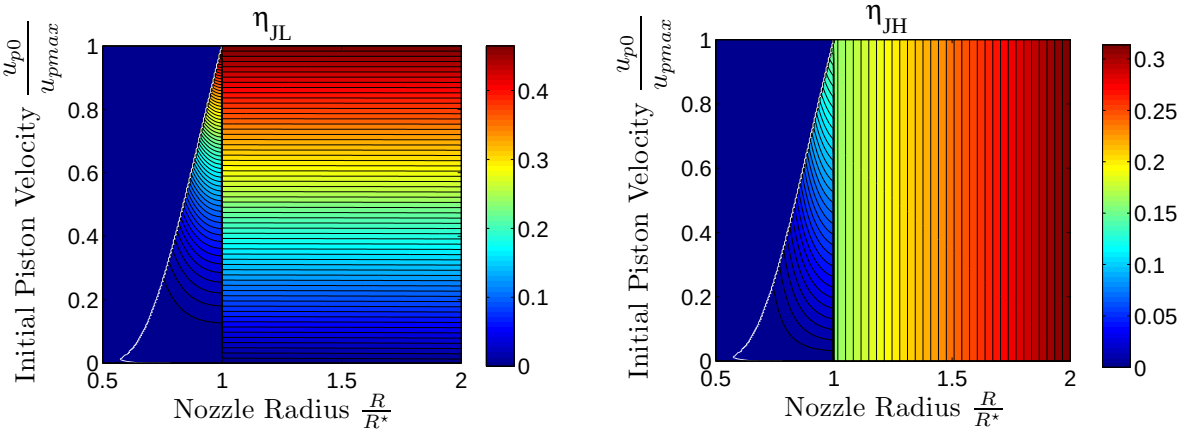

(a) Low Re (b) High Re

Figure 7.5: Jetting efficiency, η_J, is shown for the admissible range of nozzle radius and initial piston velocity for both low and high Re regimes. The boundary of the admissible control space is marked by the solid white line, and $k_1^\star = -1$ and $k_2^\star = 4$ for both regimes.

jet. This would suggest that the maximum average thrust is reached by jets with a large formation number; however, increasing the formation number by accelerating the piston velocity does not increase the average thrust, as indicated by the average thrust values for nozzle radius below the critical radius.

The jetting efficiency in the low Reynolds number regime, $\eta_J L$, for the converging nozzle configuration ($k_1^\star = -1$ and $k_2^\star = 4$) is shown over the same range of nozzle radius as well an admissible range of initial piston velocities in Figure 7.5(a) and Figure 7.5(b) shows the jetting efficiency for high Re and the same control space. When the nozzle radius is selected below the critical radius there is a maximum initial piston velocity defined by equation (7.13), and this boundary in the control space is marked by the solid white line in Figure 7.5. It can be seen from this figure that the jetting efficiency drops of drastically when the nozzle radius is selected below the critical radius for both regimes, meaning that accelerating the piston velocity to increase the formation number of the jet is in general not beneficial to the propulsive efficiency. If the nozzle radius is above the critical radius this figure shows that a vehicle operating at low Reynolds numbers will experience a maximum jetting efficiency with maximum piston velocity and is independent of the nozzle radius (provided that radius is above the critical value). Conversely, a vehicle operating

at high Re experiences a maximum efficiency with maximum nozzle radius but is insensitive to selection of initial piston velocity.

The jetting efficiency for the parallel jet has nearly identical shape as the converging jet for both velocity regimes. In order to show the quantitative effect of non-parallel jets on jetting efficiency we again restrict the control space to just the selection of nozzle radius, and the initial piston velocity is selected to be the maximum allowable for that radius. Figure 7.6 shows the jetting efficiency for both velocity regimes and both nozzle configurations. It can be observed that the converging radial velocity has a higher jetting efficiency for the same constraints in the high Re regime, suggesting that jetting efficiency is maximized by thin cored vortex rings in this regime. Whereas, the parallel jet has a higher jetting efficiency in the low Re regime.

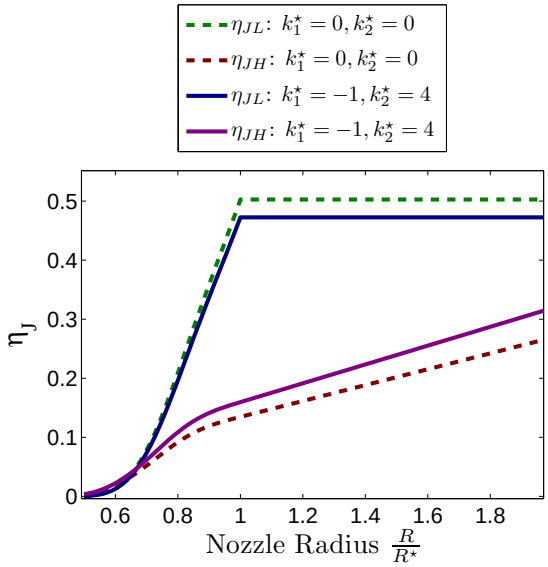

Figure 7.6: Jetting efficiency, η_J, resulting from choice of nozzle radius under the constraints that total ejected volume, V, is equal to jet volume, V_{jet}, piston velocity, u_p, is below the maximum piston velocity, $\dot{V}_{\max}$, and piston velocity is larger than half the vortex ring velocity, $u_\star/2$.

Chapter 8

Vehicle Integration

So far the analysis of this new type of thruster has focused heavily on jet dynamics. Here considerations are made for the implementation of such a thruster in typical vehicle control environments.

8.1 Transfer Function Approximation

Any high accuracy maneuvering system will be required to operate in chaotic environments. The energy of these turbulent marine environments is well defined in the spectral domain [64]. A Linear time invariant (LTI) transfer function model of the thruster dynamics is desirable since it allows the thruster parameters to be selected with respect to the mission specific environmental dynamics.

If the thrust equation (6.9) is mapped into the spectral domain through a Laplace transform it becomes a nonlinear integral function of the frequency input, which can be linearized by setting the input function, which in this case is the frequency, equal to a weighted Heaviside function $f(t) = f_0 \int_0^t \delta(\tau) d\tau$ trimmed at some nominal pulsation frequency f_0. The linearized thrust equation in the spectral domain is

$$\hat{T}(f,s) \approx C_v \left(\frac{f_0^2}{s} - \frac{f_0^2}{s + f_0/\tau^\star} + \frac{\eta 2\pi f_0^3}{s^2 + 4\pi^2 f_0^2} \right). \tag{8.1}$$

The transfer function plant for the thruster is therefore the ratio $\frac{\hat{T}(s)}{F(s)}$, where $F(s)$ is the Laplace transform of the input function $F(s) = \int_0^\infty f(t)dt = \frac{f_0}{s}$. Using this relation the thruster

plant can be determined. This should be an accurate approximation so long as the rate of change of $f(t)$ is slow with respect to the rate of change of $x(t)$

$$G_{\mathrm{VRT}}(s) = C_v \left(\frac{f_0^2}{\tau^\star s + f_0} + \frac{\eta 2\pi f_0^2 s}{s^2 + 4\pi^2 f_0^2} \right). \tag{8.2}$$

Therefore the thruster plant describes the linearized dynamics between the input actuation frequency and output thrust, and is purely a function of the trim frequency f_0.

The accuracy of the linearized transfer function approximation was tested by operating the thruster in a hybrid vehicle simulation and interpolating the system frequency response. A method is used whereby the behavior of a vehicle is modeled as a virtual vehicle; and the thrust is measured empirically from the prototype thruster in a controlled static setup. Using this procedure the validity of the thruster model can be tested with respect to a "pure" vehicle which acts predictably according to the fully non-linear drag equations. Also approximation/modeling errors may be determined independently from inconsistencies due to environment unpredictability. The virtual vehicle was modeled by a simple cylinder with a single degree of freedom (perpendicular to the long axis) suspended in an incompressible fluid. The governing equation for the simple vehicle simulation is just Newton's second law with a nonlinear drag term.

The virtual vehicle model assumes that the vehicle starts at rest. At the onset of the experiment the vehicle is given some form of driving signal (desired trajectory) from a vehicle controller. The corresponding force from the thruster is measured directly using the load cell. The unfiltered thrust is then fed into the virtual algorithm, and the vehicle motion is integrated according to the vehicle governing equation. In real time the control algorithm drives the virtual vehicle using the actual forces generated by the thruster within its test environment.

In order to demonstrate the accuracy of the LTI approximation the hybrid simulation must be tested for maneuvers with fundamentally different scaling. A quantity termed the "scale factor" was introduced to quantify the different maneuvering regimes. The scale factor is defined as $A^\star = \dfrac{A}{d}$, where A is the maneuvering amplitude, and d is the vehicle diameter (or characteristic size). The simulation was tested for three different maneuvering regimes, the *Cruising Regime*

(maneuver much larger than vehicle size, $A^\star = 3$), the *Docking Regime* (maneuver smaller than vehicle size, $A^\star = 0.5$), and the *Transition Regime* (the transition between other regimes, $A^\star = 1$). A more complete description of the vehicle model, as well as considerations for modeling different maneuvering regimes refer to Appendix C.

8.2 Frequency Response

Within the hybrid simulation the open loop frequency response was determined for the thruster vehicle system. This response was tested (over a maneuvering frequency range encompassing the -3 dB cutoff frequency) for all three maneuvering regime scale factors. The three response curves are shown in Figure 8.1. It should be noted here that the modeled response was calculated assuming a pulsation frequency sufficiently higher than the maneuvering frequencies tested in the simulation. For the *Cruising Regime* the model assumes a thruster frequency of $f_0 = 20Hz$, however, the thruster trim frequency could be set significantly lower for the other regimes and still maintain accuracy, due to the lower thrust requirements in general for those regimes. The modeled response was calculated for the other two regimes assuming a pulsation frequency of 9 and 5 Hz respectively.

It can be seen from this graph that the constant pulsation frequency approximation accurately models several features of the frequency response including the cutoff frequency and the convergence of different maneuvering regime response curves near the cutoff frequency. Another interesting feature is located in the low frequency maneuvers. Here the spread between the maneuvering regimes is more drastic than at the corner frequency of the system (which happens to be nearly identical for all three maneuvering regimes). This is indicative of the fact that at low maneuvering frequencies the thruster is required to deliver smaller forces, which in turn result in lower actuation frequencies, so that at this level the vehicle experiences individual pulsations. In the low amplitude *Docking regime* this results in a higher gain since pulsations enact an acceleration before drag forces take effect. In the *Transit regime* however, this results in less gain since the drag terms dominate in between pulsations. This trend is accurately captured by the approximated LTI model. Though

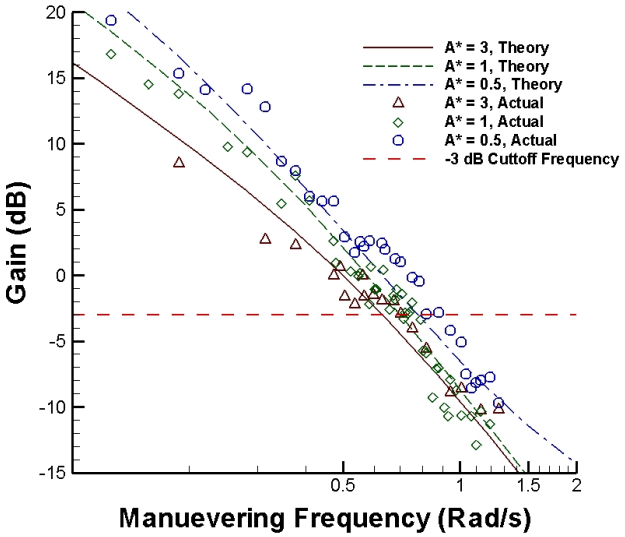

Figure 8.1: Open loop frequency response for the thruster vehicle system; *Cruising regime* shown by $A^\star = 3$, *Transition regime* shown by $A^\star = 1$, *Docking regime* shown by $A^\star = 0.5$. Theoretical response modeled assuming $f_0 = 20$, 9 and 5 Hz respectively

the simulation was not run for higher maneuvering frequencies, the model predicts that the vehicle in the *Cruising regime* will achieve a higher amplitude maneuver in the high frequency ranges, which is suggested by the slopes of the experimental trends.

8.3 Feedback Control

A simple proportional derivative (PD) feedback algorithm was then implemented in the hybrid simulation based off of the vehicle position error. The closed loop frequency response of the system under PD control is depicted in Figure 8.2. The important parameters which drive the controller gain selection are motivated by different goals for the different maneuvering regimes. The *Docking Regime* requires very accurate tracking with minimal overshoot; whereas the *Cruising Regime* is generally indifferent to overshoot and is much more concerned with a fast approach time (so that the vehicle can move to a site of interest before the phenomena of interest dissipates). For this study the feedback gain was set to 4 which was chosen to keep the required thrust within the thruster capacity; and the derivative gain ratio was set to 0.75 to keep the position overshoot within acceptable bounds in the *Docking regime*.

The system closed loop frequency response was determined over a similar frequency range for the same maneuvering scale factors as the open loop response. The pulsation frequency, f_0, for the linear model was set to the same driving frequencies as the open loop case. This model is seen to approximate the closed loop behavior of the thruster vehicle system sufficiently including the cutoff frequency. A key parameter of the model linearization which has not been discussed in detail is the trim velocity which is used to linearize the drag of the vehicle. This is one of the important parameters which differentiates between the different maneuvering regimes. In the *Docking regime*, the vehicle generally changes directions with a higher frequency and spends much of its time at low velocities. Therefore, selecting the trim velocity according to a maximum acceleration relation yields very good results, and is an appropriate approximation. By contrast the *Cruising regime* is characterized by long periods of sustained motion and the corresponding trim velocity should be set according to a velocity drag relation. Though the transfer function model for this regime

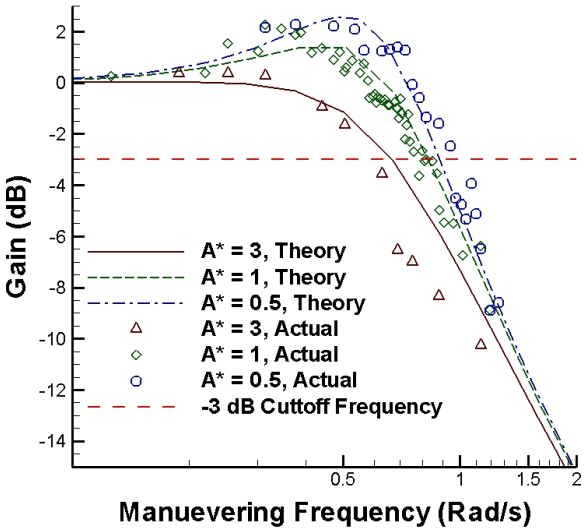

Figure 8.2: Closed loop frequency response for the thruster vehicle system. *Cruising regime* shown by $A^\star = 3$, *Transition regime* shown by $A^\star = 1$, *Docking regime* shown by $A^\star = 0.5$. Theoretical response modeled assuming $f_0 = 20$, 9 and 5 Hz respectively

comes close to approaching the actual cutoff seen in the system, it incorrectly predicts the gain on either side of the cutoff frequency. This is due to the fact that maneuvers in the cruising regime experience drastically variable drag forces, since the drag force is non-linear and the vehicle has a larger velocity range in the cruising regime. Because of these non-linearities and the sizable velocity range, the linearization about a single trim velocity predicts a drag which is too large in the low maneuvering frequencies, and similarly predicts a drag which is too low for high frequency maneuvers. Therefore, the accuracy of the drag approximation will decrease as the maneuvering scale increases. This implies that the large velocity range in the *Cruising regime*, requires a sliding model to accurately predict system frequency response (as opposed to the small scale maneuvers which are well approximated by a single trim velocity). Additionally the model has no limitation on thrust level, and in this regime drives the thruster beyond its actual capacity (even with relatively low gains). Though this is an un-modeled non-linear effect, it also addresses an interesting design consideration. This analysis demonstrates that any high accuracy thruster may not have a large enough range to be completely effective in the *Cruising regime*. The thruster could be designed with a larger output but this would reduce the accuracy of the system in the *Docking regime*. Fortunately, maneuvers in the high frequency *Cruising regime* are also generally coupled with significant forward vehicle velocity. This strong cross flow gives the thrusters an added dimensionality; instead of generating control forces strictly from the jetting momentum transfer, the VRT can be used to inject energy into the flow going over the vehicle, altering the effective shape of the vehicle seen by the surrounding flow. Furthermore, the effect of so called 'hydroshaping' increases with increased velocity where the thrust generation is observed to be lacking. Aeroshaping has been shown to be an effective technique in fighter jets, and general drag reduction [2]. Future studies will investigate the use of VRT's for the purpose of flow control. However, these studies are outside the scope of this investigation.

Chapter 9

Conclusions

9.1 Discussion

Unmanned vehicle networks are becoming an irreplaceable resource for in depth scientific testing in oceanic environments. Current vehicles are limited by an inability to provide simultaneous docking and transit capabilities. A new type of underwater jet thruster inspired by squid and jellyfish locomotion offers a possible solution to this problem since it offers faster tracking and lower overall vehicle drag than typical propeller thrusters, while maintaining the thrust capabilities at zero forward velocity. Another advantage of this type of thruster is that the desired level of thrust is reached much more quickly than typical propeller thrusters, and there is no lingering momentum transfer after the jet flow has been terminated, unlike tunnel thrusters. These advantages make this type of thruster ideal for high accuracy maneuvering applications.

There are several real world flows which involve non-parallel starting jets, but theoretical analysis has been largely focused on parallel starting jets; and specifically those created by a piston-cylinder vortex generator. It was demonstrated here that the 1D slug model, which is traditionally used to model impulse, circulation, and energy of all starting jets, under-predicts these quantities if the incoming flow has a converging radial velocity, and it is predicted that the 1D slug model will over-predict both quantities if there is a diverging radial velocity. Additionally, the 1D slug model provides a poor prediction of the impulse, circulation, and energy of low stroke ratio parallel starting jets, where the leading vortex ring has a strong influence on the incoming jet flow, as has been observed previously. Some studies have introduced correction factors to the slug model based

on nozzle configurations, but this doesn't address the source of the problem.

A new model was derived to predict impulse, circulation, energy, and pressure distribution of starting jets which specifically accounts for a radial velocity at the source of the jet flow. This model only requires the knowledge of jet kinematics at the entrance boundary of any axisymmetric control volume. This is a powerful tool for modeling jet flows and can even be extended to continuous jets by changing the treatment of farfield boundaries, but this will be examined in future publications. This formulation showed that 'overpressure' at the nozzle is impossible without any radial velocity at that boundary, induced or otherwise. We also presented generic axial and radial velocity profiles which can be used to parameterize a wide variety of actual jet flows, and the jet impulse and circulation were then derived in terms of the velocity profile parameters.

Both parallel and converging starting jets were created experimentally by ejecting fluid through a set of tube and orifice nozzles, and the velocity field of these jets was captured using DPIV techniques. The DPIV data was used to parameterize the velocity profiles at the exit of these nozzles, as well as to validate the control volume analysis. The velocity profiles of parallel jets expelled through a tube nozzle, and subsequently impulse and circulation of the jet, are highly sensitive to the formation of the primary vortex ring as indicated by the large variation in dynamics between high and low stroke ratios. Whereas, the orifice nozzle used to create a converging jet resulted in a much more uniform velocity profile throughout pulsation for any stroke ratio. The radial velocity at the entrance boundary has a drastic effect on both the circulation and impulse of the starting jet. The converging jet was observed to have as much as double the circulation and energy and 75% more impulse than the parallel jet with the same mass flux and nozzle diameter, and this increase was very well captured by the new jet model.

It should be noted that the parameters describing axial and radial velocity profiles are determined experimentally from the jet flows examined in this study, which makes these profiles more of an analytical tool than a predictive model. However, the consistency of some parameters allows them to actually be used in a predictive sense. The normalized slope of the radial profile and radial gradient profile $k_1^\star$ and $k_2^\star$ in particular show almost no variation with nozzle radius and piston ve-

locity for orifice nozzles, and seem to only depend on the stroke ratio for tube nozzles. Similarly the value of the axial shape parameters appears to be consistent for orifice nozzles since there is little change in axial velocity profile during formation. Though there is large variation in axial velocity in tube nozzle flows, these nozzles are avoided for vehicle maneuvering applications because of the increased drag associated with the tube jutting out the side of the hull. Therefore, this model is actually predictive for the type of thruster considered here under any operating condition, despite the parameterization based on specific jet flows.

The thruster was operated at high frequencies, as would be typical in vehicle applications, and the average thrust was modeled similar to the starting jets, making simple assumptions for the refilling period. It was observed that the model predicts the average thrust accurately for devices operating at frequencies below the cavitation frequency and stroke ratios below the formation number. When the frequency is very high, the formation and collapse of cavitation bubbles causes an undesired decrease in jetting volume, and when the stroke ratio is above the formation number interaction with the trailing wake substantially increases the negative impulse of refilling phase.

A model was derived to predict the formation number of the jet for any nozzle radius and jet velocity program, which is based on characteristic velocities at the axis of symmetry. The approximations developed to predict both vortex ring translational velocity and vortex ring velocity at the ring origin, may be used to predict these quantities in any vortex ring study provided that the circulation and impulse of the ring are known. The new velocity criterion was observed to accurately predict vortex ring pinch-off for the entire range of nozzle configurations, piston velocity programs, and nozzle radius programs tested in this study.

Using the new jet models a framework is presented which allows piston velocity program and nozzle radius to be optimized with respect to both maximum average thrust and maximum jetting efficiency, which is a quantity developed in this study that is similar to propulsive efficiency but does not require a knowledge of exact vehicle specifications. This analysis heavily focuses on the correct treatment of constraints on the velocity profile, and the differences between continuous jets and finite jets. The average thrust will be maximized by a constant piston velocity program at the

maximum attainable velocity, and the nozzle radius is set to a critical value where the vortex ring pinch-off occurs exactly when the flow is terminated. The jetting efficiency will be optimized by setting the nozzle radius to a minimum allowable value and expelling a jet with a slowly accelerating piston velocity which exactly matches a characteristic vortex ring velocity.

Additionally, a linear transfer function model was developed to approximate the transient dynamics of the thruster vehicle assembly. Vehicle maneuvers were characterized in three different maneuvering regimes based on this linearization; including the *Cruising, Docking* and *Transition regimes*. This transfer function model was seen to accurately predict the frequency response of the system (both open and closed loop), in regard to the cutoff frequency and general shape of the frequency response, even though it ignores certain high order dynamics, and again the thruster is seen to be ideally suited for small amplitude high accuracy maneuvers.

9.2 Future Work

9.2.1 Vortex Ring Centerline Velocity

The axial velocity distribution along the axis of symmetry a vortex ring was derived from stream function analysis in equation (5.14). This equation is valid for any vorticity distribution but the characteristic centerline velocity was approximated assuming a point vortex (zero core radius). Further analysis will be conducted to determine the centerline velocity considering the vortex distribution of the Norbury family of vortex rings. This characteristic velocity will then be a function of the total vortex ring circulation and impulse, like before, but will also have a dependence on the mean core of the vortex ring, ϵ. We predict this analysis will become necessary when formation number is delayed even more than the programs of the analysis here, and the mean core radius approaches that of hills spherical vortex $\epsilon = \sqrt{2}$.

9.2.2 Inclusion of Viscosity

The consistency of axial velocity profile for orifice nozzles allows the analysis of this study to be used as a predictive model for thrusters using these nozzles. However, pulsatile jet thrusters being used as a primary means of propulsion, rather than for maneuver, may be desired to use some form of tube nozzle. The modeling of this type of thruster would require an additional consideration, which is viscosity. The control volume analysis clearly requires that viscosity be ignored; however, the axial velocity profile at the exit of a tube nozzle is dependent on the viscosity and nozzle diameter. Since the axial shape parameter m, is inversely proportional to the thickness of the shear layer, this value could be approximated in tube nozzle flows from the fluid viscosity tube diameter, and formation time, making the model predictive.

Chapter 10

Resulting Publications

Journal Articles

[PubsJ1] M. Krieg, P. Klein, R. Hodgkinson, and K. Mohseni. A hybrid class underwater vehicle: bioinspired propulsion, embedded system, and acoustic communication and localization system. Marine Technology Society Journal: Special Edition on Biomimetics and Marine Technology, 45(4):153 – 164, 2011.

[PubsJ2] M. Krieg and K. Mohseni. Thrust characterization of pulsatile vortex ring generators for locomotion of underwater robots. IEEE J. Oceanic Engineering, 33(2):123–132, 2008.

[PubsJ3] M. Krieg and K. Mohseni. Dynamic modeling and control of biologically inspired vortex ring thrusters for underwater robot locomotion. IEEE Trans. on Robotics, 26(3):542–554, 2010.

[PubsJ4] M. Krieg and K. Mohseni. Modelling circulation, impulse, and kinetic energy of starting jets with non-zero radial velocity. J. Fluid Mech., Under Review, 2012.

[PubsJ5] M. Krieg and K. Mohseni. A new kinematic criterion for vortex ring pinch-off. Physics of fluids, Under Review, 2012.

[PubsJ6] M. Krieg and K. Mohseni. New perspectives on collagen fibers in the squid mantle. Journal of Morphology, DOI: 10.1002/jmor.20003, 2012.

../RefA1,../RefA1b

Refereed Conference Papers

[PubsC1] M. Krieg, C. Coley, C. Hart, and K. Mohseni. Synthetic jet thrust optimization for application in underwater vehicles. In Proceedings of the 14^th International Symposium on Unmanned Untethered Submersible Technology (UUST), Durham, New Hampshire,, August 21 - 24 2005.

[PubsC2] M. Krieg and K. Mohseni. Developing a transient model for squid inspired thrusters, and incorporation into control design. In Proceedings of the International Conference on Intelligent Robots and Systems (IROS 08), Nice, France, September 22-26 2008.

[PubsC3] M. Krieg and K. Mohseni. Incorporation of novel underwater thrusters into vehicle control systems. In Proceedings of the IEEE International Conference on Robotics and Automation, Pasadena, CA, May 19-23 2008.

[PubsC4] M. Krieg and K. Mohseni. Dynamic control of biologically inspired pulsatile jet propulsion thrusters. In 28th International Conference on Ocean, Offshore, and Arctic Engineering, Honolulu, HI, June 2009.

[PubsC5] M. Krieg and K. Mohseni. Dynamic thrust optimization of flow actuators inspired by squid and jellyfish locomotion. In **(Submitted)** 51st IEEE Conference on Decision and Control, Maui, HI, December 2012 2012.

[PubsC6] M. Krieg and K. Mohseni. Enhanced impulse of a jet thruster due to radial velocity at the nozzle. In 50th AIAA Sciences meeting including the New Horizons forum and Aerospace Exhibition, Nashville ,TN, Jan 2012.

[PubsC7] M. Krieg and K. Mohseni. Thrust enhancement from radial velocity in squid inspired thrusters. In 31st International Conference on Ocean, Offshore, and Arctic Engineering, Rio de Janeiro, Brazil, July 2012.

[PubsC8] M. Krieg, A. Pitty, M. Salehi, and K. Mohseni. Optimal thrust characteristics of a synthetic jet actuator for application in low speed maneuvering of underwater vehicles. In Proceedings of the OCEANS 2005, Washington, D.C., September 19-23 2005. MTS/IEEE.

Non-Ref Conference Papers, Talks, and Co-Authored Papers

[PubsT1] T. Clark, M. Krieg, and K. Mohseni. Flow visualization for pulsatile vortex ring thrusters. Technical Report IMECE2008-68030, ASME International Mechanical Engineering Congress & Exhibition, Boston, Massachusetts, October 31 - November 6 2008.

[PubsT2] M.W. Krieg, T. Clark, and K. Mohseni. Thrust optimization in pulsatile vortex generators in liquid medium. In Bulletin of the American Physical Society; 59th Annual Meeting of the Fluid Dynamics Division, page 146. American Physical Society, 2006.

[PubsT3] T. Thomas, M. Krieg, and K. Mohseni. Thrust characterization for bio-inspired pulsatile vortex ring thrusters with variable exit nozzle diameter. Buena Vista, FL, 13-19 November 2009. ASME International Mechanical Engineering Congress and Exposition.

Bibliography

[1] D. G. Akhmetov. Vortex Rings. Springer, Berlin, Heidelberg, 2009.

[2] M. Amitay, D. R. Smith, V. Kibens, D.E. Parekh, and A. Glezer. Aerodynamic flow control over an unconventional airfoil using synthetic jet actuators. AIAA Journal, 39(3):361–370, 2001.

[3] E.J. Anderson and E. DeMont. The mechanics of locomotion in the squid *loligo pealei*: Locomotory function and unsteady hydrodynamics of the jet and intramantle pressure. J. Exp. Biol., 203:2851–2863, 2000.

[4] E.J. Anderson and M.A. Grosenbaugh. Jet flow in steadily swimming adult squid. J. Exp. Biol., 208:1125–1146, 2005.

[5] D.S. Barrett, M.S. Triantafyllou, D.K.P. Yue, M.A. Grosenbaugh, and M. Wolfgang. Drag reduction in fish-like locomotion. J. Fluid Mech, 392:183–212, 1999.

[6] I.K. Bartol, P.S. Krueger, W.J. Stewart, and J.T. Thompson. Hydrodynamics of pulsed jetting in juvenile and adult brief squid *L*olliguncula brevis: evidence of multiple jet 'modes' and their implications for propulsive efficiency. Journal of Experimental Biology, pages 1189–1903, 2009. doi:10.1093/icb/icn043.

[7] I.K. Bartol, P.S. Krueger, J.T. Thompson, and W.J. Stewart. Swimming dynamics and propulsive efficiency of squids throughout ontogeny. Integrative and Comparative Biology, pages 1–14, 2008. doi:10.1093/icb/icn043.

[8] I.K. Bartol, M.R. Patterson, and R. Mann. Swimming mechanics and behavior of the shallow-water brief squid *lolliguncula brevis*. J Exp Biol, 204:3655–3682, 2001.

[9] G.K. Batchelor. An Introduction to Fluid Mechanics. Cambridge University Press, Cambridge, 1967.

[10] T.B. Benjamin. The alliance of practical and analytical insights into the nonlinear problems of fluid mechanics. In Applications of Methods of Functional Analysis to Problems in Mechanics, volume 503, pages 8–29. Springer-Verlag, 1976.

[11] Q. Bone, A. Pulsford, and A. D. Chubb. Squid mantle muscle. Journal of Mar. Biol. Assoc., 61:327–342, 1981.

[12] B.J. Cantwell. Viscous starting jets. J. Fluid Mech, 173:159–189, 1986.

[13] R.B. Clark and J.B. Cowey. Factors controlling the shape of certain nemertean and turbellarian worms. J Exp. Biol., 35:731–748, 1958.

[14] I. Cohen and P. Kundu. Fluid Mechanics. Academic Press, New York, 2007.

[15] J. O. Dabiri, S. P. Colin, K. Katija, and J. H. Costello. A wake based correlate of swimming performance and foraging behavior in seven co-occurring jellyfish species. J. Exp. Biol., 213:1217–1275, 2010.

[16] J.O. Dabiri and M. Gharib. Fluid entrainment by isolated vortex rings. J. Fluid Mech, 511(4):311–331, 2004.

[17] J.O. Dabiri and M. Gharib. Starting flow through nozzles with temporally variable exit diameter. J. Fluid Mech, 538:111–136, 2005.

[18] N. Didden. On the formation of vortex rings: Rolling-up and production of circulation. Z. Angew. Mech. Phys., 30:101–116, 1979.

[19] M. Dunbabin, J. Roberts, K. Usher, G. Winstanley, and P. Corke. A hybrid auv design for shallow water reef navigation. In Proceedings of the IEEE International Conference on Robotics and Automation, pages 2105–2110, Barcelona, Spain, April 2005.

[20] T. I. Fossen. Nonlinear modelling and control of underwater vehicles. PhD thesis, Norwegian Institute of Technology, Trondheim, Norway, 1991.

[21] L.E. Fraenkel. On steady vortex rings of small cross-section in an ideal fluid. Proc. R. Soc. Lond., 316:29–62, 1970.

[22] L.E. Fraenkel. Examples of steady vortex rings of small cross-section in an ideal fluid. J. Fluid Mech., 51(1):119–135, 1972.

[23] M. Gharib, E. Rambod, and K. Shariff. A universal time scale for vortex ring formation. J. Fluid Mech, 360:121–140, 1998.

[24] W.F. Gilly, B. Hopkins, and G.O. Mackie. Development of giant motor axons and neural control of escape responses in squid embryos and hatchlings. Biol Bull, 180:209–220, 1991.

[25] A. Glezer. The formation of vortex rings. Phys. Fluids, 31(12):3532–3542, 1988.

[26] J.M. Gosline and R.E. Shadwick. The role of elastic energy-storage mechanisms in swimming - an analysis of mantle elasticity in escape jetting in the squid Loligo-Opalescens. Canadian Journal of Zoology, 61:1421–1431, 1983.

[27] J.M. Gosline and R.E. Shadwick. The Molluska, volume 1, chapter Molluscan collagen and its mechanical organization in squid mantle (8). Academic Press, New York, New York, 1985.

[28] J.M. Gosline, J.D. Steeves, A.D. Harman, and M.E. Demont. Patterns of circular and radial mantle muscle-activity in respiration and jetting of the squid *loligo-opalescens*. J Exp Biol, 104:97–109, 1983.

[29] I. S. Gradshteyn and I. M. Ryzhik. Table of integrals, series, and products. Academic Press, San Diego, CA, 2000.

[30] J.E. Harris and H.D Crofton. Structure and function in the nematodes: internal pressure and cuticular structure in *ascaris*. J Exp. Biol., 34:116–130, 1957.

[31] R Holman, Y Utturkar, R Mittal, BL Smith, and L Cattafesta. Formation criterion for synthetic jets. AIAA Journal, 43(10):2110–2116, OCT 2005.

[32] Lord Kelvin. The translatory velocity of a circular vortex ring. Phil. Mag., 4:511–512, 1867.

[33] Lord Kelvin. Mathematical and Physical Papers, volume IV. Cambridge University Press, Cambridge, UK, 1910.

[34] M. Krieg and K. Mohseni. Thrust characterization of pulsatile vortex ring generators for locomotion of underwater robots. IEEE J. Oceanic Engineering, 33(2):123–132, 2008.

[35] M. Krieg and K. Mohseni. Dynamic modeling and control of biologically inspired vortex ring thrusters for underwater robot locomotion. IEEE Trans. on Robotics, 26(3):542–554, 2010.

[36] M. Krieg and K. Mohseni. Dynamic thrust optimization of flow actuators inspired by squid and jellyfish locomotion. In **(Submitted)** 51st IEEE Conference on Decision and Control, Maui, HI, December 2012 2012.

[37] M. Krieg and K. Mohseni. Modelling circulation, impulse, and kinetic energy of starting jets with non-zero radial velocity. J. Fluid Mech., Under Review, 2012.

[38] P. Krueger, J. Dabiri, and M. Gharib. The formation number of vortex rings formed in a uniform background co-flow. Journal of Fluid Mechanics, 556(1):147–166, 2006.

[39] P.S. Krueger. An over-pressure correction to the slug model for vortex ring circulation. J. Fluid Mech, 545:427–443, 2005.

[40] P.S. Krueger and M. Gharib. The significance of vortex ring formation to the impulse and thrust of a starting jet. Phys. Fluids, 15(5):1271–1281, 2003.

[41] P.S. Krueger and M. Gharib. Thrust augmentation and vortex ring evolution in a fully pulsed jet. AIAA J., 43(4):792–801, 2005.

[42] H. Lamb. Hydrodynamics. Dover, New York, 1945.

[43] S. Licht. Biomimetic oscillating foil propulsion to enhance underwater vehicle agility and maneuverablity. PhD thesis, Massachusetts Institute of Technology, Cambridge, Massachusetts, 2008.

[44] S. Licht, V. Polidoro, M. Flores, F.S. Hover, and M.S. Triantafyllou. Design and projected performance of a flapping foil AUV. IEEE Journal of Ocean Engineering, 29(3):786–68, 2004.

[45] T.T. Lim and T.B. Nickels. Vortex rings. In Sheldon I. Green, editor, Fluid Vortices. Kluwer Academic Publishers, 1995.

[46] D. Lipinski and K. Mohseni. Flow structures and fluid transport for the hydromedusa sarsia tubulosa. AIAA paper 2009-3974, 39th AIAA Fluid Dynamics Conference, San Antonio, Texas, June 22-25 2009.

[47] D. Lipinski and K. Mohseni. A numerical investigation of flow structures and fluid transport with applications to feeding for the hydromedusae Aequorea victoria and Sarsia tubulosa. J. Exp. Biology, 212:2436–2447, 2009.

[48] P. Macgillivray, E. J. Anderson, G. M. Wright, and M. E. DeMont. Structure and mechanics of the squid mantle. The Journal of Experimental Biology, 202:683–695, 1999.

[49] J. S. Marshall. Inviscid Incompressible Flow, chapter 13, pages 260–292. Wiley, New York, 2001.

[50] T. Maxworthy. The structure and stability of vortex rings. J. Fluid Mech., 51(1):15–32, 1972.

[51] T. Maxworthy. Some experimental studies of vortex rings. J. Fluid Mech, 80:465–495, 1977.

[52] M.B. Mclean. Dynamic performance of small diameter tunnel thrusters. PhD thesis, Naval Postgraduate School, Monterey, California, 1991.

[53] K. Mohseni. Statistical equilibrium theory of axisymmetric flows: Kelvin's variational principle and an explanation for the vortex ring pinch-off process. Phys. Fluids, 13(7):1924–1931, 2001.

[54] K. Mohseni. Mixing and impulse extremization in microscale vortex formation. In Proceedings of the Fifth International Conference on Modeling and Simulation of Microsystems, San Juan, Puerto Rico, April 2002.

[55] K. Mohseni. A formulation for calculating the translational velocity of a vortex ring or pair. Bioinspiration & Biomimetics, 1:S57–S64, 2006.

[56] K. Mohseni and M. Gharib. A model for universal time scale of vortex ring formation. Phys. Fluids, 10(10):2436–2438, 1998.

[57] K. Mohseni, H. Ran, and T. Colonius. Numerical experiments on vortex ring formation. J. Fluid Mech, 430:267–282, 2001.

[58] M. Nitsche and R. Krasny. A numerical study of vortex ring formation at the edge of a circular tube. J. Fluid Mech., 276:139–161, 1994.

[59] J. Norbury. A steady vortex ring close to hill's spherical vortex. Proceedings of the Cambridge Philosophical society, 72:253, 1972.

[60] J. Norbury. A family of steady vortex rings. J. Fluid Mech, 57(3):417–431, 1973.

[61] R.K. O'Dor and D.M. Webber. Invertebrate athletes: Trade-offs between transport efficiency and power density in cephalopod evolution. Journal of Experimental Biology, 160:93–112, 1991.

[62] A.B. Olcay and P.S. Krueger. Measurement of ambient fluid entrainment during laminar vortex ring formation. Experiments in Fluids, 44(2):235–247, 2008.

[63] A Packard and E. R. Trueman. Muscular activity of the mantle of *Sepia Loligo* (cephalopoda) during respiratory movements and jetting, and its physiological interpretation. Journal of Experimental Biology, 61:411–419, 1974.

[64] W.J. Pierson and L.A. Moskowitz. Proposed spectral form for fully developed wind seas based on the similarity theory of s. a. kitaigorodskii. Journal of Geophysical Research, 69(3):5181–5190, 1964.

[65] W. D. Pilkey and O. H. Pilkey. Mechanics of Solids, chapter Stess and Strain (4), page 292. QPI. Quantum Publishers, New York, 1974.

[66] T.Z. Preuss, N. Lebaric, and W.F. Gilly. Post-hatchling development of circular mantle muscles in the squid *loligo opalescens*. Biol Bull, 192:375–387, 1997.

[67] D. I. Pullin. The large-scale structure of unsteady self-similar rolled-up vortex sheets. J. Fluid Mech., 88(3):401–430, 1978.

[68] D. I. Pullin and W. R. C. Phillips. On a generalization of kaden's problem. J. Fluid Mech., 104:45–53, 1981.

[69] D.I. Pullin. Vortex ring formation in tube and orifice openings. Phys. Fluids, 22:401–403, 1979.

[70] M. Raffel, C. E. Willert, and J. Kompenhans. Particle Image Velocimetry. Springer, Heidelberg, NY, 1998.

[71] R. Raju, R. Mittal, Q. Gallas, and L. Cattafesta. Scaling of vorticity flux and entrance length effects in zero-net mass-flux devices. In AIAA 35th Fluid Dynamics Conference and Exhibit, Toronto, Ontario, 6-9 June 2005.

[72] W. C. Reynolds, D. E. Parekh, P. J. D. Juvet, and M. J. D. Lee. Bifurcating and blooming jets. Annu. Rev. Fluid Mech, 35:295–315, 2003.

[73] E. G. Richardson and E. Tyler. The transverse velocity gradients near the mouth of a pipe in which an alternating or continuous flow of air is established. Proc. Phys. Soc. London, 42:1–15, 1929.

[74] B. J. Rigby, N. Hirai, J. D. Spikes, and H. Eyring. The mechanical properties of rat tail tendon. Journal of General Physiology, 43:265–283, 1959.

[75] P.H. Robert. A Hamiltonian theory for weakly interacting vortices. Mathematika, 19:169–179, 1972.

[76] P.H. Robert and R.J. Donnelly. Dynamics of vortex rings. Physics Letters, 31(3):137–138, 1970.

[77] M. Rosenfeld, K Katija, and J. O. Dabiri. Circulation generation and vortex ring formation by conic nozzles. Journal of Fluids Engineering, 131:091204:1–8, 2009.

[78] M. Rosenfeld, E. Rambod, and M. Gharib. Circulation and formation number of laminar vortex rings. J. Fluid Mech, 376:297–318, 1998.

[79] P. G. Saffman. The number of waves on unstable vortex rings. J. Fluid Mech., 84(4):625–639, 1978.

[80] P.G. Saffman. Vortex Dynamics. Cambridge University Press, Cambridge, 1992.

[81] M. Sahin and K. Mohseni. The numerical simulation of flow patterns generated by the hydromedusa aequorea victoria using an arbitrary Lagrangian-Eulerian formulation. AIAA paper 2008-3715, 38$^{\text{th}}$ AIAA Fluid Dynamics Conference and Exhibit, Seattle, OR, June 23-26 2008.

[82] M. Sahin and K. Mohseni. An arbitrary Lagrangian-Eulerian formulation for the numerical simulation of flow patterns generated by the hydromedusa Aequorea victoria. J. Comp. Phys., 228:4588–4605, 2009.

[83] M. Sahin, K. Mohseni, and S. Colins. The numerical comparison of flow patterns and propulsive performances for the hydromedusae Sarsia tubulosa and Aequorea victoria. J. Exp. Biology, 212:2656–2667, 2009.

[84] K. Shariff and A. Leonard. Vortex rings. Ann. Rev. Fluid Mech., 34:235–279, 1992.

[85] M. Shusser and M. Gharib. A new model for inviscid vortex ring formation. In AIAA 30th Fluid Dynamics Conference, Norfolk, 28 June - 1 July 1999.

[86] M. Shusser and M. Gharib. Energy and velocity of a forming vortex ring. Phys. Fluids, 12(3):618–621, 2000.

[87] J. Thompson and W. Kier. Ontogenetic changes in fibrous connective tissue organization in the oval squid, *sepioteuthis lessoniana* lesson, 1830. Biology Bulletin, 201:136–153, 2001.

[88] J. T. Thompson and W. M. Kier. Ontogenetic changes in mantle kinematics during escape-jet locomotion in the oval squid, Sepioteuthis lessoniana lesson, 1830. Biol. Bull., 201:154–166, 2001.

[89] K.A. Torsiello. Acoustic positioning of the NPS autonomous underwater vehicle (AUV II) during hover conditions. Master's thesis, Naval Postgraduate School, Monterey, California, USA, Mar. 1994.

[90] E.R. Trueman. Motor performance of some cephalopods. Journal of Experimental Biology, 49:495–505, 1968.

[91] Y. Vargas, T. Finley, K. Mohseni, and J. Hertzberg. Flow characterization of a synthetic jet. AIAA paper 2006-1422, 44^{th} AIAA Aerospace Sciences Meeting and Exhibit, Reno, Nevada, January 9-12 2006.

[92] A. Viidik. Simultaneous mechanical and light microscopic studies of collagen fibers. Z. Anat., 136:204–212, December 1972.

[93] S. Vogel. Comparative biomechanics: Life's physical world. Princeton University Press, Princeton, NJ, 2003.

[94] S.A. Wainwright, W.D. Biggs, J.D. Currey, and J.M. Gosline. Mechanical design in organisms. Edward Arnold, London, England, 1976.

[95] D. V. Ward and S. A. Wainwright. Locomotory aspects of squid mantle structure. J. of Zoology, 167:437–449, 1972.

[96] C. E. Willert and M. Gharib. Digital particle image velocimetry. Experiments in Fluids, 10:181–193, 1991.

[97] M. Wilson, J. Peng, J.O. Dabiri, and J.D. Eldredge. Lagrangian coherent structures in low reynolds number swimming. J. Physics: Condensed Matter, 21:204105, 2009.

[98] D. Yoerger, J. Cooke, and J.-J. Slotine. The influence of thruster dynamics on underwater vehicle behavior and their incorporation into control system design. IEEE Journal of Oceanic Engineering, 15(3):167–178, 1990.

[99] J. Z. Young. The functioning of the giant nerve fibres of the squid. Journal of Experimental Biology, 15:170–185, 1938.

Appendix A

Vortex Ring Reynolds Number Dependency

The Reynolds number of the jet describes the relative significance of viscous damping forces to inertial forces; and is closely related to the transition into turbulent flow regimes. The jet Reynolds number can be computed in terms of the initial circulation Γ_0 defined as [25],

$$Re_\Gamma = 2\frac{\Gamma_0}{\nu} \ . \tag{A.1}$$

It was determined that jets created from fluid at rest will roll into laminar vortex rings if the Reynolds number is less than a critical Reynolds number which is dependent on the stroke ratio of the jet. For a jet with a stroke ratio of 2.3 the critical Reynolds number at which the vortex ring becomes turbulent is 25000 [25].

To analyze the nature of the jet a cross section of the flow extruding from the thruster was photographed using a laser induced fluorescein (LIF) technique. A laser sheet was used to illuminate the vortex ring cross section shown in Figure A.1. According to the formulation of the Reynolds number in terms of the initial circulation, every pulse of the thruster at the operational parameters used in capturing the images in Figure A.1 produces a ring with an identical Reynolds number of 9408. The first ejected vortex ring is clearly seen to be a laminar one. This ring is created from a laminar jet extruding from the orifice (Figure A.1(a)). For this ring the Glezer criteria for the laminarity of the vortex ring is clearly satisfied. It should be noted that all of the vortex rings studied in [25] were started from laminar jets, whereby fluid at rest in a cylinder was ejected by a sliding piston which was reset and brought to rest before subsequent testing. The jet only evolved

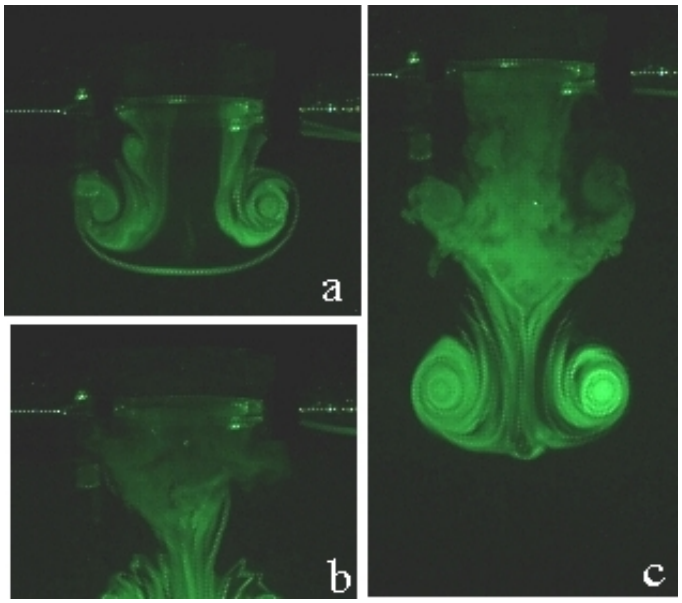

Figure A.1: Cross section of the flow emanating from thruster operating with stroke ratio of 2.3 and $f = 7$ Hz. A reflective dye is illuminated with a laser sheet through the center of the vortex ring. The initial ring with a laminar starting jet is shown in (a), the secondary turbulent pulsatile jet is shown in (b), and both fully evolved vortex rings are shown in (c).

into a turbulent ring if a critical Reynolds number criterion was met. The second ring ejected from our thruster, by contrast, started from a turbulent jet, and evolved into a turbulent ring. Even though the Re_Γ for both rings is identical for both cases, $Re_\Gamma = 9408$, the second ring is clearly turbulent due to the fact that it is generated from a turbulent jet (the jet is initially turbulent since it is comprised of fluid which was recently ingested into the cavity). The inherent disturbances in the cycling fluid motion into the cavity causes pulsatile jets to be much more prone to turbulence than starting jets, an idea reflected in the higher spreading rate of a pulsatile jet as compared with a steady jet[1] . Therefore, in all of the high frequency experiments conducted in this investigation the jet emanating from the orifice is primarily turbulent.

[1] For experimental measurement and analytical modeling of micro synthetic jets in air see [91]

Appendix B

Piston Velocity Validation

The jet piston velocity, u_p, is determined from motor encoder velocity, assuming that the plunger has a linear corespondence between deflection and volume displacement. The displaced volume was measured at several plunger deflections to test this relationship. However, this testing used static volume measurement techniques and further validation was needed to ensure that this relationship is preserved during high speed operation, especially considering that the plunger is constructed with a flexible rubber which might have load dependent deformation characteristics.

Fortunately, one of the tube nozzles used during experimentation is constructed out of clear acrylic which allowed visual access to the internal flow. Therefore, filming the internal flow just required repositioning the camera slightly higher in the visualization setup (see Section 3.3). A sample image of the clear tube nozzle with illuminated internal flow is depicted in Figure B.1.

A typical driving signal was sent to the thruster, which was to quickly ramp up to then maintain a constant piston velocity, around 7 cm/s. The internal tube flow was filmed and processed using the commercial DPIV algorithms (see Section 3.4). The velocity profile across the nozzle area was determined at multiple locations. Though the nozzle itself is a cylindrical plastic tube, the optical density of acrylic is close enough to water that the optical distortion will be minimized, and no corrections were made to the velocity field determined in the tube. The velocity profile accross the nozzle was also observed to be nearly uniform except at the nozzle surface at later stages of pulsation accounting for boundary layer development. The volume flux, Ω, was calculated

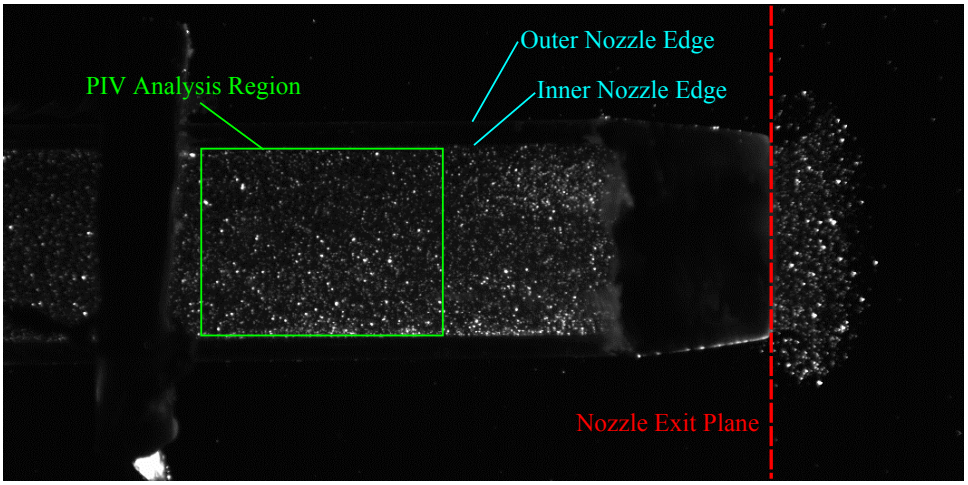

Figure B.1: A single frame depicting the flow visualization used to calibrate piston velocity. Seeding particles are illuminated by a laser sheet entering from the nozzle opening.

by integrating the DPIV velocity profile over the nozzle area,

$$\Omega = 2\pi \int_0^R ur\, dr \ . \tag{B.1}$$

Next the piston velocity is determined from the volume flux in the usual way, $u_p = \Omega/\pi R^2$. The piston velocity was also determined from the motor encoder data for the same trial run. The piston velocity determined from each method is plotted as a function of time in Figure B.2.

For the majority of the pulsation cycle the piston velocity determined from DPIV matches the piston velocity determined by the encoder validating the encoder piston velocity, with the exception of the end of pulsation where the sudden termination of plunger motion results in some oscillation of the piston velocity associated with elastic vibrations in the plunger surface.

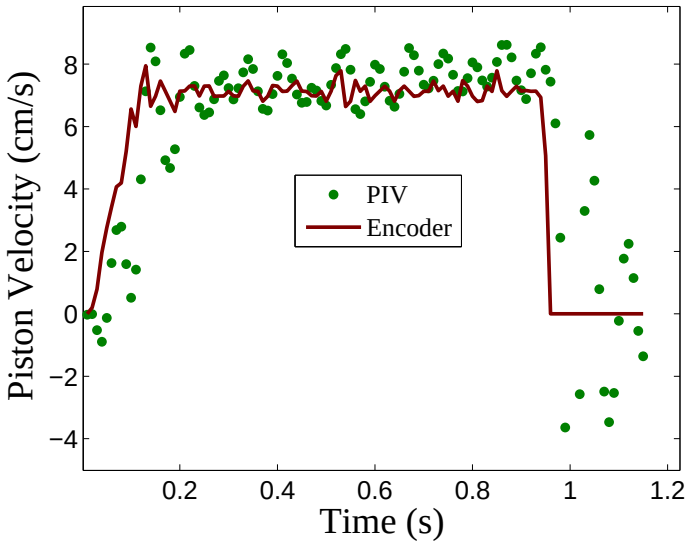

Figure B.2: Piston velocity is shown vs. time, values determined from encoder data are shown by the solid red line and values determined from DPIV measurements are shown with a green point marker

Appendix C

LTI Vehicle Modeling and Thruster Implementation

C.1 Vehicle Model

Consider a simple underwater vehicle to be modeled by a cylinder in a fluid with a single degree of freedom. The governing equation for the system is given by the simple drag equation

$$M\ddot{x} = T - C_d\dot{x}_r|\dot{x}_r| \tag{C.1}$$

here, x is the unrestrained axis, M is the mass of the vehicle (including an added mass), T is the instantaneous force provided by the thruster, $\dot{x_r}$ is the relative vehicle velocity $\dot{x_r} = \dot{x} + u_{\text{fluid}}$, and C_d is a drag coefficient defined by $C_d = \frac{1}{2}\rho S C_D(Re)$, S is the wetted area of the vehicle and $C_D(Re)$ is the coefficient of drag of a cylinder in a laminar cross flow, which seems like a fair assumption since the primary uses of these thrusters are for maneuvers involving rotation and sideways translation at low speeds, both of which induce a laminar cylinder cross flow. Without loss of generality the relative velocity will be considered equal to the inertial velocity (i.e. $u_{\text{fluid}} = 0$). If the nonlinear drag term is linearized about some nominal trim velocity $\dot{x}_{\text{trim}}$ then the governing equation of the vehicle can be modeled by a plant in the spectral domain with the following form,

$$G_{\text{sub}}(s) = \frac{1}{ms^2 + Cs}, \text{ and } C = \frac{1}{2}\rho S C_D(Re)\dot{x}_{\text{trim}}, \tag{C.2}$$

where the input is the transient thrust of the thruster, and the output is the position of the vehicle along the x axis.

C.2 Maneuver Scaling and Trim Conditions

The ultimate goal of this type of maneuvering technology is to achieve a high accuracy loiter or hover, so that the vehicle can engage some docking mechanism and perform autonomous upkeep. Marine environments are cluttered with wave like current disturbances. To overcome these disturbances a vehicle must provide a wide range of controlling forces. It becomes apparent that the performance of a controller in this type of an environment can be most usefully characterized by a frequency analysis. Whereby, the inputs to the system are sinusoidal maneuvers of the form

$$x_d = A \sin(\omega t) \tag{C.3}$$

with x_d being the desired vehicle position, A is the maneuvering amplitude, and ω the maneuvering frequency.

It should be noted that the model developed for the thruster vehicle system was derived using several approximations and linearizations. The actual dynamics of the system are highly non-linear, so that the choice of design points to linearize about has a strong effect on the predicted dynamics of the system. Therefore, the selection of these design points deserves careful consideration. Typically these parameters would be defined in terms of actual vehicle requirements, but we would like to extend a more general analysis. That is to define optimal vehicle parameters with respect to maneuvering capabilities, and maneuvering parameters.

Consider again that the drag model assumes the vehicle to be a perfect cylinder in cross flow. The characteristic size of a cylinder in this flow is the diameter. If all vehicles are assumed to have the same aspect ratio (which we will denote σ), then the geometry is reduced to the diameter d. The relative size of a maneuver plays a large role in determining the dynamics of the vehicle performing that maneuver. This quality can be characterized by the ratio of maneuver amplitude to the vehicle characteristic length $A^\star = \frac{A}{d}$, which will be referred to as the scale factor of the maneuver. If we characterize maneuvers according to their scale factor, then maneuvers can be thought of as members three regimes. Maneuvers in the *Cruising regime* are characterized by maneuvers much larger than the vehicle sizing, and maneuvers in the *Docking regime* are characterized by maneuvers

much smaller than the vehicle characteristic sizing. Maneuvers with amplitudes on the same order as the vehicle sizing are in the *Transition regime*, which is required to transition between the cruising and docking modes.

C.3 Scaling the problem for unitary amplitude

This section describes a method for scaling the vehicle control problem so that maneuvers in different regimes can be analyzed using consistent nomenclature as in the frequency response analysis. It is convenient from a frequency analysis point of view, to scale the problem so that the maneuvering amplitude attains unity (A = 1). Through this mapping a maneuver with a smaller amplitude may be modeled by a larger vehicle with unitary amplitude. The geometric scaling is fairly straightforward. The vehicle diameter can be recast as $d = 1/A^\star$, and assuming that the vehicle is designed to approach neutral buoyancy the mass of the vehicle becomes $M = \rho\pi/A^{\star 3}$. In order to maintain consistency, the thruster response must be scaled appropriately to incorporate the larger vehicle. The limitation on the thruster is the maximum thrust it can produce while still being accurately described by the slug model; which in the vehicle model shows up as a maximum voltage that can be applied to the motor controller $V_{\max}$. If a thruster bounded by maximum thrust $C_v \left(V_{\max} K_{MC}\right)^2$ is operating on a vehicle of mass $M(A^\star)$, the maximum acceleration it can attain can be derived from Newton's second law (assuming the vehicle is at rest and being forced with the maximum thrust). This maximum acceleration will be considered the design criterion for vehicle thruster selection. Consider a thruster (characterized by K_{MC_0}) which is selected for a vehicle of characteristic size d_0. The criterion on the thrust capacity requires that the system's maximum acceleration is equal to the maximum required maneuvering acceleration (given $A^\star = 1$). Some algebra gives a natural maneuvering frequency where this design constraint holds true

$$\omega_0 = \left(\frac{C_v}{\rho\pi}\right)^{\frac{1}{4}} \left(\frac{K_{MC_0} V_m ax}{\omega_0}\right)^{\frac{1}{2}}. \tag{C.4}$$

Additionally as the maneuvering regime changes the maximum acceleration required by the desired maneuver increases proportionally to the scale factor ($\ddot{x}_{d,max} = A^\star \ddot{x}_{max}$). This is the condition

that will be enforced to ensure a consistent thruster scaling.

Now consider the scaled vehicle which ensures unitary amplitude whose diameter and mass are purely a function of the scale factor. The maximum acceleration of this vehicle can similarly be defined in terms of the scaled unknown thruster gain $K_{MC}(A^\star)$. Furthermore, the maximum acceleration of the desired maneuver will always be the square of the maneuvering frequency (since it has unitary amplitude). If the maneuvering amplitude is set equal to the natural maneuvering frequency of the actual thruster vehicle system, and the relation between accelerations is enforced then the scaled thruster gain can be solved as a function of the natural vehicle parameters and the scale factor,

$$K_{MC}(A^\star) = K_{MC_0} \frac{1}{A^{\star 2} d_0^2}. \tag{C.5}$$

If we define a natural scale factor for the system as, $A_0^\star = \frac{1}{d_0}$, then the equation for the scaled motor gain takes on a much more aesthetic form given by

$$K_{MC}(A^\star) = K_{MC_0} \left(\frac{A_0^\star}{A^\star} \right)^2. \tag{C.6}$$

Similarly the drag normalization velocity can be rescaled in terms of the maneuvering regime parameter which results in a new coefficient term in the vehicle model (C.2)

$$C = \frac{K_{MC} V_{\text{trim}}}{A^\star} \sqrt{\frac{\rho C_D C_v \sigma}{2}}, \tag{C.7}$$

where V_{trim} is a trim voltage which should be somewhere in the middle of the range of possible controller signal voltages correlating to the voltage required to attain the trim velocity. Therefore a maneuver defined by a given scale factor, being performed by a vehicle with specific parameters can be similarly analyzed by a unitary maneuver being performed by a scaled equivalent vehicle, whose thruster strength is characterized by (C.6), and whose drag is characterized by (C.7).

Appendix D

New Perspectives on Squid Collagen Fibers

D.1 Introduction

Squid Mantle

The powerful squid mantle primarily consists of muscle packed between two helically wound collagenous tunics which are oriented at an angle of approximately $27^\circ \pm 1^\circ$ to the longitudinal axis of the squid, for *Lolligoguncula brevis* [95]. The arrangement of a single layer of collagen fibers in the tunic and a definition of the tunic fiber angle, θ, are shown in Figure D.1. Circumferential muscles ring the mantle and radial muscles run from the inner tunic to the outer tunic Figure D.2. The robust nature of the collagen fibers in the tunic, their inelastic properties, and low axial angle suggest that they act to prevent elongation and deformation of the mantle tissue during jetting.

Wound through the muscle layer, are three systems of intramuscular (IM) collagen fibers conventionally dubbed, IM-1, IM-2, and IM-3. IM-1 runs at an oblique angle through the muscle layer that is difficult to measure unless the angle is known a priori. Measurements of the IM-1 fiber angle relative to the squids long axis, therefore, rely on both sagittal and tangential sections (see Figure 2 for definition of primary sections) to accurately describe the path. We will refer to the respective fiber angles in these planes (demarcated by some authors as IM-1 sag and IM-1 tan) as β and λ in this analysis. Values differing by as much as 20° are reported for both β and λ. Ward and Wainright [95], measured β in *Lolligoguncula brevis* at 28°. Bone et al. [11] measured λ at 15° in *Alloteuthis subulata*. MacGillivray et al. [48] reported similar values in *Loligo pealei*. These low angles are in contrast to those reported by Thompson and Kier [87], who

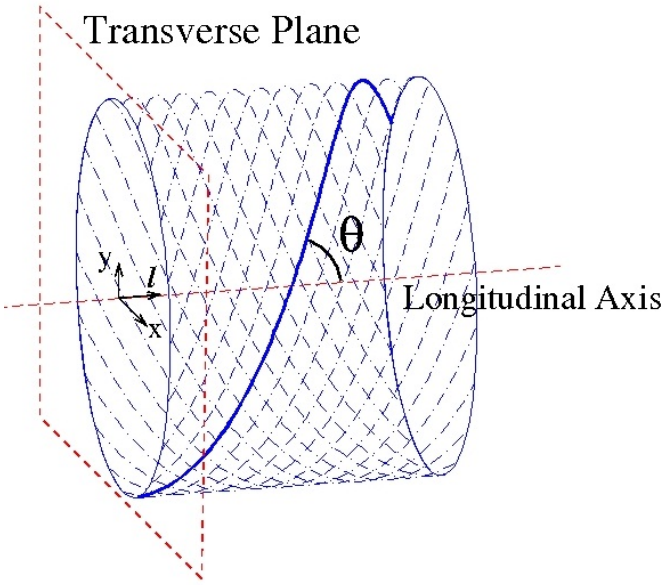

Figure D.1: The squid tunic fibers are wound in a spiral helix arrangement, and are oriented at a uniform angle (θ) to the longitudinal axis. The tunic fibers form a cylindrical tube with length L and radius a. Though the tunic consists of multiple layers of spiraling fibers only a single layer is shown for clarity.

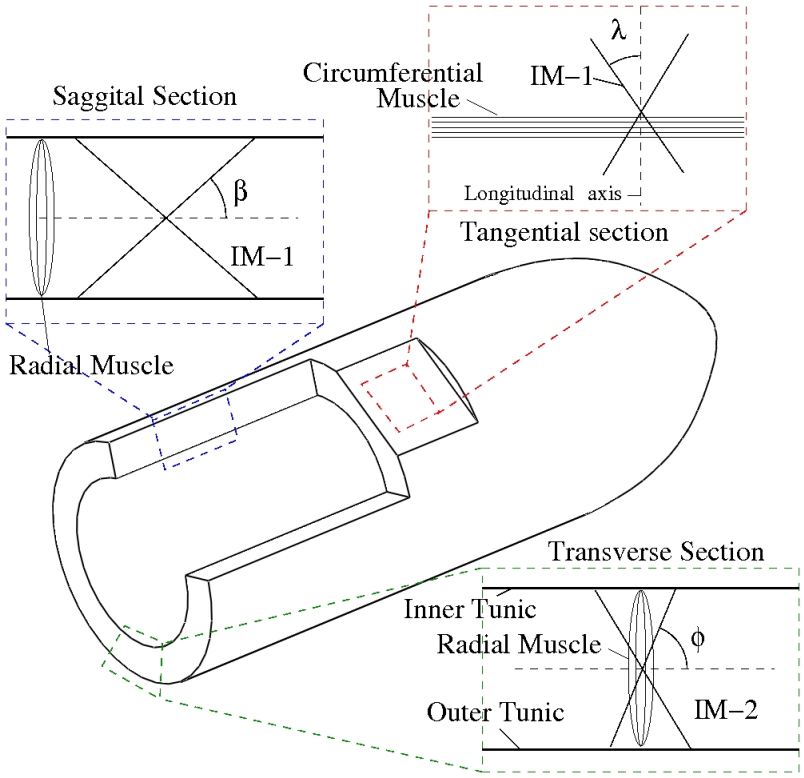

Figure D.2: Intramuscular (IM) Fibers - Conceptual diagram of the squid mantle structure. Depicted are the three primary reference planes defining the (IM) collagen fiber angles, and the muscle structure. The sagittal plane cuts through and runs parallel to the longitudinal axis; the tangential plane runs parallel to the longitudinal axis and is locally tangent to the surface; the transverse plane runs Normal to the longitudinal axis. IM-1 fibers run at oblique angles through the mantle and form angles β and λ with the longitudinal axis in the sagittal and tangential sections respectively. The IM-2 fibers are found localized in the radial muscles and form an angle ϕ with the circumferential axis in the transverse plane.

measured an angle of 43° for β and 32° for λ in juvenile *Sepioteuthis lessoniana* (though this value varies significantly throughout ontogeny). Thompson and Kier suggest that the less streamlined appearance of hatchling and juvenile squid is related to the larger fiber angles. The differences between findings may also have resulted from species differences, or largely different ratio of mantle cavity volume to total volume as will be discussed in the Maximizing Energy Storage and Results sections.

The exhalant phase of the jetting cycle begins when the squid contracts the circumferential muscles reducing the circumference of the mantle and thickening the muscle layer, while producing only a small increase in length [95, 90]. The rapid reduction in the mantle cavity volume forces seawater through the funnel and results in a high-energy jet that rapidly accelerates the squid. After coasting, the inhalant phase begins and the inner and outer tunics are brought closer together, thinning the muscle layer [99]. This is achieved by a combination of radial muscle contraction and energy transfer from deformed IM-1 and IM-2 fibers [26]. In fact, it was shown that the refilling of the mantle cavity can occur in the absence of any radial muscle power [28].

Regardless of the measurement discrepancies, the function of the IM-1 fibers is generally agreed upon. During the circumferential muscle contraction, the muscle layer thickens, and as the collagen fibers are stretched they store elastic potential energy. Once the circumferential muscles relax, the fibers pull the tunics closer together and increase the mantle circumference. We will show that the orientation of these fibers allows them to store an optimal amount of energy during contraction in the Results section.

The IM-2 measurements have been more consistent between studies. When mantle tissue was viewed in transverse sections, the IM-2 angle relative to the mantle surface has been reported from 50° to 55° [26, 87, 95]. However the exact function of these fibers is less clear.

The IM-3 fibers lie parallel to the circumferential muscle fibers, and are observed to be coiled up while the mantle is in a resting state [48]. Their orientation suggests that the IM-3 fibers are rarely fully extended while the squid is cruising, but rather aide in the contraction of the mantle after hyperinflation has been utilized for an especially large jet [48].

D.2 Problems Addressed

First the difference between maximizing ejected jet volume and maximizing total volume must be examined. Squid draw propulsive power from a transfer of momentum to a fluid jet. The force acting on the squid during this process is equal to the rate at which the squid transfers momentum to the jet. This force is equal to the product of the jet mass flux and velocity. Both of these quantities are intrinsically related to the muscle contraction rate and the dynamic response of the mantle geometry associated with muscle contraction. Jet velocity and mass flux can be determined from the rate of change of the mantle cavity volume. In this study, we model the muscular contraction as a geometric constraint rather than modeling the complicated dynamics of the muscles themselves. Therefore, the thrust experienced by the squid can be explicitly determined by the structural kinematics of the mantle. The change in mantle cavity volume is modeled with respect to tunic fiber orientation in the subsection Maximizing Jet Volume. The energy storage capacity of the IM-1 fibers was modeled next. We considered a squid swimming at a steady rate with regular contractions and without hyperinflation. We modeled the squid mantle as a tube circled by inner and outer walls (the tunics) and determined the energy stored by the IM fibers according to the mantle stress strain dynamics. In developing the energy storage model it was determined that the elongation of the squid, played a crucial role in the energy storage capacity. The fact that the IM-1 collagen fibers lie at a low angle in the sagittal plane causes the strain of individual fibers to have a strong dependence on longitudinal deformation. Though this deformation is small, inclusion in the energy storage model resulted in an optimal fiber orientation in the sagittal plane. This methodology is found in the subsection Maximizing Energy Storage.

D.3 Methods

D.3.1 Maximizing Jet Volume

To analyze the effect of collagen geometry, we constructed a rigid mathematical definition of the fiber orientation. The squid mantle is essentially a tube of interwoven muscle and collagen

fibers. The mantle is encased by the tightly woven spiral stacks of the inner and outer tunics. For the purposes of this analysis, each tunic will be modeled as a perfect cylinder composed of helically spiraling fibers Figure D.1. The parametric equations,

$$\begin{aligned} x &= a\cos(\omega z) \ , \\ y &= a\cos(\omega z) \ , \end{aligned} \tag{D.1}$$

describe the layout of a single tunic fiber, where z is the location of a point along the fiber in the longitudinal direction (starting at the anterior and extending towards the posterior) and x and y are the geometric coordinates of a point on the collagen fiber in the plane normal to the longitudinal axis a distance z from the origin (transverse plane at z). The coordinates in the transverse plane are centered on the longitudinal axis; positive y extends towards the dorsal side, and positive x forms a right handed coordinate system with y and z. The orientation of this coordinate system is depicted in (Figure 1). Additionally, a is the spiral radius, and ω is a parameter which controls the slope of the spiral (the inverse of ω is the spiral wavelength).

This construct allows us to easily determine several geometric parameters of the cylinder that are necessary to model the mantle mechanics. The cylinder diameter is simply $D = 2a$, the total cylinder length, L, is the maximum value of the parametric length $L = z_{\max}$, and the tunic fiber angle is defined as $\theta = \arctan(a\omega)$. The length of the tunic fiber is the total arc length of the spiral which is,

$$s = \int_0^L \sqrt{\dot{x}^2 + \dot{y}^2 + 1}\, dz = L\sqrt{a^2\omega^2 + 1}\ . \tag{D.2}$$

With these definitions, the cylinder geometry is defined in terms of the tunic fiber angle, θ. This allows the cylinder volume to be calculated as,

$$\begin{aligned} V = \frac{\pi}{4}D^2L &= \frac{\pi}{4}\left(\frac{s}{2\pi m}\sin\theta\right)^2 s\cos\theta \\ &= \frac{s^3}{16\pi^2 m^2}\sin^2\theta\cos\theta\ . \end{aligned} \tag{D.3}$$

Here m is the number of spiral windings in the cylinder and s is the fiber length defined in (D.2). It can be seen from (D.3) that the total cylinder volume is purely a function of fiber length, s, and fiber angle, θ. Since the collagen fibers are known to have a large low extensibility, we hold

the fiber length constant. This imposed constraint reduces the cylinder volume to a function of a single variable, θ. A similar approach has been used to analyze the total squid volume [93]. In the next section of this manuscript a model is derived describing the energy storage in the collagen fibers which requires deformation of collagen fiber lengths. However, these deformations are very small and can be neglected when defining mantle geometry with minimal error.

It is convenient to clarify our naming convention since there are several characteristic volumes which describe the squid. Equation (D.3) describes the volume of a cylinder defined by a fiber of length s and angle θ. The total squid volume is the outer tunics cylindrical volume, V_2. The total internal volume is the inner tunics cylindrical volume, V_1. The sum of the mantle cavity volume and the internal organs comprises the total internal volume. The difference between the outer tunic cylinder volume and the inner tunic cylinder volume is the mantle volume (or volume of the mantle tissue).

Assuming water to have a constant density, ρ, the mass flux across the funnel will be proportional to the rate of volume change of the inner tunic. Jet velocity can easily be determined from the volume flux if the funnel area, A, is known. This allows the thrust, T, to be described in terms of the tunic geometry to a first order approximation as,

$$T = \dot{m}u_j = \rho A u_j^2 = \frac{\rho}{A}\left(\frac{\partial V_1}{\partial t}\right)^2 = \frac{\rho}{A}\left(\frac{\partial V_1}{\partial C_1}\right)^2\left(\frac{\partial C_1}{\partial t}\right)^2 . \tag{D.4}$$

Here, $\dot{m}$ is the mass flux across the funnel, u_j is the jet velocity, A is the funnel cross sectional area, and $C1 = \pi D_1$ is the circumference of the inner tunic. The rate of change of inner tunic volume, $\frac{\partial V_1}{\partial t}$, is decomposed according to the chain rule into the rate of change of the inner tunic volume with respect to change in the inner tunic circumference, $\frac{\partial V_1}{\partial C_1}$, and the time rate of change of the inner tunic circumference itself, $\frac{\partial C_1}{\partial t}$. As was mentioned previously, the rate at which the circumference contracts is purely defined by the dynamics of the ring muscles and will be treated as a constant. Although the funnel area, A, is known to oscillate with the jetting cycle [3, 8], for simplicity we will assume that it remains constant. Therefore, the fiber orientation which maximizes $\frac{\partial V_1}{\partial C_1}$ will also maximize the thrust capacity of the squid for any given muscle contraction. This partial derivative

is defined here as a function of the inner tunic fiber angle, θ_1, by use of the chain rule,

$$\begin{aligned} \frac{\partial V_1}{\partial C_1} &= \frac{\partial V_1}{\partial \theta_1}\frac{\partial \theta_1}{\partial C_1} \propto tan\theta_1 \left(3\cos^2\theta_1 - 1\right) \ , \\ \text{where} \qquad \frac{\partial V_1}{\partial \theta_1} &\propto \sin\theta_1 \left(3\cos^2\theta_1 - 1\right) \ , \\ \text{and} \qquad \frac{\partial \theta_1}{\partial C_1} &\propto \frac{1}{\cos\theta_1} \ , \end{aligned} \tag{D.5}$$

and irrelevant constants have been omitted since we only seek to optimize with respect to θ_1, and are somewhat indifferent to the exact value of (i.e. the angle which maximizes the volume derivative will be the optimal tunic fiber angle because it results in the largest jet volume for some small contraction of the circumferential muscles, but the actual jet volume for a given contraction is less important).

D.3.2 Maximizing Energy Storage

During slow swimming, the power stroke comes from contracting the circumferential muscles that ring the mantle and contribute the bulk of its mass. The inhalant phase is powered mainly by releasing elastic energy stored during the contraction phase. There is also a set of radial muscles that extend between the inner and outer tunics (Figure 2); a contraction of these muscles will thin out the mantle layer causing its circumference to re-expand. The intramuscular collagen fibers IM-1 and IM-2 are predicted in some studies to store the necessary mechanical energy with an efficiency approaching 75% [26]. This restoring mechanism allows the mantle composition to heavily favor the circumferential muscles, with a small number of radial muscles accounting for energy losses and providing power for the hyper-inflation, required for escape jetting and large amplitude ventilation. This arrangement gives the squid a larger range of jetting capabilities since such a large portion of the mantle structure is composed of circumferential muscles used actively during jetting.

To model the energy storage process, we investigated the stress-strain dynamics in the mantle structure. We modeled the mantle as a tube defined by an inner and outer helical shell (the inner and outer tunics), whereby the geometry of each shell is defined by Equations (1) and (3), and depicted in Figure 1. The mantle geometry can be explicitly defined in terms of shell geometries.

The mantle volume is,

$$\begin{aligned} V_m &= \frac{\pi}{4}\left(D_2^2 L_2^2 - D_1^2 L_1^2\right) + \frac{\pi}{6}\left(D_2^2 - D_2 D_1 + D_1^2\right) \ , \\ &= f\left(\theta_1, \theta_2\right) \ . \end{aligned} \tag{D.6}$$

Here D_1, L_1, D_2, L_2 are the diameter and length of the inner and outer tunics respectively, which can be defined in terms of the inner and outer tunic fiber angles, θ_1 and θ_2, and fiber lengths, s_1 and s_2, as described in the previous section (we assumed that the inner and outer tunic fibers have the same angle at rest $\theta_1 = \theta_2$). Here, again, the tunic fiber lengths are considered to remain constant during the mantle contraction, which means that the tunic fiber angles must change to allow for any change in tunic volume and diameter. Therefore, a deformation of the tunic will be modeled by a small shift in the tunic fiber angle, defined as α. It should be noted that a shift in fiber angle will result in coupled changes in volume, length, and diameter. Since the jet volume will be equal to the change in internal volume, the shift in inner tunic fiber angle, α_1, can be determined if the jet volume, initial tunic fiber angle, and initial inner tunic volume are known (i.e. $V_j = V(\theta_1 + \alpha_1) - V(\theta_1)$ where V is the volume defined by (D.3) and V_j is the jet volume). Thus the shift in the inner tunic fiber angle is calculated numerically, as the value which achieves the desired jet volume. It should be noted that the actual jet volume, ejected during swimming, has been minimally studied. Most experiments rely upon indirect measurements based on wet and dry weights of deceased specimens [61, 90]. The study by Thompson and kier [88] measured the mantle cavity volume more accurately by weighing anesthetized squid with both empty and full mantle cavity. This method should give an appropriate upper bound for the ratio between the jet volume and the total volume, but does not address the possibility that certain swimming behaviors only eject a portion of the fluid in the mantle cavity. This uncertainty will be discussed later in the Results section. Anderson and Demont [3], approximated the jetting volume during swimming by determining the squid 2-D profile in the sagittal plane and interpolating the total squid volume assuming perfect axial symmetry. However, this approach completely ignores any oblateness or non-uniformity which might arise during swimming. It has also been qualitatively observed that the paralarvae (early development stages) hold a proportionally greater volume of water in their

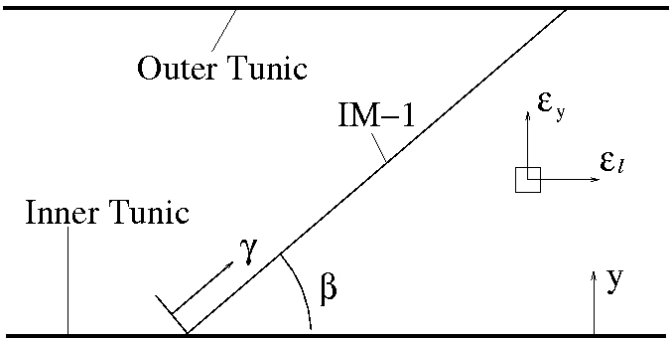

Figure D.3: Strain model construction in the sagittal plane. Here ϵ is the mantle strain (subscripts indicate direction of strain), y is the radial distance from the inner tunic, γ is the length in the direction of the IM-1 fiber.

cavities than juvenile and adult squid [24, 66].

To calculate the shift in the outer tunic fiber angle, α_2, we assumed that the mantle volume remained constant during contraction (constant muscle tissue density). The shift in the inner tunic fiber angle is directly correlated to the change in volume required for jetting. This is coupled to a contraction of the diameter and elongation of the length. As a result, the outer tunic must experience a corrective shift in fiber angle which preserves the mantle volume. This shift can be determined by setting the initial mantle volume equal to the final mantle volume,

$$f\left(\theta_1 + \alpha_1, \theta_2 + \alpha_2\right) = f\left(\theta_1, \theta_2\right) \ , \tag{D.7}$$

where f is the mantle volume function defined in (D.6). α_2 can now be calculated from (D.7) since θ_1, θ_2, and α_1 are all known. Thus the geometry of the entire mantle can be determined before and after contraction. The change in geometry will be used to determine the mantle strain characteristics (which will not be uniform).

The energy stored in the mantle structure is directly related to the strain distribution. Similar to a spring system, the energy stored in the collagen fibers is equal to the integral of the stress (force) applied during stretching over the distance [65]. Furthermore, the stress applied to a material is intrinsically related, by the elastic properties of the material, to the strain (stretching) it experiences. The strain experienced throughout the mantle structure is modeled according to the change in geometry experienced during contraction, and the strain experienced in the fibers

themselves is calculated according to their orientation in the mantle. The axial symmetry of the mantle model allows us to define the 3-dimensional strain in cylindrical coordinates. In general, the contraction of the mantles circumferential muscles causes the tunic cylinders to decrease in circumference and volume, but also causes the mantle to increase in length and thickness. Thus, the strain in the radial and longitudinal directions will be positive, but the strain in the tangential direction (hoop strain) will be negative. We analyzed the orientation of the IM-1 fibers in the sagittal plane since this involves the radial and longitudinal components of strain, which are both positive.

Consider a longitudinal slice through the top of the mantle, in the sagittal plane. Figure 3 shows the strain orientation and projection of the IM-1 fibers onto this plane. According to the original model construction, the diameter of each tunic is assumed to be constant along its length. This means that the thickness of the mantle will increase uniformly throughout the mantle during contraction. Consequently, the radial component of strain throughout the section will be constant, $\epsilon_y = \frac{h_f - h_0}{h_0}$, where $h = D_2 - D_1$ is the thickness of the mantle, and the subscripts 0 and f refer to the initial and final states of the mantle (before and after contraction) respectively. The lateral strain is slightly more complicated. Both tunics experience a contraction, which results in elongation. However, the amounts by which they contract are not equal ($\alpha_1 \neq \alpha_2$), so their elongations will not be strictly equal either. The lateral strain of each tunic can be determined from the length deformation, $\epsilon_i = \frac{L_{if} - L_{i0}}{L_{i0}}$, where ϵ_i is the tunic strain, and the subscript i can take a value of either 1 or 2 and refers to either the inner or outer tunic respectively. Assuming that the material on the surface of the tunic experiences the same strain as the tunic itself, and a linear strain distribution, the lateral strain at any location in the section is $\epsilon_l(y) = \epsilon_2 + (\epsilon_1 - \epsilon_2)\,\frac{y}{h_f}$, where y is the distance from the inner tunic in the radial direction, and h_f is the final mantle thickness. This gives a complete strain distribution in the longitudinal and radial directions, which allows us to define the total strain imposed on a collagen fiber lying in this section.

The stress-strain relationship for collagen fibers is only defined in the direction of the fibers primary axis since collagen fibers only support tensile loads, and the energy stored in a given fiber

is determined purely by the strain in the direction of that fiber. For a fiber of length b, which is oriented at the IM-1 sagittal angle β with respect to the longitudinal axis, the normal strain can be calculated as,

$$\begin{aligned} \epsilon_{\text{fiber}} &= \frac{1}{b}\int_0^b \left[\epsilon_l(y(\gamma))\cos\beta + \epsilon_y \sin\beta\right]\ d\gamma\ , \\ &= \frac{\epsilon_1+\epsilon_2}{2}\cos\beta + \epsilon_y\sin\beta\ , \end{aligned} \tag{D.8}$$

where γ is a variable which describes position along the length of the fiber (see Figure D.3). Given the final strain in a single fiber as defined by (D.8), the energy stored in that fiber is defined by a simple integral equation.

$$E_{\text{fiber}} = \int_0^{\delta_f} F(\epsilon(\delta))\ d\delta = bA_{\text{fiber}}\int_0^{\epsilon_{\text{fiber}}} \sigma(\epsilon)\ d\epsilon \tag{D.9}$$

In this equation δ is the change in fiber length, δ_f is the total change after contraction, A_{fiber} is the cross sectional area of the fiber, F is the stretching force acting on the fiber (tension), and is the stress of the fiber which is a function of the strain. Gosline and Shadwick examined the stress strain relationship for the mantle tissue of *Loligo opalescens* ([26] Figure 7). A section of the mantle tissue was compressed in the circumferential direction to mimic natural muscle contraction, and the resulting reaction forces were recorded. The mantle tissue was determined to be relatively stiff with an elastic modulus of 2×10^6 Nm^{-2}. Unfortunately, these findings only give the bulk material properties rather than the elastic modulus of the collagen fibers themselves, which is the relationship required for our potential energy model (D.9). To the authors knowledge there are no studies which present the elastic properties of individual IM fibers; however, Gosline and Shadwick [27] performed tensile testing on thin isolated sheets of tunic fibers. Since the fibers in the tunic are at very acute angles, this stress strain relationship should be considered a decent approximation for the stress strain relationship of the IM fibers, and has been recreated in Figure 4. These experiments indicated that collagen fibers exhibit a parabolic stress strain relationship in the low strain regime (toe region), but the slope quickly becomes close to linear and maintains a linear proportionality for the majority of the strain domain. Before reaching the critical breaking stress, there is a very small region where the stress strain relationship asymptotically plateaus which is

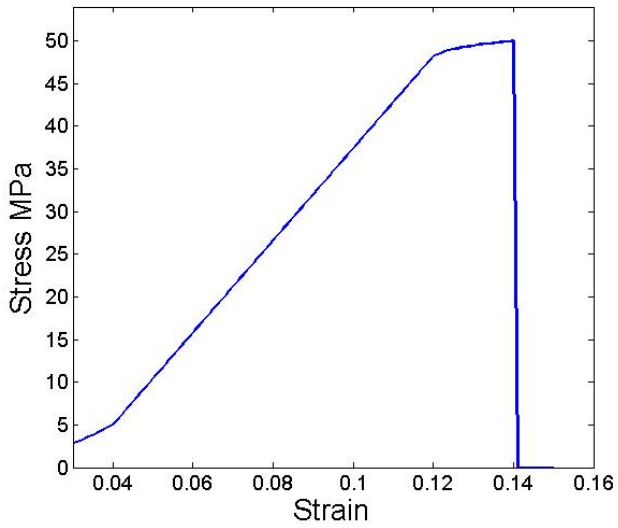

Figure D.4: Stress vs. strain relationship used in the model (estimated from [27] for a sheet of tunic collagen fibers.)

typical behavior for elastic fibers which deform plastically at high strains, but the transition in collagen is very sharp. Therefore, we modeled the stress strain relationship as,

$$\sigma = \begin{cases} c_1\epsilon^2 & \text{if} \quad \epsilon \leq \epsilon_1 \\ \sigma_1 + E\epsilon & \text{if} \quad \epsilon_1 \leq \epsilon \leq \epsilon_2 \\ c_2\left(\epsilon + c_3\right)^{\frac{1}{n}} & \text{if} \quad \epsilon_2 \leq \epsilon \leq \epsilon_m \\ 0 & \text{if} \quad \epsilon_m \leq \epsilon \end{cases}, \tag{D.10}$$

where,

$$E = 540 \text{ MPa} \quad \begin{array}{lll} \epsilon_1 = 0.04 & \sigma_1 = 5 \text{ MPa} & c_1 = \sigma_1/\epsilon_1^2 \\ \epsilon_2 = 0.13 & \sigma_2 = 48 \text{ MPa} & c_2 = \left(\frac{\sigma_m^2 - \sigma_2^2}{\epsilon_m - \epsilon_2}\right)^{\frac{1}{n}} \\ \epsilon_m = 0.14 & \sigma_m = 49 \text{ MPa} & c_3 = (\sigma_m/c_2) - \epsilon_m \end{array}$$

where ϵ_1, ϵ_2, and ϵ_m are the critical strains in the stress/strain profile corresponding to the beginning and end of the linear region and the critical failure strain respectively. E is the modulus of elasticity in the linear range (540 MPa), σ_1, σ_2, and σ_m are the stress values corresponding to strains ϵ_1, ϵ_2, and ϵ_m. The values used for all of these coefficients were estimated from ([27], Fig. 5).

This form was chosen because it closely matches the shape of empirical curves obtained for

both invertebrate and mammalian collagen [26, 74, 92, 94]. However, it is hypothesized that the toe region is due to the fact that the collagen fibers are still not perfectly aligned with the strain direction, and this is in essence a straightening process. Therefore, the stress strain relationship was also be modeled as a perfect spring with the modulus of elasticity equal to that of the linear region; however, this had very little effect on optimal fiber angles predicted by the model, which is mostly sensitive to the critical stress/strain values, rather than the profile in the low strain region.

Now all of the relationships in the mantle model have been defined so that the total energy stored in a single fiber is found by numerically approximating the integral of (D.9), using the stress relationship defined by (D.10).

To determine an actual value for total energy storage in the mantle structure several constraints must be imposed. The initial geometry of the mantle was defined according to the length, diameter and thickness of *Sepioteuthis lessoniana* as were reported in [87]. We also assumed that the inner and outer tunics start at the same length which gives a relationship between the fiber lengths of each tunic. The predictions of this model under these constraints will be compared with observed data in Section D.4.

D.4 Results

D.4.1 Tunic Fiber Orientation

To maximize thrust production the fiber angle should be aligned so that the ejected volume flux is maximized rather than the total volume. The rate at which fluid is ejected should be considered proportional to the rate of change in the total volume with respect to a change in the circumference, as is derived in (D.5).

Figure D.5 shows the instantaneous change in tunic cylinder volume with respect to a differential change in circumference, as a function of the initial fiber angle. It can be seen from this figure that, for a given small contraction of the circumferential ring muscles, the squid will expel a maximal jet if the initial fiber angle is near 31°. This jet will result in maximum thrust assuming

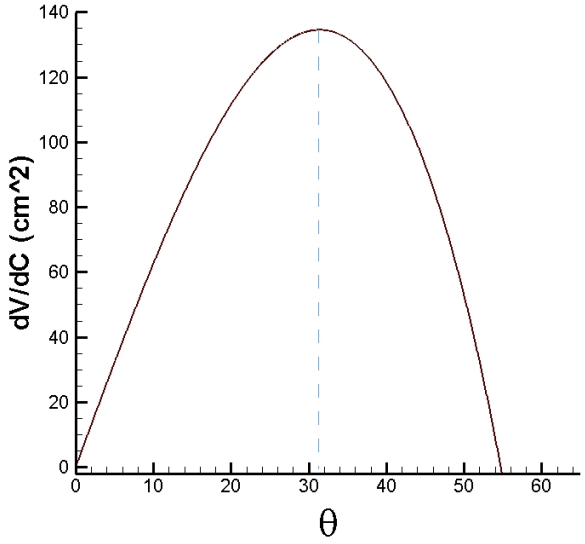

Figure D.5: Differential change in cylinder volume with respect to a contraction of circumference.

that the ring muscles have a constant rate of contraction (D.4). This angle approaches the actual orientation of tunic fibers measured by Ward and Wainwright [95].

D.4.2 Intramuscular Fiber Orientation

The squid mantle is oriented so that the circumferential ring muscles (which constitute the bulk of the mantle muscle tissue) provide sufficient compression forces during the jetting phase. However, the refilling phase is driven by sparsely packed radial muscles as well as a release of elastic potential energy stored in the deformed mantle fiber structure, which provides sufficient force to refill the mantle cavity in the absence of any radial muscle contraction [28].

There is an obvious dichotomy between the tightly packed collagen fibers in the tunics and the scarce intramuscular collagen fibers. The tunic fibers are wound in layers of alternating orientation to form a more or less uniform tube of collagen. The IM fibers, by contrast, are arranged more sparsely throughout the muscle tissue, accounting for $0.1-7\%$ of the total mantle volume, depending on the age of the squid [87]. The abundance of collagen fibers in the tunics suggest that these self reinforced fibers experience minimal stretching compared to the IM fibers. As discussed in the subsection Maximizing Energy Storage, energy is directly related to the deformation of the fibers. The small deformation of tunic fibers results in a low capacity for energy storage, indicating that the tunic fibers primarily serve a structural purpose. In contrast, the high deformation of the IM-1 fibers suggests that they serve as the primary energy storage devices.

Figure D.6 shows the normalized energy storage capacity of the IM-1 fibers as a function of the sagittal plane orientation angle β, as was modeled in the subsection Maximizing Energy Storage. The storage capacity was normalized by the maximum achievable energy storage over the β distribution. Figure D.6a shows the fiber storage capacity vs. β for a jet volume ratio of 0.25, and Figure D.6b for a jet volume ratio of 0.45. It can be seen that a squid expelling a jet with a low volume ratio will store a maximum potential energy when the IM-1 fibers are oriented with an angle $\beta = 67°$. The peak in the energy storage capacity curve is very oblate giving a large range of fiber angles with similar energy storage capacity. Conversely the energy storage capacity for the

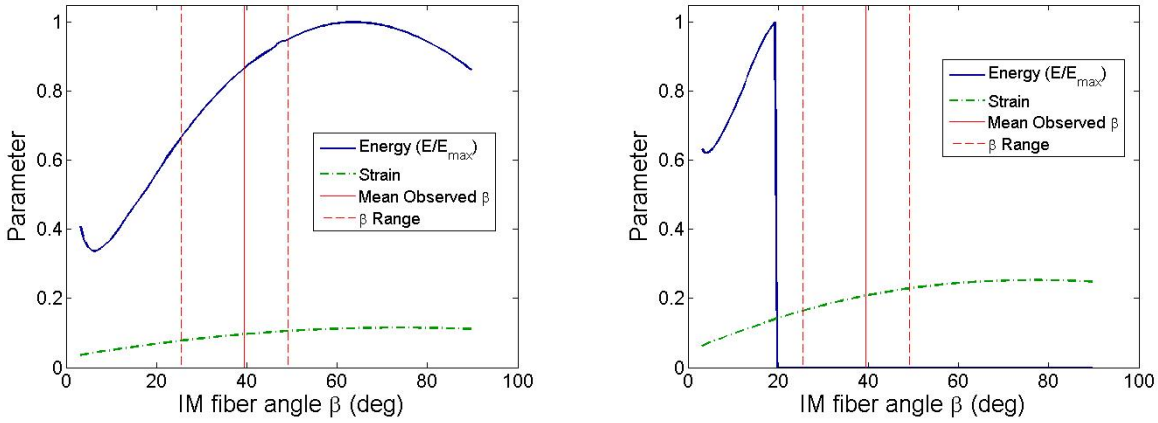

Figure D.6: Energy storage capacity of the mantle structure and IM-1 collagen fiber strain vs. fiber angle β. Energy storage capacity as a function of fiber angle is represented by the solid line, fiber strain is shown by the dash-dotted line, and actual distributions of fiber angles are bounded by the vertical band. Energy storage capacity for a cavity volume ratio of 0.25 (a), and cavity volume ratio of 0.45 (b).

squid ejecting a jet with a larger volume ratio has a very distinct peak at $\beta = 23°$. This peak does not actually correspond to an equilibrium balance between axial and radial strain, but rather is associated with the failure strain of the collagen fibers; as the fiber angle increases so does the strain in the fiber until the failure strain is reached and the fiber is ruptured.

Data reported for *Sepioteuthis lessoniana* in [88] was used to define the initial geometry of the mantle (length, diameter, thickness). This data set was chosen because the mantle geometry and mantle cavity volume ratio required for the energy storage model is presented for a large range of squid developmental stages. Additionally the IM fiber angles are given in [87] corresponding to a similar squid population, providing a reference to validate the model. The values for β over this data set are shown as a vertical band in Figure D.6 (bounded on either side by the maximum and minimum observed fiber angles). The cavity volume ratio can vary quite drastically throughout ontogeny, and is more precisely, a maximum bound on the jet volume, and ignores the possibility that during cruising the squid might not eject the entire cavity volume. We used our model to predict optimal fiber angle for the entire range of cavity volume ratios seen in *S. lessoniana* using the mantle geometry associated with that cavity volume ratio and assuming complete evacuation of the cavity. We also calculated the optimal fiber angle for the same range of jet volume ratios using the mantle geometry of a single adult squid. The optimal fiber angles determined for both ranges of initial conditions are shown in Figure D.7. It can be seen that the optimal fiber angles for both conditions are nearly identical, indicating that the squid mantle grows such that the relationship between jet volume ratio and mantle strain is preserved.

In addition, the longitudinal strain on the inner tunic was calculated for the same set of volume fractions, and the result is also shown in Figure D.7. For the entire range of volume fractions, the longitudinal tunic strain remains very small $< 8\%$; a fact which has been observed in previous experiments [63]. As a result many models have ignored longitudinal tunic strain entirely, thus losing knowledge of a key energy storage mechanism as will be analyzed in the Discussion.

The model predicts an optimal fiber angle with respect to jet volume ratio (cavity volume ratio), which can be related to dorsal mantle length (via Thompson and Kier [88]). Therefore we

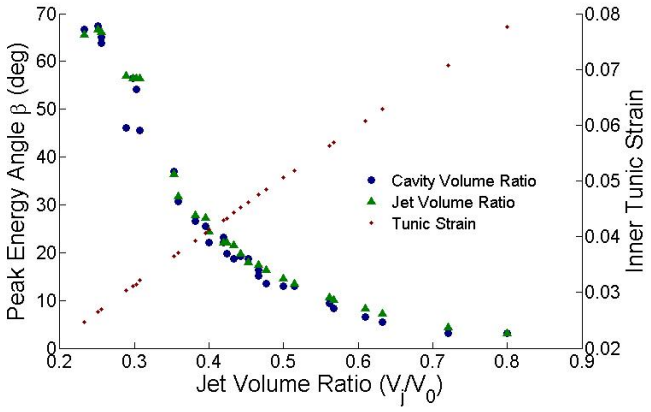

Figure D.7: Optimal IM-1 sagittal fiber angle β as well as inner tunic longitudinal stress ϵ_1 shown as a function of the volume ratio $\frac{V_j}{V}$.

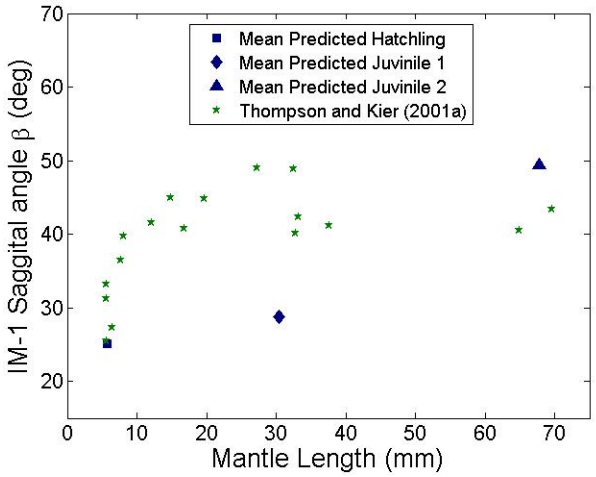

Figure D.8: IM-1 sagittal fiber angle, β, throughout ontogeny. Predicted optimal fiber angles shown by large square, diamond, and triangle markers and actual fiber angles marked by star.

can directly compare the optimal fiber angle predicted by the model with the actual fiber angles observed in the squid [87] over the range of dorsal mantle lengths reported. The large variability in cavity volume fraction for a given dorsal mantle length, results in the model predicting a similarly large range of optimal fiber angles for a given dorsal mantle length. To aid in visualizing this data the predicted optimal fiber angle was averaged for three mantle length regions (hatchling, juvenile 1, and juvenile 2) which are compared to the actual fiber angle distribution in Figure D.8.

D.5 Discussion

The use of helically wound high tensile strength fibers has been examined in the anatomy of several invertebrates with respect to spiral orientation angles. Harris and Crofton [30] first looked into the effect of the orientation of reinforcing fibers on the length and volume relationship in nematodes. This analysis was extended and applied to both nemerteans and turbellarians (both of which are adept at changing shape) in Clark and Cowey [13], and determined a relationship between volume and fiber angle for a given length of worm. The volume attains a maximum for a fiber angle near 55°. Similarly, this nominal angle was identified by Harris and Crofton [30] as the angle that would maintain a constant worm volume for a small deflection in the fiber orientation

angle. Vogel [93] adapted this analysis to squid tunic structures and noted that actual tunic fiber angles will result in a structure that decreases volume with decreased diameter, despite an increase in length, and that the squid volume is maximized at the nominal fiber angle of 55°. However, as is shown in Figure D.5, a tunic fiber angle close to 31° will maximize the jet volume flux for a given circumferential muscle contraction (directly related to the jetting thrust), which is very close to actual squid tunic fiber angles. Figure D.5 also shows that when the fiber angle is 55°, there will be no change in volume for a small contraction in circumference (or equivalently diameter), as observed by Harris and Crofton [30].

Unlike previous studies [95, 13] which assert that the low angles of the tunic and IM fibers prevent the mantle from changing length, our model incorporates the variation in mantle length during contraction. Our analysis predicts that IM-1 fibers have an optimal angle in the sagittal plane that allows for maximum energy storage. Additionally, we find that as length, diameter, and volume are intrinsically coupled, a purely constant mantle length is an overly restrictive assumption and is not required to achieve maximal jet volume. Furthermore, the large aspect ratio of the mantle (being much longer than it is thick), causes a small deformation in length to result in substantial potential energy storage in the longitudinal direction. In fact, the predicted longitudinal strain in the tunics is quite small, 4% in the outer tunic and 4.8% in the inner tunic, which is within the range of longitudinal strains measured by Packard and Trueman [63]. These longitudinal tunic strains were determined assuming a volume ratio of 0.45. In the Results section, we calculated the longitudinal strain on the inner tunic for several other volume ratios. The sensitivity of tunic strain to volume ratio was shown in Figure D.7. It can be seen that even as the jet volume approaches a maximum value of 0.8, the longitudinal tunic strain remains below 8%.

The sensitivity of the optimal IM-1 fiber angle β with respect to cavity volume fraction and jet volume fraction was also shown in Figure D.7. The large variation in the optimal fiber angle can primarily be attributed to the fact that large volume ratio contractions produce critical strain in the IM-1 fibers with larger orientation angles in the sagittal plane. In fact, if the fiber is assumed to have a boundless linear stress strain relationship, the optimal fiber angle varies by only 3°. This

means that squid can eject several different size jets with similar mantle energy storage properties. As was previously mentioned, Figure D.6a shows that the energy storage capacity has a rather broad peak (when critical strain is not a factor), meaning that there is a large range of fiber angles, β, with favorable energy storage characteristics. Moreover, even the minimum fiber angle observed throughout ontogeny, still has an energy storage capacity close to 70% of predicted maximum for low volume ratio. Therefore, the IM-1 fibers are most likely oriented to provide the maximum energy storage, within the limiting physical bounds of the collagen fibers.

The comparison of IM-1 sagittal fiber angles in Figure 8 shows decent agreement between predicted optimal β and actual measured β; but the optimal energy storage model predicts β more acute than that observed, for both hatchling and shorter juvenile squid. First, it should be noted that both these age groups have the most uncertainty in cavity volume ratio, which will certainly carry over to uncertainty in predicting optimal fiber angles. Additionally, the squid mantle is not a perfect cylinder but tapered (like a conical tube), this shape is more pronounced in younger squid, so the cylinder mantle approximation may not be valid for these young developmental stages.

In the transverse plane, the components of mantle strain were quite different. The radial component of strain (through the thickness) was still defined by the mantle thickness expansion. However, the circumferential component (tangent to the tunic) was negative due to the contraction of the circumferential muscles. Since fibers can only store energy under tension (not compression), the IM-2 fibers would store a maximum amount of energy if they were oriented radially (90°). The fact that these fibers are oriented at an angle between 50° and 55° suggests that these fibers are not purely energy storage components, but also serve to transmit forces from the discrete radial muscles to the rest of the mantle.

The various systems of collagen fibers within squid mantle tissue form a complex mechanical system. Several studies have observed a nearly universal orientation of these fiber systems across several species. We have provided a rigid mathematical model to analyze the structural mechanics of the tunic fiber system, and have determined that the tunic fibers angle of incidence maximizes the expelled jet volume for a given contraction of circumferential muscles. We have also modeled

the energy storage dynamics of the IM-1 fiber system in the sagittal plane. It was shown that the orientation of these fibers maximizes their energy storage capacity, within the physical limitations of the collagen fiber itself. In addition it was determined that previous assumptions about the role of IM-1 fibers in restricting longitudinal deformation are not supported by the energy analysis.